

**Influence of chemical substitutions and the oxygen  
content on superconducting properties of RE123  
single crystals**

Anna Kortyka

Praca doktorska

wykonana w Instytucie Fizyki Polskiej Akademii Nauk  
pod kierunkiem Dr hab. Romana Puźniaka, profesora IFPAN



Warszawa, październik 2010

*„I do not know what I may appear to the world, but to myself I seem to have been only like a boy playing on the sea-shore, and diverting myself in now and then finding a smoother pebble or a prettier shell than ordinary, while the great ocean of undiscovered truth lay all undiscovered before me”*

Sir Isaac Newton

# Contents

|  |           |
|--|-----------|
| <b>Abstract</b>  | <b>iv</b> |
| <b>Streszczenie</b>  | <b>vi</b> |
| <b>1. Introduction</b>   | <b>1</b>  |
| <b>2. Theoretical background</b>   | <b>6</b>  |
| 2.1. London model.....   | 7         |
| 2.2. Ginzburg-Landau theory.....   | 9         |
| 2.3. Superconductor in a magnetic field.....   | 11        |
| 2.4. Flux-line pinning.....  | 11        |
| 2.5. Intrinsic pinning.....  | 13        |
| 2.6. Bean model.....   | 14        |
| 2.7. Rigours analysis of the isothermal $M(H)$ .....   | 17        |
| <b>3. Measurement techniques</b>   | <b>21</b> |
| 3.1. SQUID magnetometry.....   | 21        |
| 3.2. AC susceptibility.....  | 23        |
| 3.3. Torque magnetometry.....  | 24        |
| 3.4. Hall probe scanning technique.....  | 26        |
| <b>4. Single crystals of <math>\text{REBa}_2\text{Cu}_3\text{O}_{7-\delta}</math> and their characterization</b>           | <b>29</b> |
| 4.1. Crystal growth and annealing.....   | 30        |
| 4.2. Critical temperature and oxygen content.....  | 32        |
| 4.3. Solubility of a rare earth for Ba ions in $\text{REBa}_2\text{Cu}_3\text{O}_{7-\delta}$ .....                         | 33        |
| <b>5. Superconducting state parameters and their evaluation</b>  | <b>35</b> |
| 5.1. Intrinsic parameters.....   | 35        |
| 5.2. Extrinsic parameters.....   | 38        |
| <b>6. Oxygen deficiency effect in <math>\text{SmBa}_2\text{Cu}_3\text{O}_x</math>: experimental results and discussion</b> | <b>41</b> |
| 6.1. Single crystals of $\text{SmBa}_2\text{Cu}_3\text{O}_x$ .....   | 42        |

|  |            |
|--|------------|
| 6.2. Intrinsic properties of $\text{SmBa}_2\text{Cu}_3\text{O}_x$ .....  | 43         |
| 6.3. Historical remarks about the temperature dependence of the anisotropy parameter.....  | 46         |
| 6.4. First evidence for a temperature dependent anisotropy in cuprates.....  | 47         |
| 6.5. Possible origins of the temperature dependence of the anisotropy in underdoped cuprates.....  | 55         |
| 6.6. Extrinsic properties of $\text{SmBa}_2\text{Cu}_3\text{O}_x$ .....  | 57         |
| 6.7. Brief summary of the oxygen deficiency effect in $\text{SmBa}_2\text{Cu}_3\text{O}_x$ .....   | 61         |
| <b>7. Low level Pr substitution in <math>\text{YBa}_2\text{Cu}_3\text{O}_{7-\delta}</math>: experimental results and discussion</b>                | <b>64</b>  |
| 7.1. Single crystals of $\text{Y}_{1-x}\text{Pr}_x\text{Ba}_2\text{Cu}_3\text{O}_{7-\delta}$ .....   | 64         |
| 7.2. Influence of praseodymium ions on the intrinsic properties of $\text{Y}_{1-x}\text{Pr}_x\text{Ba}_2\text{Cu}_3\text{O}_{7-\delta}$ .....      | 67         |
| 7.3. Influence of praseodymium ions on the bulk pinning in $\text{Y}_{1-x}\text{Pr}_x\text{Ba}_2\text{Cu}_3\text{O}_{7-\delta}$ .....              | 74         |
| 7.4. Influence of Pr ions on the intrinsic pinning.....  | 81         |
| 7.5. Brief summary of low level Pr substitution in $\text{YBa}_2\text{Cu}_3\text{O}_{7-\delta}$ .....  | 84         |
| <b>8. Rare earth substitutions into Y position in <math>\text{YBa}_2\text{Cu}_3\text{O}_{7-\delta}</math>: experimental results and discussion</b> | <b>86</b>  |
| 8.1. Single crystals of $\text{REBa}_2\text{Cu}_3\text{O}_{7-\delta}$ .....  | 87         |
| 8.2. Influence of rare earth ions on the intrinsic properties of $\text{REBa}_2\text{Cu}_3\text{O}_{7-\delta}$ .....                               | 89         |
| 8.3. Influence of rare earth ions on the extrinsic properties of $\text{REBa}_2\text{Cu}_3\text{O}_{7-\delta}$ .....                               | 92         |
| 8.4. Brief summary of rare earth substitutions into Y position in $\text{YBa}_2\text{Cu}_3\text{O}_{7-\delta}$ .....                               | 99         |
| <b>9. Conclusions</b>  | <b>101</b> |
| <b>Acknowledgements</b>  | <b>105</b> |
| <b>References</b>  | <b>107</b> |
| <b>List of publications</b>  | <b>120</b> |
| <b>Curriculum Vitae</b>  | <b>121</b> |

## Abstract

High-temperature superconductivity in copper oxide compounds has been viewed as an “exotic” phenomenon since its discovery in 1986. It was suggested that superconductivity in the cuprates is driven by magnetic interactions between carriers or by polaron formation rather than by the conventional mechanism of exchange of lattice vibrations. On the other hand, the phenomenon that attracted most attention in the last few years was the multiband superconductivity observed in  $\text{MgB}_2$  and suggested to exist in the iron-based superconducting pnictides. Investigating  $\text{MgB}_2$  and the pnictides several new phenomena were observed which turned out to be challenging for an interpretation with existing concepts of high- $T_c$  superconductivity. Here, some of these newly-observed phenomena are discussed with respect to  $\text{REBa}_2\text{Cu}_3\text{O}_{7-\delta}$  (RE123, RE – a rare earth or Y ion) single crystals.

The aim of this work was to investigate compounds of RE123 superconductors, namely the oxygen deficiency effect in Sm123, the influence of partial substitution of Y by Pr ions in the Y123 system, and the influence of different rare earths on the superconducting state parameters of RE123. The intrinsic and extrinsic superconducting state parameters were determined from magnetization measurements and by applying the effective media approach scaling method. Torque magnetometry was employed to study the anisotropy of the superconducting state parameters,  $\gamma$ . The vortex pinning behaviour was analysed using a rigorous treatment, based on the Ginzburg-Landau theory, for the magnetization behaviour and for the critical current density,  $J_c(B)$ .

Single crystals of  $\text{SmBa}_2\text{Cu}_3\text{O}_x$  with an oxygen content corresponding to  $T_c$ 's varying from 19.6 to 63.6 K were investigated and the superconducting state parameters derived. It was found that the crossover field,  $H_{cr}$ , where the irreversibility line changes slope, remains higher for  $\text{SmBa}_2\text{Cu}_3\text{O}_x$  than for  $\text{YBa}_2\text{Cu}_3\text{O}_{7-\delta}$  single crystals, which is related to better vortex pinning in the former. On the other hand, the dependence of the anisotropy on the transition temperature in  $\text{SmBa}_2\text{Cu}_3\text{O}_x$  is very similar to that of  $\text{YBa}_2\text{Cu}_3\text{O}_{7-\delta}$ .

Torque magnetometry measurements revealed that the anisotropy in underdoped  $\text{SmBa}_2\text{Cu}_3\text{O}_x$  is strongly temperature dependent, while only a weak dependence on the magnetic field was observed. It seems to be clear that the underdoped cuprates have the same intrinsic temperature dependence of the anisotropy parameter as multiband superconductors. On the other hand, no evidence for a field dependent superfluid density was observed, which may suggest that the multiband scenario, that leads to the temperature

dependence of the anisotropy parameter in  $\text{MgB}_2$  and the pnictides, is not applicable for cuprates.

Single crystals of  $\text{Y}_{1-x}\text{Pr}_x\text{Ba}_2\text{Cu}_3\text{O}_{7-\delta}$  with  $x$  varying from 0 to 0.024 were studied in order to investigate how the superconducting state parameters change upon introducing Pr ions. Substitution of Y by Pr introduces effective pinning centres leading to an increase of the critical current density. An averaged anisotropy parameter of 7.4 was determined. No influence of the Pr ion concentration on  $\gamma$  was observed. In all crystals a pronounced maximum at angles between  $0.5^\circ$  and  $1^\circ$  out of the  $ab$ -plane was observed in the irreversible angular dependence of the torque. This maximum is attributed to intrinsic pinning associated with kinked vortices.

Finally, the superconducting state parameters and the vortex pinning behaviour were studied for three optimally oxygenated single crystals with different rare earths introduced into the Y position in  $\text{YBa}_2\text{Cu}_3\text{O}_{7-\delta}$ . A common pinning mechanism was found in  $\text{SmBa}_2\text{Cu}_3\text{O}_{7-\delta}$  and  $\text{NdBa}_2\text{Cu}_3\text{O}_{7-\delta}$  superconductors, where pinning by  $(\text{Nd,Sm})_{1+y}\text{Ba}_{2-y}\text{Cu}_3\text{O}_{7-\delta}$  type solid solutions was probably responsible for the pronounced fishtail effect. It is assumed that solid solutions can lead to magnetic/charge modulations, i.e. stripes. For temperatures close to  $T_c$ , pinning centres are more effective in  $(\text{Nd,Sm})\text{Ba}_2\text{Cu}_3\text{O}_{7-\delta}$  than in  $\text{YBa}_2\text{Cu}_3\text{O}_{7-\delta}$  single crystals.

## Streszczenie

Nadprzewodnictwo wysokotemperaturowe w miedzianach, od momentu jego odkrycia w roku 1986, uważane jest za zjawisko egzotyczne. Istnieją wskazania, iż za tworzenie się par Coopera w tych materiałach odpowiedzialne są oddziaływania magnetyczne pomiędzy nośnikami lub też polarony, a nie fonony jak to ma miejsce w nadprzewodnikach klasycznych. Jednocześnie, jednym ze zjawisk które wzbudziły największe zainteresowanie w ciągu ostatnich kilku lat było nadprzewodnictwo wielopasmowe, występujące w  $MgB_2$  i prawdopodobnie w nadprzewodnikach z płaszczyznami żelazowymi (pniktydkach). W trakcie badania tych materiałów odkryte zostały nowe właściwości, co może być przydatne w interpretacji zjawisk obserwowanych w nadprzewodnikach wysokotemperaturowych. Niektóre z tych właściwości zostały przeanalizowane w prezentowanej rozprawie w trakcie badań monokryształów  $REBa_2Cu_3O_{7-\delta}$  (RE123, RE – jon ziemi rzadkiej lub Y).

Celem tej pracy było zbadanie wpływu podstawień chemicznych i zawartości tlenu na właściwości stanu nadprzewodzącego wybranych nadprzewodników z grupy RE123. Zbadany został wpływ stopnia utlenienia na właściwości nadprzewodzące Sm123, wpływ częściowego podstawienia jonów Y przez jony Pr w Y123 oraz wpływ jonów ziemi rzadkiej na parametry stanu nadprzewodzącego RE123. Samoistne i niesamoistne właściwości stanu nadprzewodzącego zostały wyznaczone na podstawie pomiarów magnetycznych oraz dzięki zastosowaniu metody skalującej w podejściu efektywnego ośrodka (ang.: *effective media approach*). Do badań anizotropii parametrów stanu nadprzewodzącego,  $\gamma$ , została zastosowana magnetometria torsyjna. Kotwiczenie wirów było analizowane w ramach modelu, opartego na teorii Ginzburga-Landaua, służącego do opisu magnetyzacji oraz gęstości prądu krytycznego,  $J_c(B)$ .

Wyznaczono parametry stanu nadprzewodzącego dla monokryształów  $SmBa_2Cu_3O_x$ , w których stopień utlenienia odpowiadał wartości  $T_c$  z przedziału pomiędzy 19.6 a 63.6 K. Zaobserwowano, iż pole rozgraniczające (ang.: *crossover field*),  $H_{cr}$ , w którym linia nieodwracalności zmienia nachylenie, ma większe wartości dla monokryształów  $SmBa_2Cu_3O_x$  niż dla  $YBa_2Cu_3O_{7-\delta}$ , co związane jest z lepszym kotwiczeniem wirów w  $SmBa_2Cu_3O_x$ . Z kolei zależność parametru anizotropii od temperatury krytycznej jest bardzo podobna dla  $SmBa_2Cu_3O_x$  i dla  $YBa_2Cu_3O_{7-\delta}$ .

Pomiary przy pomocy magnetometru torsyjnego wykazały, iż anizotropia parametrów stanu nadprzewodzącego w niedomieszkowanym  $SmBa_2Cu_3O_x$  jest silnie zależna od

temperatury i bardzo słabo zależna od pola magnetycznego. Można sądzić, iż niedomieszkowane miedziany, podobnie jak nadprzewodniki wieloprzerwowe, należą do tej samej grupy materiałów, dla których temperaturowa zależność anizotropii jest właściwością samoistną. Jednakże nie zaobserwowano zmiany gęstości nośników nadprzewodzących (ang.: *superfluid density*) w funkcji pola magnetycznego, co może sugerować iż model nadprzewodnictwa wieloprzerwowego, który prowadzi do temperaturowej zależności anizotropii w  $\text{MgB}_2$  oraz w pniktydkach, nie jest prawdziwy dla miedzianów.

W celu określenia wpływu jonów prazeodymu na parametry stanu nadprzewodzącego  $\text{YBa}_2\text{Cu}_3\text{O}_{7-\delta}$  zbadane zostały monokryształy  $\text{Y}_{1-x}\text{Pr}_x\text{Ba}_2\text{Cu}_3\text{O}_{7-\delta}$  o zawartości prazeodymu z zakresu od 0 do 0.024. Zaobserwowano, iż jony Pr podstawione w pozycję jonów Y są efektywnymi centrami kotwiczenia, co prowadzi do wzrostu wartości gęstości prądu krytycznego. Wyznaczono średni parametr anizotropii równy 7.4, przy czym nie zaobserwowano wpływu jonów Pr na  $\gamma$  w badanym zakresie koncentracji  $x$ . Zaobserwowano silne maksimum w nieodwracalnej części zależności momentu skręcającego dla kątów pomiędzy  $0.5$  a  $1^\circ$  odchylenia od płaszczyzny  $ab$ . Występowanie takiego maksimum spowodowane jest silnym kotwiczeniem wirów pomiędzy płaszczyznami (ang.: *intrinsic pinning*), które w badanych kryształach związane jest ze schodkową strukturą wirów (ang.: *kinked vortices*).

Parametry stanu nadprzewodzącego oraz mechanizm kotwiczenia wirów były badane dla trzech optymalnie utlenionych monokryształów z różnym jonem ziemi rzadkiej podstawionym w miejsce Y w  $\text{YBa}_2\text{Cu}_3\text{O}_{7-\delta}$ . Znalezione wspólny mechanizm odpowiedzialny za kotwiczenie wirów w  $\text{SmBa}_2\text{Cu}_3\text{O}_{7-\delta}$  oraz  $\text{NdBa}_2\text{Cu}_3\text{O}_{7-\delta}$ , gdzie kotwiczenie na defektach w postaci wytrąceń roztworów stałych (ang.: *solid solution*)  $(\text{Nd,Sm})_{1+y}\text{Ba}_{2-y}\text{Cu}_3\text{O}_{7-\delta}$  jest prawdopodobnie odpowiedzialne za efekt wzrostu wartości prądu krytycznego dla wyższych pól (tzw. *fishtail effect*). Przypuszcza się, iż wytrącenia takich roztworów prowadzić mogą do magnetycznej modulacji ładunku w postaci wstęg ładunkowych (ang.: *stripes*). W temperaturach bliskich  $T_c$  centra kotwiczenia w monokryształach  $(\text{Nd,Sm})\text{Ba}_2\text{Cu}_3\text{O}_{7-\delta}$  są bardziej efektywne niż te w  $\text{YBa}_2\text{Cu}_3\text{O}_{7-\delta}$ .



## 1. Introduction

Three years after the successful liquefying of helium in 1908, superconductivity in mercury was discovered [1]. Soon it was found that the phenomena of superconductivity appears in many elements among which Nb possesses the highest transition temperature  $T_c$  of 9.2 K (at ambient pressure). The first attempt to describe the electrodynamic properties of the superconducting state was the phenomenological London theory [2]. In 1950 the phenomenological Ginzburg-Landau (GL) theory of superconductivity was devised [3] while the microscopic theory was proposed by Bardeen, Cooper, and Schrieffer (BCS theory) in 1957 [4]. The conventional electron-phonon interaction for electron pairing has been suggested to allow a maximum  $T_c$  of roughly only 30 K without triggering a lattice instability catastrophe [5,6]. Compound of  $\text{Nb}_3\text{Ge}$  possess the highest  $T_c = 23$  K [7]. In 1986,  $T_c$  limits raised up to about 35 K with the discovery of superconductivity in La-Ba-Cu-O by Bednorz and Müller [8]. Immediately afterwards, the search for superconductivity in materials of similar structure began, and a few months later the dream of a superconductor with a transition temperature higher than 77 K became true, namely  $\text{YBa}_2\text{Cu}_3\text{O}_{7-\delta}$  compound was born [9]. As a result of great scientific effort,  $T_c$  raised up to 133 K at the ambient pressure for  $\text{HgBa}_2\text{Ca}_2\text{Cu}_3\text{O}_{1+x}$  [10] and later reached its highest value observed so far of 138 K in Tl-doped  $\text{HgBa}_2\text{Ca}_2\text{Cu}_3\text{O}_{7+\delta}$  [11].

On the theoretical part, the first important step in understanding the cuprates was made by Anderson [12]. He identified the key feature of new superconductors that are the  $\text{CuO}_2$  planes with a weak interplane coupling. The theories proposed to explain that new behaviour have been getting increasingly sophisticated and the basic question of what is the origin of superconductivity in materials with the  $\text{CuO}_2$  planes, the cuprates, still remains open [13].

In 2001 superconductivity in  $\text{MgB}_2$ , a material where two distinct Fermi sheets are responsible for superconducting properties [14,15,16,17], was discovered [18]. Lately, superconductivity in the family of the pnictides, materials with the iron-based planes, was revealed [19]. Eighteen months after superconductivity was found in  $\text{MgB}_2$ , an almost complete theory explaining observed properties was proposed [20]. During two years into the ‘iron age’, very extensive research was conducted [21,22]. Twenty four years after the discovery of superconductivity in the cuprates, the mechanism, that binds the charge carriers together, is a matter of an intensive discussion. In conventional superconductors, the interaction occurs due to phonons, however in the case of high- $T_c$  superconductors

(HTSC), polarons [23] or magnetic origin [24,25] were suggested. Moreover, questions of what is the carriers' pairing symmetry, why  $\text{GdBa}_2\text{Cu}_3\text{O}_{7-\delta}$  does and  $\text{PrBa}_2\text{Cu}_3\text{O}_{7-\delta}$  does not superconduct, are the cuprates multiband superconductors, and what is the Fermi surface in underdoped regime, are calling for an answer. There are striking similarities between three groups of HTSC, i.e.  $\text{MgB}_2$ , the pnictides, and the cuprates. They all possess a layered structure while the latter two are characterized by similar phase diagrams of temperature versus charge carrier concentrations. Moreover, superconductivity develops when magnetism is destroyed by doping [26,27]. The discovery of temperature dependence of both the anisotropy parameter and multiband superconductivity in  $\text{MgB}_2$  as well as in the pnictides stimulate new research in the cuprates that could help understand physics of unconventional superconductors. The aim of this thesis is to present results of the study of temperature dependence of the anisotropy parameter, influence of magnetic ions on the superconducting state properties, and characteristics of vortex pinning in the cuprates.

The experimental results obtained for HTSC, due to lack of a corresponding microscopic theory, are described within the framework of phenomenological anisotropic Ginzburg-Landau theory (AGLT). According to AGLT a superconductor is characterized by the anisotropy parameter of the effective mass of the superconducting carriers,  $\gamma$ . Although the theory is successfully applied to many systems, it does account for neither the occurrence of an in-plane anisotropy in the tetragonal basal plane nor the positive curvature of the temperature dependence of upper critical field  $H_{c2}(T)$ . These phenomena were observed in several materials. The limitations for application of AGLT became the most apparent after the discovery of superconductivity in the magnesium diboride and in the pnictides. In both these superconductors, a strong temperature dependence of the anisotropy parameter was found. The origin of this phenomenon is two-band superconductivity in  $\text{MgB}_2$  and, presumably, also in the iron-based superconductors. There has been no clear evidence for a temperature dependence of the anisotropy parameter for the longest known HTSC's, i.e. the cuprates. Therefore, the general question is whether or not the temperature dependence of the anisotropy parameter is a common feature of HTSC. Dissertation presents results of the first studies of the  $\gamma(T)$  for underdoped cuprates in a wide range of temperatures.

The HTSC (type II superconductors) can carry critical current densities,  $J_c$ , that are higher by a factor of 10 at temperature of 4 K in comparison to conventional ones. However,  $J_c(T)$  strongly decreases at high temperatures in these materials. Separation of the magnetic phase diagram into a region where dissipation-free current transport is possible and into

a region, where the superconductor behaves completely reversible is defined by an irreversibility line. Thermal fluctuations of vortex lattice at high temperatures strongly decreases the  $J_c$ . Several methods may be used to obtain the required increase of  $J_c$  and shift of the irreversibility line to higher temperatures and fields. Some of them involve introduction of neutron, proton or heavy-ion irradiation defects [28,29,30,31,32], nanoscale normal regions like Y211 [33], chemical substitutions [34,35,36,37] or variation of the superconducting carrier concentration [38]. The superconducting carrier concentration may be changed by varying oxygen deficiencies,  $\delta$ , for superconducting  $\text{REBa}_2\text{Cu}_3\text{O}_{7-\delta}$ , where RE is a rare earth or Y ion. In this work, focus was drawn to the problem of how chemical substitution and oxygen content modify the  $H(T)$  phase diagram.

The  $\text{REBa}_2\text{Cu}_3\text{O}_{7-\delta}$  (RE123, RE – a rare earth or Y ion) shows superconducting properties only for a narrow range of the oxygen content. Moreover, the dependence of the thermodynamic parameters (e.g.  $T_c$  or the anisotropy) on the oxygenation level has been so far validated only for Y123. The phase diagram of  $T_c$  versus charge carrier concentration, i.e. oxygen content, remains unknown for Sm123, the material to which a lot of attention was drawn in recent years due to its high critical current density. The substitution of Y ions by Sm, does not change the value of  $T_c$  significantly in optimally oxygenated Y123 but the introduced Sm ions act as the effective pinning centres. Therefore, extrinsic parameters of Y123 and Sm123 are compared here.

The question whether magnetism and superconductivity can coexist was first posted by Ginzburg in 1957 [39] and the influence of magnetic impurities on superconductivity was studied by Abrikosov and Gorkov [40]. Whenever a ferromagnet is in contact with a superconductor, the Cooper pairs from the superconductor are not expected to survive beyond at most a few nanometres into the ferromagnet. Antiferromagnetism (AFM) is more relevant to HTSC than ferromagnetism (FM), because superconductivity in the cuprates and the pnictides arises from electron- or hole-doping of their AFM parent compounds [41,42]. Antiferromagnetic order is less pair-breaking than FM, thus many examples of superconductivity coexisting with antiferromagnetic order are known and have been recently reviewed [43]. In RE123, the transition temperature is unaffected by a local magnetic moment on the RE ion apart from Ce, Pr, and Tb ions. Despite the fact that RE ions order antiferromagnetically, the exchange interaction between RE ions spins and superconducting electrons is small [44]. However, superconductivity in Y123 disappears for substitution of around 54% of Y by Pr in Y123 due to unknown reasons [45,46,47,48,49]. Nevertheless, for

a low level Pr substitutions additional pinning centres are expected to be introduced into Y123 via Pr ions, which should lead to an increase of  $J_c$ . At the same time,  $T_c$  as high as possible is preferential. The problem of how the thermodynamic parameters of the cuprates are influenced by a small praseodymium ion concentration was subject of presented studies.

The aim of this dissertation was to characterize compounds of RE123 superconductors. Specifically, the work presents the oxygen deficiency effect in Sm123, the influence of a partial substitution of Y by magnetic ions in Y123 system, and the influence of different rare earth itself on the superconducting state parameters of RE123 were studied. Intrinsic parameters, i.e. coherence length, penetration depth, lower and upper critical fields, thermodynamic critical field, anisotropy parameter, and the Ginzburg-Landau parameter were investigated. Additionally, extrinsic parameters, i.e. the critical current density, irreversibility field, and the pinning force density, were examined. Due to the availability of large size single crystals, the trapped field profiles were investigated.

The investigations were carried out on single crystals, necessary for study of anisotropic properties. Several methods, namely SQUID and torque magnetometry, AC susceptibility, and Hallscan technique, were employed.

This work is organized as follows: Section 2 consists of a short theoretical introduction. In Sections 3 and 4 the description of the experimental methods and characteristics of RE123 single crystals are presented, respectively. Various methods of evaluation of the superconducting state parameters are introduced in Section 5. Sections 6, 7, and 8 describe obtained experimental results. Final conclusions are drawn in Section 9.



## 2. Theoretical background

There are two basic properties that distinguish a superconductor from other materials, namely the perfect conductivity (observed for the first time in 1911 for mercury) and the ideal diamagnetism (discovered in 1933 and known as Meissner effect). Meissner and Ochsenfeld [50] found that not only a magnetic field is excluded from entering a superconductor, as might be explained by perfect conductivity. Additionally, the field in the sample that was normal conducting above a critical temperature  $T_c$  is expelled as it is cooled through  $T_c$ . Experimentally it was shown that a small magnetic field in a superconductor is not fully expelled, but the screening current flows at the surface and the superconductor is in the so-called “Meissner state”, close to a perfect diamagnet ( $B = \mu_0(H + M) \approx 0$ , where  $\mu_0$  is the magnetic permeability in vacuum). By their physical properties, superconductors can be type I or type II. When the field  $H$  exceeds a characteristic value superconductivity is destroyed in type I superconductors ( $H > H_c$ ), but enters so-called mixed or Shubnikov phase in type II materials ( $H > H_{c1}$ ), which is still a superconducting state up to  $H_{c2}$ , see Fig. 2.1. The magnetic flux penetrates a superconductor in the mixed state in the form of quantized flux lines called vortices. The vortices can be thought of cylinders with a normal conducting core placed in the direction of applied field. Thus, coexistence of the superconducting with normal phase occurs and vortices pointing into the same direction repel each other [7]. As it was first demonstrated experimentally in 1967 [51], triangular array of flux lines, called Abrikosov lattice, is preferential over the square one.

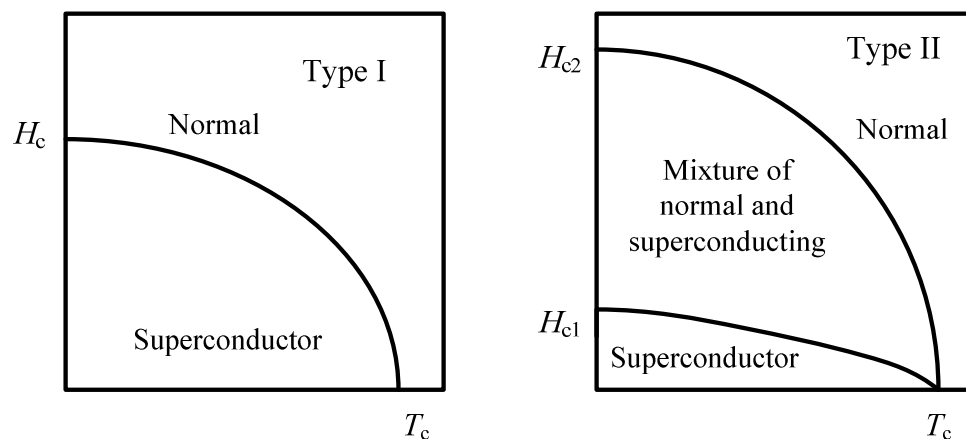


**Fig. 2.1.** Schematic comparison of  $H$ - $T$  phase diagram for type I (left) and type II (right) superconductors.

In reality, the phase diagram of type II superconductors is more complex than the one presented in Fig. 2.1, see Section 2.4 for details. The nature of different vortex phases and the thermodynamic transitions between them are of fundamental interest and subject of substantial theoretical and experimental studies [52,53,54].

## 2.1. London model

The phenomenological theory of Fritz and Heinz London was the first attempt to describe the electrodynamic properties of a superconducting state. They showed that the Meissner effect is a consequence of the minimalization of the electromagnetic free energy carried by superconducting current [2]. They proposed two equations

$$\bar{\mathbf{E}} = \frac{\partial}{\partial t} \left( \frac{m}{n_s^* e^{*2}} \bar{\mathbf{J}}_s \right), \quad (2.1.1)$$

$$\bar{\mathbf{H}} = -\nabla \times \left( \frac{m}{\mu_0 n_s^* e^{*2}} \bar{\mathbf{J}}_s \right), \quad (2.1.2)$$

where  $m$  denotes the electron mass,  $e^*$  is the charge of the superfluid carriers,  $n_s^*$  is the density of superconducting carriers, and  $\bar{\mathbf{J}}_s$  is the vector density of circulating supercurrents. The first equation describes perfect conductivity since any electric field accelerates the superconducting electrons. The second equation combined with the Maxwell equation  $\nabla \times \bar{\mathbf{H}} = \bar{\mathbf{J}}$  leads to exponential screening of the magnetic field from the interior of a sample with a characteristic distance denoted as  $\lambda$ , called the penetration depth, and defined by  $\lambda = (m^*/\mu_0 n_s^* e^{*2})^{1/2}$ , where  $m^*$  denotes the electron effective mass. London equations describe distribution of the magnetic field at a constant temperature and in the case when the number of superconducting electrons remains constant, i.e.  $n_s^*$  is uncorrelated with the applied field or the flowing current.

The total free energy density, in the reversible region, of a type II superconductor in magnetic field  $H_{c1} \ll H \ll H_{c2}$  is given by following equation [7]:

$$f(H) = \frac{\mu_0 H^2}{2} - \frac{\Phi_0 H}{8\pi\lambda^2} \ln \left( \frac{\eta H_{c2}}{H} \right), \quad (2.1.3)$$

where  $\eta$  is a numerical parameter of the order of unity depending on the structure of the flux-line lattice [55] which takes into account the uncertainty in defining size of the vortex

core [56]. The magnetic induction  $B$  is related to the magnetic field  $H$  and the magnetization  $M$  of the sample through  $B = \mu_0(H + M)$ . Equation (2.1.3) yields directly the magnetization since  $B = \partial f / \partial H$  and  $M = B / \mu_0 - H$ . For an anisotropic superconductor with magnetic field  $H_{c1} \ll H \ll H_{c2}$  applied along main crystallographic axes following equations hold:

$$M^{\parallel c} = -\frac{\Phi_0}{8\pi\mu_0\lambda_a\lambda_b} \ln\left(\frac{\eta H_{c2}^{\parallel c}}{H}\right), \quad (2.1.4)$$

$$M^{\parallel b} = -\frac{\Phi_0}{8\pi\mu_0\lambda_a\lambda_c} \ln\left(\frac{\eta H_{c2}^{\parallel b}}{H}\right), \quad (2.1.5)$$

$$M^{\parallel a} = -\frac{\Phi_0}{8\pi\mu_0\lambda_b\lambda_c} \ln\left(\frac{\eta H_{c2}^{\parallel a}}{H}\right). \quad (2.1.6)$$

Here,  $\lambda_a$ ,  $\lambda_b$ , and  $\lambda_c$  are the penetration depths related to supercurrents flowing along the  $a$ -,  $b$ -, and  $c$ -axis, respectively;  $H_{c2}^{\parallel a}$ ,  $H_{c2}^{\parallel b}$ , and  $H_{c2}^{\parallel c}$  are the upper critical fields for  $H$  applied along the  $a$ -,  $b$ -, and  $c$ -axis, respectively. For superconductors with uniaxial anisotropy, as in the case of HTSC,  $\lambda_a = \lambda_b = \lambda_{ab}$  and the three above equations reduce to two, i.e. equations for  $M^{\parallel c}$  and  $M^{\parallel ab}$ . The anisotropic behaviour of a layered superconductor can be characterized by the anisotropy parameter,  $\gamma$ , according to:

$$\gamma = \sqrt{\frac{m_c^*}{m_{ab}^*}} = \frac{\lambda_c}{\lambda_{ab}} = \frac{H_{c2}^{\parallel ab}}{H_{c2}^{\parallel c}} = \frac{\xi_{ab}}{\xi_c}. \quad (2.1.7)$$

Here,  $m_{ab}^*$  and  $m_c^*$  are the effective charge carrier masses related to supercurrents flowing in the  $ab$ -planes and along the  $c$ -axis, respectively; and  $\xi_{ab}$  and  $\xi_c$  are the corresponding coherence lengths. Then, GL parameter,  $\kappa$ , can be defined as:

$$\kappa^{\parallel c} = \frac{\lambda_{ab}}{\xi_{ab}}, \quad (2.1.8)$$

$$\kappa^{\parallel ab} = \sqrt{\frac{\lambda_{ab}\lambda_c}{\xi_{ab}\xi_c}}. \quad (2.1.9)$$

When the magnetic field is not applied along the main crystallographic axis, following scaling transformation  $B \rightarrow \varepsilon_\theta B$  holds, see e.g. [52], where:

$$\varepsilon_\theta = \sqrt{\cos^2(\theta) + \frac{1}{\gamma^2} \sin^2(\theta)}. \quad (2.1.10)$$



In such case, the free energy,  $f$ , is a function of the angle  $\theta$  between the magnetic field and the  $c$ -axis of the crystal. Then, the magnetic torque density,  $\tau$ , can be introduced due to the relation:  $\tau = -\partial f / \partial \theta$ . Torque in the reversible regime for fields  $H_{c1} \ll H \ll H_{c2}$  was first calculated by Kogan *et al.* [57,58,59] within the 3D anisotropic London model approach. It was found that the magnetic torque density equals:

$$\tau = \bar{M} \times \bar{B} = -\frac{VH\Phi_0}{16\pi\lambda_{ab}^2} \left(1 - \frac{1}{\gamma^2}\right) \frac{\sin 2\theta}{\varepsilon_\theta} \ln \left( \frac{\eta H_{c2}^{\parallel c}}{\varepsilon_\theta H} \right), \quad (2.1.11)$$

where  $\mu_0 H = B$  is used. Here,  $V$  is the volume of the crystals and  $\Phi_0$  is the flux quantum.

## 2.2. Ginzburg-Landau theory

In 1950 Ginzburg and Landau proposed a phenomenological theory [3] where a complex pseudo-wave function  $\Psi$  with  $|\Psi|^2$  as an order parameter, was introduced. The order parameter in GL theory describes the local density of superconducting electrons, later revised to be Cooper pairs [60], since  $n_s = |\Psi|^2$ . The basic postulate of GL theory is that if  $\Psi$  is small and varies slowly in space, the free energy density in the superconducting state is lower than the one corresponding to the normal state,  $f_n$ , and can be presented as follows:

$$f(\bar{H}) = f_n(0) + \alpha |\Psi|^2 + \frac{\beta}{2} |\Psi|^4 + \frac{1}{2m^*} \left| \left( \frac{\hbar}{i} \nabla - e^* \bar{A} \right) \Psi \right|^2 + \frac{\mu_0 \bar{H}^2}{2}. \quad (2.2.1)$$

Here  $\alpha$  and  $\beta$  are constants defined within the Landau theory of phase transitions [61] related to the squared modulus of the wave function,  $\hbar$  is the Planck's constant, and  $\bar{A}$  is the vector potential of magnetic field, i.e.  $\mu_0 \bar{H} = \nabla \times \bar{A}$ . The zero-field difference between the free energy of normal and superconducting states equals  $\mu_0 H_c^2 / 2$  where  $H_c$  is the thermodynamic critical field. Derivatives of Eq. (2.2.1) over  $\bar{A}$  and  $\Psi$  lead to two GL equations:

$$\alpha |\Psi| + \beta |\Psi|^2 \Psi + \frac{1}{2m^*} \left( \frac{\hbar}{i} \nabla - e^* \bar{A} \right)^2 \Psi = 0, \quad (2.2.2)$$

$$\bar{J}_s = \nabla \times \bar{H} = \frac{e^*}{m^*} \left[ \Psi \left( \frac{\hbar}{i} \nabla - e^* \bar{A} \right) \Psi \right]. \quad (2.2.3)$$

The GL theory defines two characteristic lengths: (i) length for variation of  $\Psi$  (or  $f$ ),  $\xi(T)$ , and (ii) the magnetic penetration depth,  $\lambda(T)$ . Both quantities diverge at  $T_c$ . The  $\xi(T)$  defines the characteristic decay of  $|\Psi|$ , equivalent to decay of the superconducting charge

density, at a boundary between normal ( $n$ ) and superconducting ( $s$ ) state. The penetration depth determines the characteristic variation of magnetic field at the  $n - s$  boundary and describes change in the density of the superconducting shielding currents flowing parallel to the edges of sample. Additionally, the ratio of two characteristic lengths is introduced as dimensionless GL parameter  $\kappa = \lambda/\xi$ . Abrikosov showed [62] that GL theory predicts two types of superconductors. For  $\kappa > 1/\sqrt{2}$ , there is a negative surface energy associated with a domain wall between normal and superconducting state that leads to subdivision into domains of normal and superconducting regions (type II superconductors). In the case of small  $\kappa$ , i.e.  $\kappa < 1/\sqrt{2}$ , there is a positive surface energy and subdivision into domains is energetically unfavourable (type I). Another result of Abrikosov's analysis was that, in the mixed state, the flux penetrate a superconductor in a regular array of flux tubes, each carrying a quantum of flux equal to:

$$\Phi_0 = \frac{\hbar}{2e} \approx 2.07 \times 10^{-15} \text{ Tm}^2. \quad (2.2.4)$$

Anisotropic superconductors are described by the anisotropic Ginzburg-Landau theory (AGLT). In this theory the effective mass from Eq. (2.2.1) is replaced by an effective mass tensor with values  $m_a^*$ ,  $m_b^*$ , and  $m_c^*$  along the main crystallographic axes.

The phenomenological GL theory successfully explains the macroscopic properties of many superconductors. Physical meaning of the superconducting state parameters, that can be probed experimentally and evaluated using GL theory, is explained by microscopic theory of superconductivity formulated by Bardeen, Cooper, and Schrieffer in the so-called BCS theory. For layered superconductors with extremely high anisotropy, the Lawrence-Doniach (LD) approach [63] is more appropriate than AGLT. In the LD approach the material is treated as a stack of two-dimensional (2D) superconducting layers, which are only weakly coupled together by tunnelling of Cooper pairs (similar to the Josephson effect [64]). In the limit of low anisotropy, the Lawrence-Doniach approach reduces to the AGLT, that describes superconducting layers as a continuous 3D medium. The crossover, where the discreteness of the layers starts to become important, occurs when the coherence length perpendicular to the layers,  $\xi_c$ , becomes comparable to the distance between the superconducting layers,  $s$ .

### 2.3. Superconductor in a magnetic field

In magnetic field  $H \geq H_{c1}$  a type II superconductor enters the mixed state and vortices start to penetrate it (Fig. 2.1). As long as the separation of flux lines is large compared to  $\lambda$ , there is no significant interaction between vortices. In such case, the superconducting state parameters can be determined by solving GL equations:

$$\mu_0 H_{c1}^{\parallel c} = \frac{\Phi_0}{4\pi\lambda_{ab}^2} (\ln \kappa^{\parallel c} + \varepsilon), \quad (2.3.1)$$

$$\mu_0 H_{c1}^{\parallel ab} = \frac{\Phi_0}{4\pi\lambda_{ab}\lambda_c} (\ln \kappa^{\parallel ab} + \varepsilon), \quad (2.3.2)$$

$$\mu_0 H_{c2}^{\parallel c} = \frac{\Phi_0}{2\pi\xi_{ab}^2}, \quad (2.3.3)$$

$$\mu_0 H_{c2}^{\parallel ab} = \frac{\Phi_0}{2\pi\xi_{ab}\xi_c}, \quad (2.3.4)$$

$$\mu_0 H_c = \frac{\mu_0 H_{c2}^{\parallel ab}}{\sqrt{2}\kappa^{\parallel ab}} = \frac{\mu_0 H_{c2}^{\parallel c}}{\sqrt{2}\kappa^{\parallel c}}. \quad (2.3.5)$$

The parameter  $\varepsilon$  describes interaction between flux lines' cores. Brandt [65] provided an interpolation formula for this quantity and estimated it to be  $\varepsilon \approx 0.5$ .

The Lorentz force,  $F_L = J_c B$ , acts on a flux-line and flux lines tend to move [66,67]. In such case, a type II superconductor shows non-zero resistance and is unable to sustain a persistent current unless some mechanism exists which prevents the Lorentz force from moving the vortices. For strong field  $H$  close to  $H_{c2}$ , vortex cores start to overlap and it is a real problem to make such superconductor to carry a useful high current without energy dissipation.

### 2.4. Flux-line pinning

Pinning centres like vacancies in the crystal lattice, dislocations or normal conducting inclusions, cause local variation of the free energy. In general, pinning of vortices to a fixed location in the material results from any spatial inhomogeneity of the material due to local variations of  $\xi$ ,  $\lambda$ , or  $H_c$ . The most energetically favourable state is when the vortex is placed onto a small defect of size of the order of  $\xi$  as then the condensation energy  $H_c^2/2$  is saved in the volume of the defect. Different pinning mechanisms are due to different interaction of defects with the vortices at varying temperature [7,52,68]. Pinning associated with a spatial

variation of the superconducting transition temperature throughout the sample is usually denoted as  $\delta T_c$ , while the one associated with a variation of the upper critical field as  $\delta H_c$ . Knowledge of the pinning mechanisms is crucial for understanding the field and temperature dependence of the critical current density.

A type II superconductor enters so-called ‘‘Bragg glass’’ phase at temperatures significantly lower than  $T_c$  and when external magnetic field exceeds  $H_{c1}$ . The critical current density is low in this quasi-ordered phase. The Bragg glass transforms into a ‘‘disordered glass’’ phase with increasing magnetic field. The disordered glass phase is characterized by much higher critical current density compared to the Bragg glass phase. Characteristic field at which the order-to-disorder vortex lattice transition occurs,  $H_{OD}$ , is often marked by the fishtail effect, see e.g. Ref. [69].

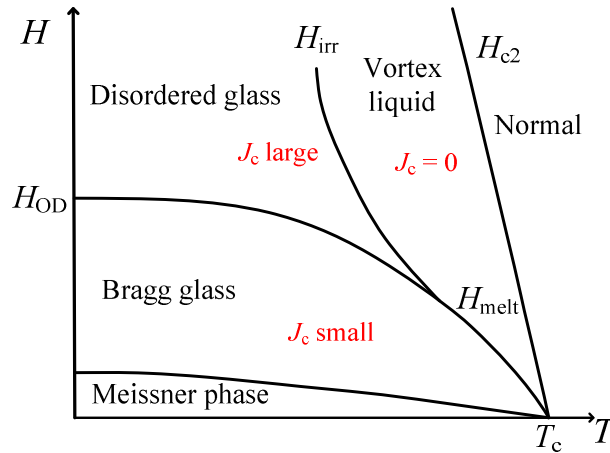


**Fig. 2.4.1.** Phase diagram of a high- $T_c$  superconductor.

At temperatures close to  $T_c$ , depinning force is greater than pinning force of vortices on defects and the vortex structure resembles liquid. Two characteristic fields are recognized at high temperatures, namely the irreversibility field,  $H_{irr}$ , and the field of a vortex lattice-to-melting phase transition,  $H_{melt}$  (Fig. 2.4.1). The relationship between  $H_{irr}(T)$  and  $H_{melt}(T)$  was for a long time a subject of an intensive investigation, see e.g. [70,71,72,73].

Strong pinning, which prevents electrical resistance, defines the irreversibility line  $H_{irr}(T)$ . This line divides the  $(H,T)$ -plane into regions where the critical current equals zero and where  $J_c$  is greater than zero, respectively, see Fig. 2.4.1. Among many HTSC,

the highest, in respect to fields and temperatures, lying  $H_{\text{irr}}(T)$  lines have been found for RE123 superconductors [74].

Not all pinning sites are effective at low magnetic fields, thus, vortices start to move at temperatures above the melting temperature,  $T_{\text{melt}}(H)$ , and the flux-line lattice disappears [75]. The large anisotropy parameter  $\gamma$  and the high temperature are the primary factors which depress the melting field much below  $H_{c2}$  in the HTSC. The first-order vortex melting transition has been evidenced in various experiments [76,77,78,79,80,81].

A lot of difficulties in the description of the vortex pinning arise when sample is characterized by a large anisotropy. For example the high- $T_c$  superconductors with copper oxides planes, i.e. cuprates, have layered structure and a very short coherence length  $\xi_c$  of the order of a few nanometres. Then, the three-dimensional GL theory for a long-wavelength phenomena may not hold and the 2D LD model [63] may be more suitable. Extreme anisotropy means that vortices act more like a weakly correlated stack of vortex 'pancakes' rather than a line, making them even harder to pin [82].

The pinning of vortex lattice on defects is not effective when large thermal fluctuations are acting on vortex lines. The strength of thermal fluctuations is described by the so-called Ginzburg number [83]:

$$Gi = \frac{1}{2} \left( \frac{\gamma k_B T_c}{H_c(0)^2 \xi_{ab}(0)^3} \right)^2. \quad (2.4.2)$$

While this dimensionless quantity is of the order of  $10^{-10}$  to  $10^{-7}$  in low  $T_c$  superconductors [84,85], it can become larger than  $10^{-2}$  in the cuprates [83]. This is due to the higher  $T_c$ , the very short coherence length, and the pronounced anisotropy in HTSC [86,87].

## 2.5. Intrinsic pinning

Significant role of the layered structure in HTSC is the consequence of a very short coherence length, i.e.  $\xi_c(T) < s$ , and a large anisotropy. For magnetic field applied along the  $ab$ -plane, a strong intrinsic pinning of the vortices appears, which results in a lock-in of vortex lines or kinked state of vortices. From the thermodynamical point of view, it is more favourable to place the flux lines between superconducting layers than into them.

The intrinsic pinning of the vortices originates from a modulation of the order parameter in the direction perpendicular to the layers [88]. Pinning by planar structures occurs

when the magnetic field is nearly parallel to the  $\text{CuO}_2$  planes, namely, when the misalignment of the field from the planes does not exceed a critical angle  $\theta$ , see Fig. 2.5.1 [89,90,91]. More precisely, two critical angles are distinguishable and the flux line lattice penetrating HTSC undergoes dramatic changes when the direction of the magnetic field approaches the  $\text{CuO}_2$  planes [92]. First, at very small angles, i.e. for magnetic fields very close to  $H \parallel ab$ , and when pinning by the layered structure becomes strong enough, vortices become confined between the  $\text{CuO}_2$  planes. The lock-in transition occurs for angles smaller than the lock-in angle given by following relation:

$$\theta_{\text{lock}} = \arcsin\left(\frac{H_{c1}(1-D)}{H}\right), \quad (2.5.1)$$

where  $D$  denotes the demagnetizing coefficient, see Section 5. For angles greater than  $\theta_{\text{lock}}$ , the tilt energy associated with kink formation [93] is balanced by the core energy gained by forming vortex segments parallel to the layers [94]. This leads to tilting of the vortex lattice at angles  $\theta_{\text{lock}} < \theta < \theta_{\text{kink}}$  [91] and vortex lines consist of Josephson vortices parallel to the  $ab$ -plane (of the length of  $d \tan \theta$ ) and short London kinks parallel to the  $c$ -axis, see Fig. 2.5.1 [95,96,97]. In total, four different vortex states were reported depending on whether the applied field components parallel and perpendicular to the superconducting planes are higher or lower than the respective lower critical fields  $H_{c1}^{\parallel ab}$  and  $H_{c1}^{\parallel c}$ , see [52] and [92] and references therein.

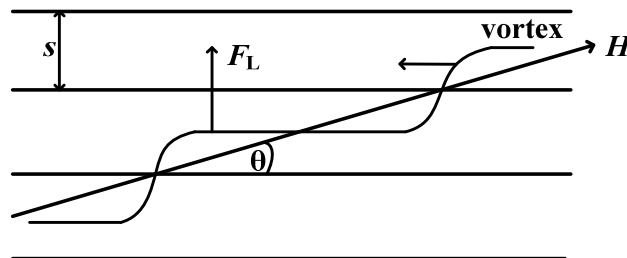


**Fig. 2.5.1.** Schematic diagram of kinks along a vortex line, where  $\theta$  is the angle between the magnetic field and the  $ab$ -plane and  $F_L$  is the Lorentz force acting on vortices parallel to the layers. The small arrow represents the motion of the kinks.

## 2.6. Bean model

The magnetization of a type II superconductor is always determined by the sum of two contributions, namely the reversible magnetization and the magnetization due to the critical

currents. The former is an equilibrium material property while the latter expresses itself in the hysteresis of magnetization loops. The evaluation of the critical current is based on the time independent form of the fourth Maxwell equation  $\nabla \times \vec{H} = \vec{J}$ . It is a more than challenging task to find a general solution for  $J_c(B)$  for arbitrary geometry. A detailed analysis of the functional dependence of the magnetization on the applied magnetic field is difficult in HTSC because of varying vortex phases, varying pinning force behaviour over the  $(B, T)$  plane, and fluctuations of the vortex lattice. The most commonly used simplified model is the Bean model [98].

The Bean model in its basic form assumes a field independent critical current density  $J_c$ . Under this condition, the field profile in an infinitely long cylindrical sample can be simply estimated. There exists only one field slope  $dH_{\text{irrev}}/dr$  equals  $J_c$ . Here, the external field is applied along the axis of the cylinder and  $r$  is a distance from the cylinder core. When the external field is raised from zero to a small value, flux enters the sample from the border until the sample is fully penetrated at  $H^*$ . Then, the shielding current  $J_c$  flows homogeneously. Above  $H^*$ , the magnetic moment does not change with increasing field. After lowering the field following  $H_{\text{max}}$ , flux leaves the sample until at  $H = H_{\text{max}} - 2H^*$  the current flow is again homogeneous. The magnetic moment does not change below this field, leading to the remnant moment at  $H$  equals zero. The magnetic moment  $m(H)$  (or magnetization  $M(H)$ , where  $M = m/V$ ) is calculated as the integral of the local field over the sample volume. These considerations allow a straightforward evaluation of  $J_c$  from experimental  $m(H)$  (consequently,  $m(B)$ ) data. For rectangular samples, where  $a$  and  $b$  are the sample dimensions perpendicular to the applied field and  $a \geq b$ , following relation holds:

$$J_c(B) = \frac{m(B)}{V} \frac{12a}{b(3a-b)}. \quad (2.6.1)$$

Usually, in order to eliminate the contribution of the reversible magnetic moment  $m_{\text{rev}}$ , the magnetic moment is measured in increasing field  $m_{\uparrow} = -m + m_{\text{rev}}$  and in decreasing field  $m_{\downarrow} = m + m_{\text{rev}}$ . The half of the difference between these two cancels  $m_{\text{rev}}$ .

An extended model for the critical current was proposed by Kim *et al.* [99,100]. The Kim model assumes that the critical current density depends on the internal magnetic field through:

$$J_c(B) = \frac{J_c}{1 + |B(x)|/B_K}, \quad (2.6.2)$$

where  $B(x)$  is the position dependence of the internal field and  $B_K$  is a magnetic field parameter. Unfortunately the Kim model did not turn out as practically useful as the Bean model and, in fact, the studies based on the Kim model remains limited mainly to the theoretical type of work in the areas like the low-field AC susceptibility [101] and fishtail effect [102]. There are two main reasons for the less practical usefulness of the Kim model. The first is that the two constants, which are involved in this model,  $J_c$  and  $B_K$ , are tied by single equation, therefore, cannot be calculated as independent of one another. The second reason lies in the fact that in some cases an infinite value for the critical current density may be obtained, which is unphysical.

Only in the high-field regime, where magnetization is weakly field-dependent, the Bean model yields reasonably accurate values for  $J_c(B)$ . Complications in the  $M(H)$  analysis occur at fields of the order of  $H_{c1}$  and in regimes of large spatial flux gradients. These complications arise due to demagnetization and barrier effects in the plate-like single crystals. Near  $T_c$ , bulk pinning is very weak and contribution to hysteresis from surface or geometrical barriers dominate. Geometrical barriers (GB) [103,104] result in vortices first penetrating the sample diagonally across the corners and lead to a delayed penetration field. GB are important in case of non-ellipsoidal sample geometry. The gradient in magnetic potential that the vortices experience once they have penetrated the sample drives them to its centre. This (macroscopic) barrier also leads to retarded flux entry and to irreversibility in the magnetization at lower fields. Surface barriers were investigated by Bean and Livingston [105] and unlike GB, arise from a competition between two forces. The Lorentz force of the Meissner screening current drives vortices into the sample. The attractive interaction between vortices and their image acts repulsively on a vortex near the sample surface. The first force outweighs the second one for small fields  $H$  less than  $H_p$ . Here,  $H_p$  is greater than the lower critical field and is called the field of first penetration.

The Bean model does not take into account the actual influence of the external field on the magnetic response of the superconducting material, namely a strong dependence  $J_c(B)$ . In particular, the Bean model does not account for an increase of the critical current density with increasing field up to  $H_{\text{peak}}$  (or, equivalently,  $B_{\text{peak}}$ ), i.e. fishtail or peak effect (PE). Phenomena of the PE was reported for many superconductors while it was first observed in



Nb-Zr alloys [106]. More accurate model for the analysis of the magnetization behaviour is needed to describe this phenomenon.

## 2.7. Rigorous analysis of the isothermal $M(H)$

An accurate analysis of the fundamental (equilibrium) properties and the vortex pinning behaviour requires the knowledge of the constitutive relations of the equilibrium magnetic induction,  $B_{\text{eq}}(H,T)$ , or of the equilibrium magnetization,  $M_{\text{eq}}(H,T)$ , and of the demagnetization effects. The equilibrium properties of HTSC may be evaluated, at least approximately, using the Ginzburg-Landau theory with a single temperature and field-independent GL parameter  $\kappa$ . The equation for  $B_{\text{eq}}(H)$  may be obtained from a numerical solution of the Ginzburg-Landau theory presented by Hao and Clem [107]. An extension of the Hao-Clem analysis is the Labusch-Doyle [108] treatment that gives more accurate values at low fields. An alternative analysis is a numerical treatment performed by Brandt [109], who introduced an iterative approach that allows to calculate the form factors of magnetic field and order parameter. The magnetization scaling treatment yields reasonably good estimates for the equilibrium and the vortex pinning parameters in regions of the  $(B,T)$  plane where vortex fluctuations are not prevalent. The non-equilibrium properties may be obtained by introducing vortex pinning phenomena into the analysis. In general, fitting of the reduced experimental magnetization isotherms  $M/X$  and  $H/X$  to the numerical solution of GL equations ( $X$  is set to be  $H_{c2}$  in the Hao-Clem and Brandt models and  $H_{c1}$  in the Labusch-Doyle treatment) may be done in two stages, namely:

(i) establish equilibrium values for the superconducting state parameters, see Fig. 2.7.1a. First, mean values of the experimental magnetization, i.e.  $M_{\text{rev}}(H)$  isotherms, are reduced by the fitting parameter  $X$ . Second, the numerical solution of the GL equations with a suitably chosen equation for  $B_{\text{eq}}(H)$  is computed and compared with the isotherms. The fitting leads to the  $X$  and  $\kappa$  values;

(ii) establish non-equilibrium pinning parameters, see Fig. 2.7.1b. Experimentally obtained values of  $M(H)$  are reduced by  $X$ . Equations for  $B_{\text{eq}}(H)$  and  $J_c(B,T)$  are used in the computation of the numerical solution of the GL equations. The fitting of the experimental data to the theoretical  $M(H)$  allows determination of the vortex pinning parameters used in  $J_c(B,T)$  formula.

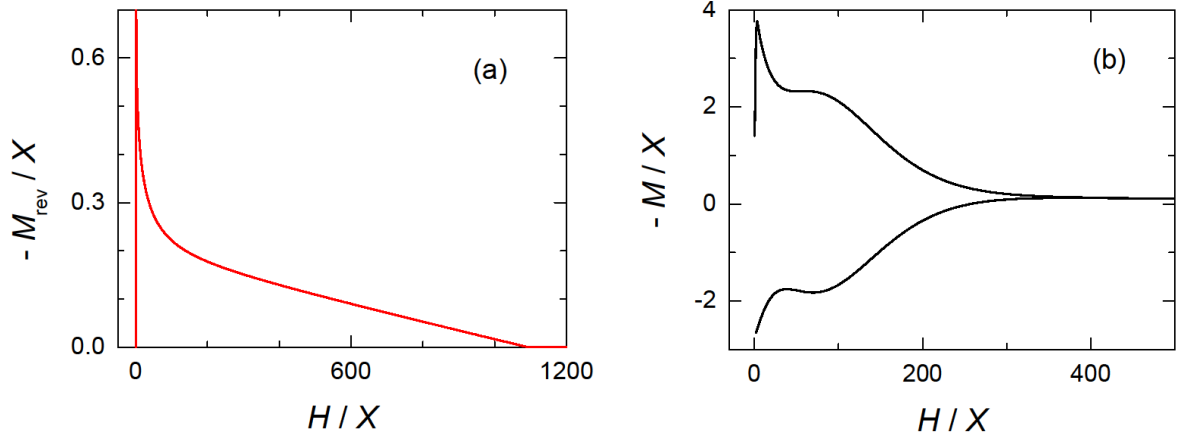


**Fig. 2.7.1.** Reversible (a) and irreversible (b) field dependence of the magnetization calculated using the magnetization scaling with  $X$  as the fitting parameter.

Heuristic models for  $J_c(B)$  (or  $F_{\text{pin}}(B)$ ) should take into account the fishtail effect. Many of such models were compared and critically discussed by Jirsa *et al.* [110,111,112]. These models can be divided into two categories, according to the pinning potential used, namely models with the power-law and the logarithmic potential.

Classical pinning theory, as introduced by Kramer [113], explains the peak in the  $F_{\text{pin}}(B)$  dependence by a crossover from the regime of individual vortex pinning at low fields to the regime of elastically interacting vortex lattice at high fields. The relative position of PE maximum is controlled by two parameters and the same applies for the curve width. So far, the analysis of a fully developed PE in the RE123 system requires rather high values of the fitting parameters that lack a theoretical explanation [111].

More recently Yin *et al.* proposed new approach, where pinning potential was represented by a power expansion [114]. The  $F_{\text{pin}}(B)$  dependence consists of one term increasing with a power of  $B$  and three terms decreasing at different rates with increasing  $B$ . Such a function develops a maximum at an intermediate field  $B_{\text{peak}}$  [114,115,116,117]. Yin's approach results in a scaling relation that is very similar to the classical Kramer's law.

The critical current density with the logarithmic pinning potential decays at high fields exponentially with increasing field according to following relation:

$$J_c \left( \frac{B}{B_{\text{peak}}} \right) = \left( \frac{B}{B_{\text{peak}}} \right)^m \exp \left\{ \left[ 1 - \left( \frac{B}{B_{\text{peak}}} \right)^n \right] \frac{m}{n} \right\}, \quad (2.7.1)$$

where  $m$  equals one for most of the RE123 single crystals. In such case  $n$  remains the only free parameter. A similar expression can be derived for the pinning force density by replacing  $m$  by  $m + 1$ . The fact that only the peak position  $B_{\text{peak}}$  is needed for determining  $n$  and consequently the shape of the whole curve up to the irreversibility field is a big advantage of this model [111].

Comparable accuracy of the fits of the experimentally obtained values of  $M(H)$  with various pinning potentials were reported [111]. Nevertheless, the fit of experimental data for HTSC with the classical formula is more difficult due to larger ‘‘freedom’’ of the fitting parameters [111]. The logarithmic pinning potential is justified in HTSC by both magnetic and transport experiments as it leads to an exponential decay of  $F_{\text{pin}}(B)$  and  $J_c(B)$  at high fields.

The above heuristic models for the fishtail effect at intermediate field do not account for the experimentally established background vortex pinning that is generally evident at low fields. The force of background pinning decays approximately exponentially with field (as does  $J_c(B)$  in samples without peak effect [110,111]), hence, it is reasonable to assume following formula for the critical current density:

$$J_c \propto \exp\left(-\alpha \frac{B}{B_{\text{peak}}}\right). \quad (2.7.2)$$

Here  $\alpha$  is a positive parameter.



### 3. Measurement techniques

Various experimental methods are used to study magnetic properties of superconductors. Among them, Superconducting Quantum Interference Device (SQUID) magnetometer is the system of the highest sensitivity for measuring of a sample's magnetic moment. Exact values of superconducting-to-normal transition temperature and its width are often obtained from AC susceptibility measurements. For determination of anisotropy parameter, torque magnetometry technique is the most accurate. Finally, Hall probe scanning technique is a proper tool to investigate trapped field profiles. All of the techniques are shortly introduced below.

#### 3.1. SQUID magnetometry

The SQUID magnetometer itself is one of the major applications of superconductivity. In 1962 Josephson [118,119] predicted that a zero voltage supercurrent should flow between two superconducting electrodes separated by a thin insulating barrier. Moreover, if a voltage difference were maintained across the junction, the difference in the phase of the GL wavefunction in the two electrodes would evolve so that the current would be an alternating one with amplitude  $I_c$ . If the corresponding supercurrents  $I_{c1} = I_{c2} = I_c$  passed by two Josephson contacts, then the maximum supercurrent of the combination would be:

$$I_{\max} = 2I_c \left| \cos(\pi\Phi / \Phi_0) \right|, \quad (3.1.1)$$

where  $\Phi$  is the magnetic flux, i.e.  $\Phi = \int \vec{A} d\vec{s}$ . Hence, SQUIDs are based on the principle of quantum interference and Eq. (3.1.1) is the basic equation governing the SQUID magnetometer. The effective critical current is modulated by the flux enclosed in the junction, which permits  $\Phi$  to be measured to an extremely small fraction of  $\Phi_0$ . Therefore, the greatest advantage of this measurement system is high resolution. The SQUID magnetometer operates with a radio frequency sensor able to detect magnetic moments even of the order of  $10^{-10} \text{ Am}^2$ . As long as the current is smaller than the intrinsic critical current,  $I_{c0}$ , voltage is equal zero. If the current is greater than  $I_{c0}$ , the DC voltage across the device is

$$V = \frac{R}{2} \left[ I^2 - [2I_c \cos(\pi\Phi / \Phi_0)]^2 \right]^{1/2}, \quad (3.1.2)$$

where  $R/2$  is the resistance of the two resistively shunted junctions in parallel. Hence, SQUID can be viewed as a flux-to-voltage transducer. The largest vortex swing is obtained if the device is biased at current of amplitude  $2I_c$ , in which case voltage ranges from zero for integral numbers of flux quanta to  $I_c R$  for half-integral flux values.

The principle of measurements with SQUID magnetometer is the following. Flux (or current) is coupled with the SQUID ring by a superconducting input coil. The input coil,  $L_i$ , is a part of a flux transformer, which consists of an external superconducting coil,  $L_c$ . The flux changes in  $L_c$  are directly mirrored in  $L_i$ , hence, detected by the SQUID. The flux in the superconducting ring is decoupled from the external field as long as the necessary shielding current is smaller than the critical current of the ring itself. Connecting a superconducting pick-up coil to the input coil of the SQUID allows to transform the flux created by a sample in this pick-up coil into the sensor. Moving the sample in and out of the pick-up coil leads to a signal in the SQUID output coil. Such signal is directly proportional to the sample's magnetic moment. In order to reduce any environmental noise, the pick-up coil is usually produced as a second order gradiometer and consists of three coils. In that case, magnetic signals which are seen simultaneously by both of these coils cancel and the first derivative of the environmental noise is rejected. A single loop of the pickup coils is characterized by a radius  $R$  and loops are separated by distance  $d$ . The output voltage,  $V_{\text{SQUID}}$ , is evaluated by fitting the proportionality of the obtained voltage-versus-position to a calibration curve with the theoretical expression for a pure magnetic dipole signal [120]:

$$V_{\text{SQUID}}(z) = C \left( \frac{2}{(z^2 + R^2)^{3/2}} - \frac{1}{((z+d)^2 + R^2)^{3/2}} - \frac{1}{((z-d)^2 + R^2)^{3/2}} \right), \quad (3.1.3)$$

where  $z$  denotes the sample position. At the end, the magnetic moment is calculated, see Fig. 3.1.1.

The sample is magnetized by a constant magnetic field and the magnetic moment of the sample is measured, producing a DC magnetization curve. The sample is moved commonly over a distance of few centimetres, in order to compensate for the field inhomogeneity and to obtain the output voltage with the full dipole signal as the function of the sample position. With this configuration, the magnetometer is sensitive not to the magnetic flux itself, but rather to its second (spatial) derivative. Only the longitudinal magnetization is probed.

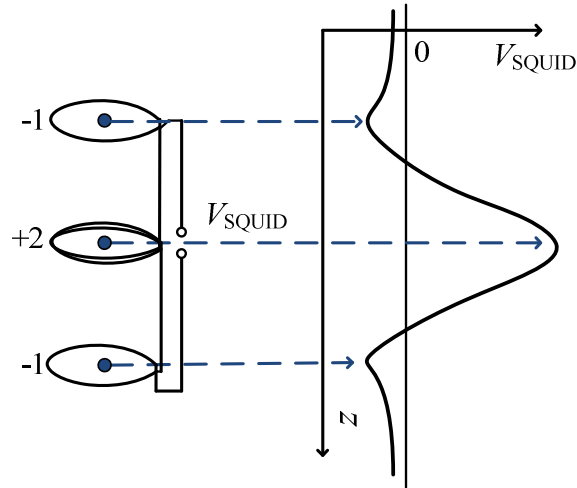


**Fig. 3.1.1.** Schematic view of the dependence of the output voltage of a second order gradiometer on the sample position. Left: gradiometer coil arrangement, right: output voltage as a function of the sample position.

### 3.2. AC susceptibility

AC magnetic measurements, in which an AC field is applied to a sample and the resulting AC moment is measured, are commonly used to study magnetic properties of wide range of materials [121]. Because the moment induced in sample is time-dependent, AC measurements yield information about magnetization dynamics which cannot be obtained in DC measurements. In AC magnetic measurements, the field of the time-dependent moment in the sample induces a current in the pickup coils, allowing for measurement without sample motion.

In case of low frequencies, the magnetic moment of the sample follows the  $m(H)$  curve that would be measured in a DC experiment. As long as the AC field is small, the time-dependent induced AC moment is:

$$m_{\text{AC}}(t) = \chi H_{\text{AC}} \sin(\omega t). \quad (3.2.1)$$

Here  $H_{\text{AC}}$  is the amplitude of the driving field,  $\omega$  is the driving frequency, and  $\chi = dm/dH$  is the slope of the  $m(H)$  curve, called the susceptibility. The AC measurement is very sensitive to small changes in  $m(H)$  and not to the absolute value. Hence small magnetic shifts can be detected even when the absolute moment is large. At higher frequencies, the AC moment of the sample does not follow along the DC magnetization curve due to dynamic effects in the sample. For this reason, the AC susceptibility is often known as the dynamic susceptibility. In this higher frequency case, the magnetization of the sample may lag behind the drive field, an

effect that is detected by the magnetometer circuitry. Thus, the AC magnetic susceptibility measurement yields two quantities: the magnitude of the susceptibility,  $\chi$ , and the phase shift,  $\phi$  (relative to the drive signal). Alternately, one can think of the susceptibility as having an in-phase (real) component  $\chi'$  and an out-of-phase (imaginary) component  $\chi''$ . The two representations are related by

$$\chi' = \chi \cos \phi, \quad (3.2.2)$$

$$\chi'' = \chi \sin \phi, \quad (3.2.3)$$

$$\chi = \sqrt{\chi'^2 + \chi''^2}, \quad (3.2.4)$$

$$\phi = \arctan(\chi''/\chi'). \quad (3.2.5)$$

In the limit of low frequency, where results of an AC measurement are most similar to those of a DC measurement, the real component  $\chi'$  is just the slope of the  $m(H)$  curve. The imaginary component,  $\chi''$ , indicates dissipative processes in the sample and is equal to zero for superconductors in magnetic field  $H < H_{c1}$ .

### 3.3. Torque magnetometry

Measurements of the anisotropy of a HTSC in a wide temperature range are experimentally challenging e.g. due to a large anisotropy. The most accurate method to measure the anisotropy parameter is torque magnetometry, see e.g. [122,123].

If the magnetic field is applied along a principal axis, the sample magnetic moment  $\vec{m}$  will align parallel to the external induction, just like in isotropic materials. However, if the magnetic field is not applied along a principal axis, the magnetic moment will not align parallel to the external induction and will experience a mechanical torque  $\vec{\tau}$  given by the following equations:

$$\vec{\tau} = \mu_0(\vec{m} \times \vec{H}), \quad (3.3.1)$$

$$\tau(\theta) = \mu_0 m_{\perp}(\theta) H, \quad (3.3.2)$$

where  $m_{\perp}$  denotes the magnetization component perpendicular to the applied field.

Torque magnetometers are sensitive only to the part of the magnetization transverse to the applied field. Measurements as a function of the direction of the applied field are the prime mode of most torque magnetometers. The sensitivity of torque magnetometer is



proportional to the strength of the external field and torque sensors give very accurate results in very high fields.

Torque magnetometry uses piezoresistive paths in chips' legs of a cantilever and the principle of torque measurements applied for uniaxial superconductors are the following. A superconducting sample is placed on the platform connected with the chip by two legs, see Fig. 3.3.1, with the  $ab$ -plane of the sample is fixed flat to the platform. The sample is cooled down below  $T_c$  and the magnetic field is applied along the crystallographic  $c$ -axis of the superconductor. In this geometry, magnetic moment induced in the sample is aligned almost perpendicular to the planes due to the screening currents that flow within the layers. Due to symmetry reasons and as the magnetic moment tries to minimize the induction within the superconductor, the moment direction is in the plane spanned by the applied field and the  $c$ -axis of the sample. Hence, the mechanical torque is perpendicular to this plane, see Fig. 3.3.2. Torque cantilever with the superconducting sample can be rotated over 360 deg in respect to the field direction. Bending of the cantilever changes the total resistance of the two piezoresistive paths, while a torsion of the cantilever results in a change of the difference of the resistance of the piezoresistive paths. In either mode, the resistance change is measured with a conventional Wheatstone bridge and a lock-in amplifier. Typical cantilever of a commercial torque magnetometer designed by Quantum Design enables measurements of crystals with size of up to  $1.5 \times 1.5 \times 0.5$  mm and weight of up to 10 mg.

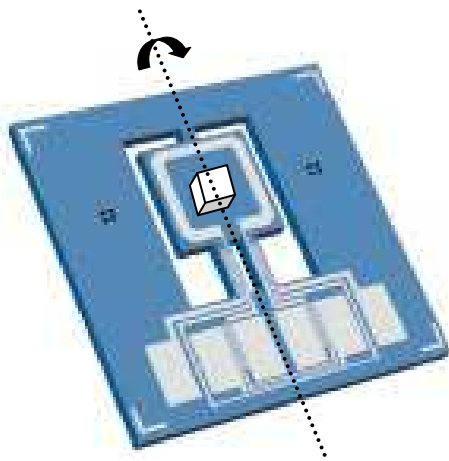


**Fig. 3.3.1.** A torque cantilever in torque magnetometer with the  $ab$ -plane of a superconducting sample fixed on the platform. The arrow shows direction of the cantilever's rotation.

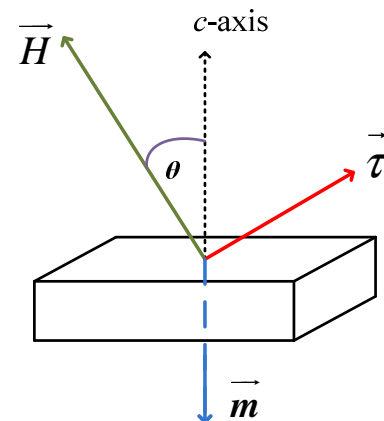


**Fig. 3.3.2.** Definition of the magnetic torque.

### 3.4. Hall probe scanning technique

Hall scans represent an appropriate pre-characterisation of superconductors, because the critical current, almost equivalently to transport measurements, can be probed in this way. In addition, this method is non-destructive and there is no need for a special preparation. The maximum trapped field in the centre of the sample depends primarily on the sheet's current density. Weaker pinning (related to a reduced trapped field) can easily be distinguished. Therefore, the scans provide qualitative information on the local variation of the critical current density in those samples. Additionally, for sufficiently thin samples (not the case of the investigated crystals), quantitative information about the critical current can be obtained from the inversed field profiles.

Hall scan leading to a proper determination of superconducting parameters can only be carried out on samples that can be magnetized to saturation in a homogenous external magnetic field. The scan setup, presented on Fig. 3.4.1, consists of a scan table with a stepper motor, the sample holder placed in a cooling liquid bath, a micro-voltmeter, a current source, a computer and different scanning devices. The scanning device is attached to the scan table and can be moved in all directions. After removing the magnetic field the remanent magnetization is scanned by a Hall probe. The Hall probe measures a voltage which is proportional to the local field of the bulk superconductor.

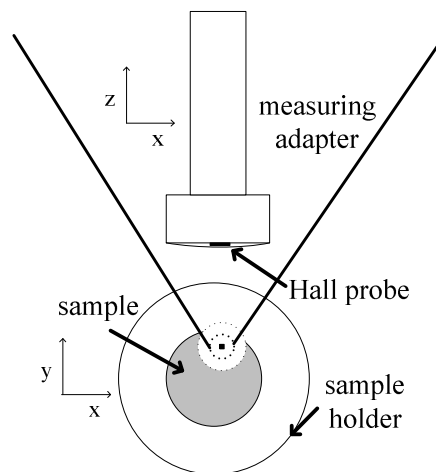


**Fig. 3.4.1.** Sketch of the experimental setup for Hall probe scanning technique.

The spatial resolution of the measurement setup strongly depends on the distance between the Hall probe and the sample surface. Therefore, the scanning device has to be

placed as close to the sample surface as possible. The distance between the active area of the Hall probe and the sample surface is generally between 0.1 and 0.5 mm. Furthermore, the sample surface must be flat and fixed to obtain no changes in the distance. Generally, a distance of 0.2 mm and a step width of 0.5 mm are used.

To sum up, both SQUID magnetometer with DC mode and torque magnetometry measure the DC magnetization, as opposed to AC susceptibility magnetometry, which measures the magnetic response to alternating external fields. Both SQUID and torque magnetometry measure the total or “bulk” magnetic moment of a sample, in contrast to, e.g., microscopic Hall sensor [124] or magneto-optics [125], which probe the local magnetization. Torque magnetometers are sensitive only to the part of the magnetization transverse to the applied field, whereas the most commonly used SQUID magnetometers are sensitive only to the longitudinal magnetization. Measurements with  $H // c$ -axis or  $H // ab$ -plane are not possible with torque magnetometry, since in these cases the magnetic moment and the field are directed (anti)parallel, and the torque is thus equal to zero. To conclude, in the current work, it was necessary to employ multiple measurement techniques in order to obtain full set of parameters required to study superconducting state properties of the investigated crystals.



## 4. Single crystals of $\text{REBa}_2\text{Cu}_3\text{O}_{7-\delta}$ and their characterization

The phase diagram of the high- $T_c$  superconducting cuprates results from tuning of the doping in the  $\text{CuO}_2$  planes (e.g. via oxygen content variation) and is shown schematically in Fig. 4.1. The superconducting cuprates are antiferromagnetic Mott insulators at half filling, i.e. their spins in the  $\text{CuO}_2$  planes arrange antiferromagnetically due to interactions between the electrons [126,127]. Thus cuprates join other families of superconductors, such as heavy fermion and organic materials, which have AFM near, or coincident with, superconductivity. With addition of holes to the  $\text{CuO}_2$  planes the AFM transition is rapidly suppressed and a superconducting state emerges. At the same time, electron correlations in a superconductor can be tuned from weak to strong. The superconducting  $T_c$  rises with increasing hole doping through the underdoped regime, reaches a peak at the optimal oxygenation level, and then falls away again at higher doping, i.e. at the overdoped regime, see e.g. [128,129]. There are also HTSC that can be electron-doped, however, they are out of the scope of this thesis.

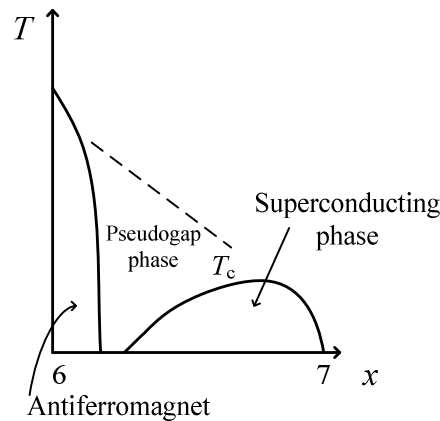


**Fig. 4.1.** Generalized phase diagram for RE123, where  $x$  denotes the oxygen content  $7-\delta$ .

Materials characterized as  $\text{REBa}_2\text{Cu}_3\text{O}_{7-\delta}$  are anisotropic superconductors and measurements have to be performed on single crystals in order to determine their intrinsic properties. Optimally doped crystals of RE123 have the transition temperature of above 90 K and a perovskite structure, analogously to the structure of Y123 presented on Fig. 4.2, with Y ions substituted by different rare earth ions. The lattice parameters do not change significantly upon such substitution, nevertheless they reflect changes in the radius of each ion.

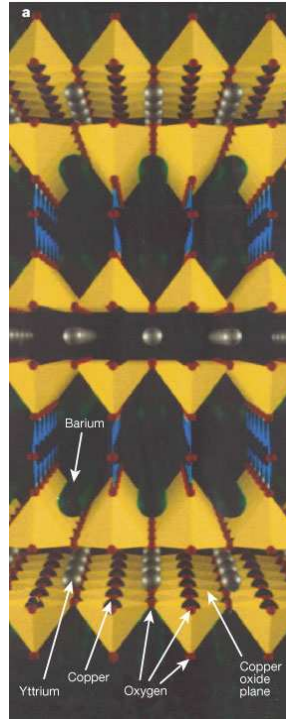


**Fig. 4.2.** The crystal structure of Y123, after Ref. [130].

#### 4.1. Crystal growth and annealing

The preparation of RE123 crystals is difficult due to their thermal and chemical instability and intensive interaction of the crystal with a solvent or crucible materials [131,132]. Additional problems come from the shortage of data concerning a phase equilibrium in this system and the role of oxygen gas in the process [133]. Usually, the growth of RE123 single crystals is performed by a crystallization method from solution during slow cooling. Crystals grow along the *c*-axis in the form of thin platter [131] and the thickness of crystals depends on the cooling rate [134].

Methods most widely used to obtain thick and large single crystals of RE123 are TSSG (Top Seeded Solution Growth) or TSFZ (Travelling Solvent Floating Zone) methods. Crystals can be grown in the air or reduced atmosphere, at normal or reduced gas pressure. Changing oxygen partial pressure may affect liquid properties (viscosity, diffusivity, solubility) which then affects growth conditions, and, finally, superconducting properties of the growing crystal. When low oxygen pressure, i.e. below 1 bar, is applied, crystals can be grown at lower temperature than those grown in the air [135]. On the other hand, higher oxygen partial pressure, i.e. of 1 bar, plays a significant role in increasing the growth rates [136].

Crystals' growth using TSSG method [137] is performed in a vertical furnace. The seed is a Y123 thin film prepared by a thermal evaporation on MgO single crystal. Usually  $\text{RE}_2\text{O}_3$  is used as the crucible while a molten solvent is made from  $\text{Ba}_x\text{Cu}_y\text{O}$  powders. For growing of Y123 single crystals,  $\text{Y}_2\text{O}_3$  is used as the crucible,  $3\text{BaO}\cdot 5\text{CuO}$  can be used as a solvent with  $\text{Y}_2\text{BaCuO}_5$  as a solute [138]. First the solution is heated above the temperature of crystallization of a RE123 crystal. The seed crystal touches the solution from the top. When temperature is slowly reduced, i.e. with the speed of about 0.2 K/h, the solvent and the solute react to form the Y123 phase at the seed. Crystallization of single crystal on the seed begins. During crystallization, the seed is rotated at the speed of about 50 rpm and lifted up with the speed of about 0.08 mm/h [139]. With this method large and good quality single crystals of RE123 can be obtained. Such crystals are interesting from the point of view of both investigating anisotropic properties as well as examination of materials for future applications like superconducting magnets.

Travelling Solvent Floating Zone method is an extension of the Floating Zone method [140] that uses no crucible, thus reducing the impurity level induced in the growing crystal. In the TSFZ method a polycrystal sample on top (so-called rod) touches the monocrystal seed at the bottom. A radiation lamp produces very high temperature melting the rod. The seed is rotated opposite to the direction of rotation of the rod. The molten (floating) zone is translated along the sample length by moving the material with respect to the radiation focus. The crystal is grown on the solidifying end of the float zone. The crystal growth can be performed at one point on the temperature-composition phase diagram thus providing an opportunity for growth of large single crystals even if their crystallization field is very narrow. Using TSFZ method the successful growth of materials which do not melt congruently can be achieved. Though the method has a lot of advantages, crystals must be grown at temperatures near 1000 °C. Therefore, TSFZ cannot be applied to the growth of a HTSC which contain volatile elements.

The as-grown crystals are tetragonal and non-superconducting. Transition from normal (tetragonal) to superconducting (orthorhombic structure) phase occurs during annealing. At that time the oxygen content is tuned from about 6 up to 7. Sometimes, several hundred hours are needed for the oxygenation of RE123 crystals using the flowing oxygen annealing (FOA), because of high density of such crystals, see e.g. [141]. In order to raise the efficiency of the oxygen annealing, the high pressure oxygen annealing (HPOA) method can be introduced.

The maximum oxygen pressure applied in the furnace chamber can reach several MPa. The annealing time, for annealing temperatures of around 450–500 °C, can be shortened from over 200 h for FOA to only 40–70 h for HPOA [142].

Twinning appears as the result of the phase transition from tetragonal to orthorhombic structure, in which elastic strains lead to formation of a domain structure. Twin planes form easily during the annealing process of RE123 due to the fact that the unit cell is only slightly orthorhombic. The twins form when oxygen ordering in the basal copper-oxide plane leads to the elongation of the *b*-axis and the contraction of the *a*-axis of the crystal lattice [141]. Thus, twins represent regions of high stress. Therefore, boundaries between different twin domains may act as pinning centres correlated along the *c*-axis direction. Twin-free crystals may be obtained by applying the pressure of about 10 MPa along the crystallographic *a(b)*-axis, while the samples are held at temperatures around 120 °C [143]. Also for crystals cooled down in pure nitrogen atmosphere after the annealing process twin structure has not been observed [136].

Different cooling procedures and speed for the cooling of crystals after their annealing lead to different oxygen content in the studied crystals [144,145]. This allows to investigate the doping effect on the superconducting state parameters.

## 4.2. Critical temperature and oxygen content

The critical temperature is related to the oxygen deficiency,  $\delta$ , through the generic phase diagram of cuprate superconductors [146,147,148], see Fig. 4.1. It was found that  $T_c$  follows an approximately parabolic dependence upon the doped hole concentration  $p$  [149]. Specifically,  $p$  is the fraction of holes per Cu atom in the CuO<sub>2</sub> sheet. This phase diagram is seen most clearly in the oxygen stoichiometric La<sub>2-x</sub>Sr<sub>x</sub>CuO<sub>4</sub>, where one-to-one correspondence between  $x$  and  $p$  was reported [150]. In such case  $T_c$  appears to be maximized around  $p \approx 0.16$ , falls to zero on both underdoped and overdoped sides at  $p \approx 0.05$  and  $p \approx 0.27$ , respectively, and can be represented using the following relation [150]:

$$\frac{T_c}{T_{c, \max}} = 1 - 82.6(p - 0.16)^2. \quad (4.2.1)$$



In fact, a single universal phase curve  $T_c(p)$  was found for several HTSC to scale with  $T_{c, \max}$  [150]. Moreover, HTSC exhibit an approximate scaling of the superfluid density,  $\sigma_s$ , with  $T_c$  [151] consistent with strong correlation models [152,153].

The oxygen content is related to the lattice parameters and particularly for Y123 superconductors crystallographic axis lattice constants were found to be described by the following relations [154]:

$$\begin{aligned} a &= 0.387498 - 0.09655x + 0.03908x^2, \\ b &= 0.389605 - 0.015166x + 0.0323x^2 - 0.018324x^3, \\ c &= 1.18114 - 0.01298x, \end{aligned} \quad (4.2.2)$$

where  $x$  is related to the oxygen content through  $x = 1-\delta$  and  $a$ ,  $b$ , and  $c$  are the lattice constants in nm.

Critical temperature of RE123 superconductors depends on the ionic radius of the rare earth ion substituting Y. Maximum  $T_c$  for optimally doped RE123 samples decreases with the decreasing radius of the rare earth ion [155]. However, it was observed that introduction of Pr, Ce, and Tb ions destroys superconductivity for high substitution levels. On the other hand, substitution of Nd or Sm in the place of Y in Y123 does not lead to significant changes in  $T_c$  and maximum  $T_c$ 's of up to 96 K were reported [155].

### 4.3. Solubility of a rare earth for Ba ions in REBa<sub>2</sub>Cu<sub>3</sub>O<sub>7-δ</sub>

In YBa<sub>2</sub>Cu<sub>3</sub>O<sub>7-δ</sub> with a light rare earth (LRE) substituted at the Y position, LREBa<sub>2</sub>Cu<sub>3</sub>O<sub>7-δ</sub> (LRE = Nd, Sm, Pr), ionic radius of LRE (for the coordination number 6), i.e. of Pr<sup>3+</sup> (0.099 nm), Nd<sup>3+</sup> (0.098 nm), and Sm<sup>3+</sup> (0.096 nm), are significantly smaller than ionic radius of Ba<sup>2+</sup> (0.135 nm) [156]. Nevertheless, it was shown experimentally that it is difficult to completely eliminate LRE-Ba substitutions [157]. The LRE-Ba substitutions cause reduction in  $T_c$  and broadening of the superconducting-to-normal state transition [136]. Additionally such substitutions highly influence the critical current values, see Ref. [136] and references therein. It was found that the substitution of LRE ion into Ba position in LREBa<sub>2</sub>Cu<sub>3</sub>O<sub>7-δ</sub> crystals is mostly affected by the oxygen partial pressure during the crystal growth. Suppression of the LRE-Ba substitutions can be achieved by performing the growth at a reduced oxygen atmosphere [158]. Furthermore, various Ba-rich additions such as BaO<sub>2</sub>, Sm<sub>2</sub>BaO<sub>7-δ</sub>, Nd<sub>2</sub>BaO<sub>7-δ</sub>, or GdBa<sub>6</sub>Cu<sub>3</sub>O<sub>7-δ</sub> can also be used to suppress the LRE-Ba substitutions and increase  $T_c$  [159,160,161,162,163].



## 5. Superconducting state parameters and their evaluation

Most of the superconducting state parameters of investigated sample can be determined from magnetization measurements. However one should always consider the presence of background contribution to the superconducting signal in  $M(H)$  measurements. Such background contribution is usually field and temperature dependent and has to be evaluated for each crystal and the crystal's orientation in respect to the applied field. Therefore, measurements of the magnetic moment,  $m(H)$ , should be performed in a broad range of temperatures above  $T_c$ . The background contribution should be subtracted from each magnetization curve,  $M(H)$ , prior to the evaluation of the superconducting state parameters.

If the long sample approximation is not met, demagnetizing field modifies the magnetic induction. This effect is described by the demagnetizing factor,  $D$ . The induction is now  $B = \mu_0(H + (1 - D)M)$  and the flux starts penetrating the sample at  $H_{c1}^* = (1 - D)H_{c1}$ . The demagnetizing factor can be easily determined from  $M(H)$  dependence if sample remains in the Meissner state and is fully diamagnetic. Then, a deviation of the constant slope of  $dM/dH$  from -1 value determines the  $D$  parameter. The demagnetizing factor should always be taken into account while working with the magnetization data, although it modifies  $M(H)$  dependence only at small fields of the order of  $H_{c1}$ .

### 5.1. Intrinsic parameters

The transition or critical temperature,  $T_c$ , is the temperature below which the investigated sample becomes superconducting. Value of  $T_c$  may be determined from zero field cooled (ZFC) measurement in the DC mode performed using SQUID magnetometer. In this procedure the sample is first cooled down from above  $T_c$  to a temperature significantly below  $T_c$  in zero field. Afterwards, a small magnetic field is applied and measurement is performed with warming. The value of  $T_c$  may be determined from the onset of superconductivity. However, more often the  $T_c$  is obtained from the steepest slope of  $M(T)$  in the transition region and its linear extrapolation to the zero magnetization, i.e. the normal conducting value, see Fig. 5.1.1a. The value of  $T_c$  may, as well, be determined similarly from the real part of the susceptibility in the AC measurements, see Fig. 5.1.1b. The transition width,  $\Delta T_c$ , is usually defined with the 10-90 % Meissner state criterion.

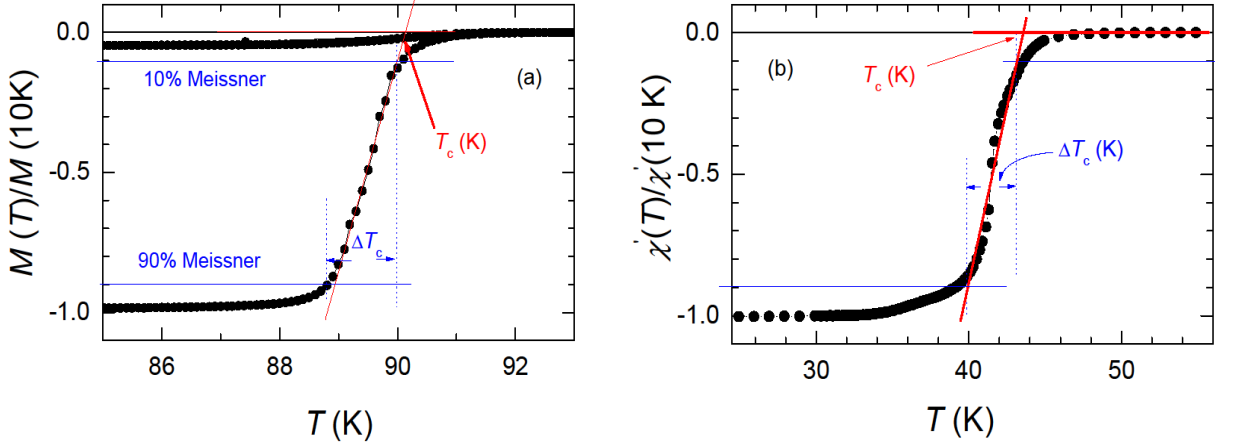


**Fig. 5.1.1.** (a) Temperature dependence of the magnetization. Value of  $T_c$  is evaluated from the magnetization measurement performed in the DC mode. (b) Temperature dependence of the reduced real part of the susceptibility. Value of  $T_c$  is evaluated from the susceptibility measurement performed in the AC mode.

Values of the lower critical field are difficult to obtain from magnetization measurements directly, since the first deviation from a true Meissner state is often masked by barriers for flux penetration, see Section 2.6. More accurate values of  $H_{c1}$  may be determined by applying magnetization scaling, see Section 2.7, according to the treatment of Labusch-Doyle. This method, i.e. the effective media approach, takes into account the geometric and surface barriers, thus leading to the exact value of  $M(H)$  at low and high fields. In this method  $H_{c1}$  is set for  $X$  and together with  $\kappa$  are the only scaling parameters. The superconducting state parameters along the  $c$ -axis may be determined. After determination of  $H_{c1}(T)$  by the fitting procedure, other superconducting state parameters can be evaluated. First, the simplified equation is employed to relate  $H_{c1}(T)$  with  $H_c(T)$  values:

$$\mu_0 H_{c1}^{\parallel c} = \frac{\mu_0 H_c}{\sqrt{2} \kappa^{\parallel c}} \ln \kappa^{\parallel c}. \quad (5.1.1)$$

It was found that the zero-temperature thermodynamic critical field is well approximated by following relation, which is applicable for cuprates as well, [164]:

$$\frac{H_c(T)}{H_c(0)} = 1.7367 \left[ 1 - \frac{T}{T_c} \right] \left[ 1 - 0.2730 \left( 1 - \frac{T}{T_c} \right) - 0.0949 \left( 1 - \frac{T}{T_c} \right)^2 \right]. \quad (5.1.2)$$

In the high- $T_c$  superconducting cuprates the upper critical fields are relatively high and only  $H_{c2}(T)$  at temperatures close to  $T_c$  are experimentally available. The value of the upper critical field along the  $c$ -axis can be determined from Eq. (2.3.5) using  $\kappa$  and previously derived  $H_c(T)$

values. Then, the zero-temperature  $H_{c2}(0)$  can be estimated using the Werthamer-Helfand-Hohenberg (WHH) approximation [165]. The WHH can be expressed (assuming the clean limit) [7] by the following relation:

$$H_{c2}(0) = 0.7255T_c \frac{dH_{c2}}{dT}. \quad (5.1.3)$$

Values of the upper critical field can, alternatively, be obtained according to the logarithmic relation between the reversible part of the magnetization and magnetic field (as in Eq. (2.1.4)). Then a linear fit of  $M$  vs.  $\ln H$  is extrapolated to the zero-magnetization value at the field corresponding to  $H_{c2}$ . Moreover, the reversible magnetization slope vs.  $\ln H$  leads, due to Eq. (2.1.4), to the superfluid density via  $\lambda_{ab}(T)^{-2} \propto \rho_s$ .

The anisotropy parameter,  $\gamma$ , can be derived from magnetization measurements as a ratio between two slopes in  $dM_{\text{rev}}/dH$  for  $H \parallel c$ -axis and for  $H \parallel ab$ -plane, respectively, see Eqs (2.1.4) and (2.1.5) with  $\lambda_a = \lambda_b = \lambda_{ab}$ . However, it is difficult to obtain  $\gamma$  from such data when a substantial paramagnetic background contribution to the superconducting signal is present. Additional problem, in case of cuprates with a large anisotropy, may be obtaining the perfect alignment of the crystal's  $ab$ -plane in respect to the field direction, which is critical in deriving the exact  $\gamma$  value. A more accurate method to obtain the anisotropy parameter is to apply the torque magnetometry. The magnetic torque is normally recorded at increasing and decreasing angles  $\theta$  between the  $c$ -axis and the applied magnetic field in an angular range of  $180^\circ$  (Fig. 5.1.2). The angular dependence of the superconducting torque in the reversible region is given by the Eq. (2.1.11). However, thermal fluctuations of vortices are not considered directly in Eq. (2.1.11). As already shown, Schneider's functional [166] for a fluctuating torque is estimated to be sinusoidal close to  $T_c$ . Hence, fluctuations can be taken into account by adding  $A \sin(2\theta)$  term to the right-hand side of Eq. (2.1.11), thus leading to following equation:

$$\tau = -\frac{VH\Phi_0}{16\pi\lambda_{ab}^2} \left(1 - \frac{1}{\gamma^2}\right) \frac{\sin 2\theta}{\varepsilon_\theta} \ln \left( \frac{\eta H_{c2}^{\parallel c}}{\varepsilon_\theta H} \right) + A \sin(2\theta). \quad (5.1.4)$$

The additional term, where  $A$  is the background amplitude, describes paramagnetic or diamagnetic background contribution to the superconducting torque [167,168]. An example of torque measurement with the fit of Eq. (5.1.4) to the reversible torque is presented in Fig. 5.1.2. The reversible torque is calculated from  $\tau_{\text{rev}}(\theta) = (\tau(\theta^+) + \tau(\theta^-))/2$  that is obtained by clockwise,  $\tau(\theta^+)$ , and counterclockwise,  $\tau(\theta^-)$ , rotating the sample in the magnetic field.

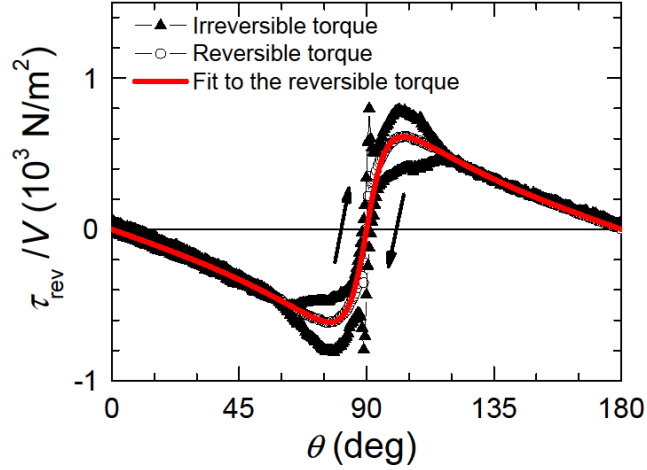


**Fig. 5.1.2.** Example of angular dependence of the torque. Triangles denote the irreversible (clockwise and counterclockwise) and circles denote the reversible (averaged) torque.

By measuring the angular dependence of the torque in the mixed state of a superconductor with a paramagnetic or diamagnetic background, four parameters can be extracted from the data: the in-plane magnetic penetration depth, the  $c$ -axis upper critical field, the effective mass anisotropy, and the background torque amplitude.

The assumption of continuous vortex lines made in the 3D anisotropic model, i.e. in Eq. (5.1.4) should be validated when studying highly anisotropic HTSC. To fully justify the applicability of the AGLT approximation,  $\xi_c(T)$  has to be larger than the interplanar distance  $s$ , which is of the order of 0.8 nm for RE123 [91]. Otherwise, the magnetic torque for fields almost parallel to the  $ab$ -plane should be better described within the 2D Lawrence\_Doniach approach.

## 5.2. Extrinsic parameters

The irreversibility field,  $H_{\text{irr}}(T)$ , is often presented in logarithmic plot of a power law dependence

$$H_{\text{irr}} = \beta \left( 1 - \frac{T}{T_c} \right)^\alpha, \quad (5.2.1)$$

where  $\alpha$  parameter depends on the dimensionality of the system and is around 1.5 for continuous vortex lines, while  $\beta$  is the proportionality parameter. At lower temperature, due to a decrease of the coherence length  $\xi_c$ , behaviour of the system of vortex lines may become more similar to behaviour of a two-dimensional system of vortex “pancakes” [7]. If  $\xi_c < s$ ,

a temperature driven 2D to 3D crossover occurs at a temperature defined by  $\xi_c(T_{cr}) \approx s$ . The crossover temperature,  $T_{cr}$ , can be estimated by applying following relation, see e.g. [169],:

$$T_{cr} \approx T_c \left[ 1 - \frac{2\xi_{ab}^2}{(\gamma d)^2} \right]. \quad (5.2.2)$$

Change from  $\alpha$  around 1.5 to a more rapid temperature dependence at higher fields occurs at magnetic field equal to the crossover field,  $H_{cr}$ , where

$$\mu_0 H_{cr} = \frac{\Phi_0}{s^2 \gamma^2}. \quad (5.2.3)$$

Similarly to behaviour at  $T > T_{cr}$ , in the fields lower than  $H_{cr}$ , pancakes couple into vortices and form a three-dimensional system.

The critical current density,  $J_c(B)$ , may be determined from magnetization measurements via Eq. (2.6.1). Then, using following relation:

$$F_{pin}(B) = J_c B, \quad (5.2.4)$$

the pinning force density may be derived. Kramer plots of  $F_{pin}/F_{pin,max}$  versus  $b$  ( $b = B/B_k$ , where  $B_k$  is defined from Kramer plots and is related to the irreversibility field rather than to the upper critical field), see Figs 5.2.1 and 5.2.2, can provide valuable information about pinning mechanisms [35]. Position of the pinning force density peak and its width indicate type of pinning centres. Changes in the position or its width indicate changes of the pinning mechanism for various investigated temperatures/studied crystals.

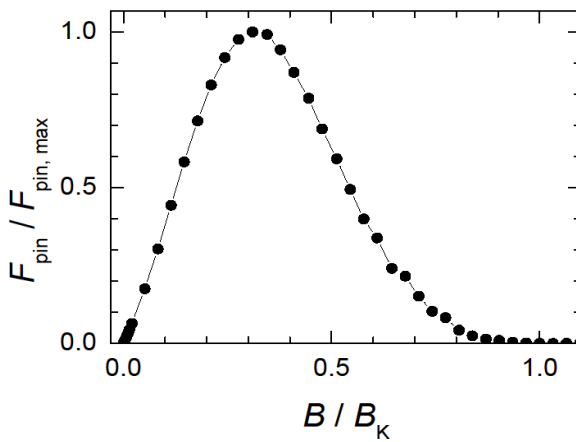


Fig. 5.2.1. Normalized pinning force density.

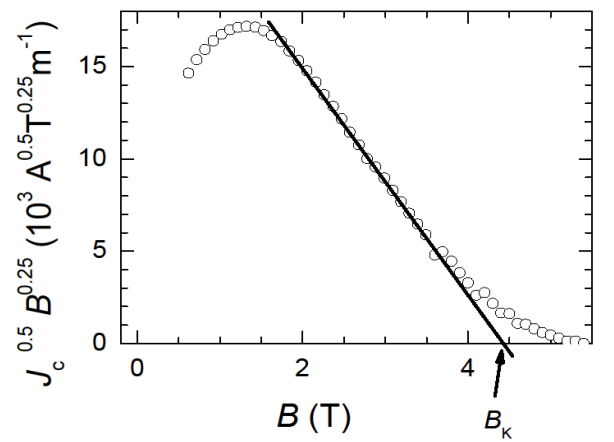


Fig. 5.2.2. Evaluation of the Kramer's field  $B_k$ .





## 6. Oxygen deficiency effect in $\text{SmBa}_2\text{Cu}_3\text{O}_x$ : experimental results and discussion

The origin and nature of different phases observed in the cuprate superconductors are one of the biggest puzzles and, therefore, subject of substantial theoretical efforts. Knowledge of such a phase diagram has a vast technological importance as it includes information about the upper limits for the resistive-free conductance. The dependence of the thermodynamic parameters on the oxygen content was studied in detail for  $\text{YBa}_2\text{Cu}_3\text{O}_{7-\delta}$  only. In recent years, a lot of attention has been paid to  $\text{SmBa}_2\text{Cu}_3\text{O}_x$  partly due to its higher  $T_c$ , but mainly due to its higher critical current density as compared with that of Y123, both in low and high magnetic fields [170]. So far, a complete phase diagram of the Sm-based cuprate has not been investigated. Therefore, comparison of Sm123 with Y123, which could have both a theoretical and functional importance, was the subject of current studies.

One of the most interesting phenomenon discovered under studies of superconducting properties of  $\text{MgB}_2$  and pnictides was the temperature dependence of the anisotropy parameter [16,171,172,173]. A clear evidence whether the anisotropy parameter is temperature dependent or independent was missing for the cuprates [71,169,174], the only remaining group of the whole family of HTSC. This failure, nevertheless, was most likely due to one or few of several factors: (i) pronounced irreversibility, sometimes not fully eliminated by vortex shaking procedure, making the derived anisotropy uncertain, (ii) very narrow temperature range studied, (iii) limitation of the anisotropy data to optimally doped crystals only.

In this Section, the effect of the oxygen deficiency on the superconducting state parameters is discussed and difficulties in description of underdoped cuprates within the AGLT approach are addressed. Underdoped single crystals of  $\text{SmBa}_2\text{Cu}_3\text{O}_x$  were studied using SQUID and torque magnetometry. Focus was drawn to the anisotropy parameter. To make the anisotropy investigations reliable, torque magnetometry measurements (see Section 3.3) were performed in magnetic fields where the torque hysteresis is small or negligible, i.e. at  $H$  of the order of the irreversibility field in the  $ab$ -plane,  $H_{\text{irr}}^{\parallel ab}$ , and in fields below  $H_{c2}^{\parallel c}$ . For highly anisotropic superconductors with irreversibility lines at high magnetic fields, it is often difficult to obtain reliable anisotropy parameters in a wide temperature range. These problems are mitigated in strongly underdoped superconductors where the upper critical field

and the irreversibility field are strongly reduced. An example of such superconductors is  $\text{SmBa}_2\text{Cu}_3\text{O}_x$ .

### 6.1. Single crystals of $\text{SmBa}_2\text{Cu}_3\text{O}_x$

Crystals to be investigated were cut from the as-grown crystal of  $\text{SmBa}_2\text{Cu}_3\text{O}_x$ , of centimetre size and grown by TSSG method in the air. In total five pairs of crystals were prepared, each pair containing one relatively large and one relatively small size crystal (see Tables 6.1.1 and 6.1.2). Each pair was oxygenated simultaneously. Crystals were annealed in flowing oxygen-helium gas at various temperatures between 490 and 505 °C and in oxygen partial pressures between 0.009 and 0.4 bar in order to obtain various oxygenation levels, i.e. crystals with various critical temperatures.

**Table 6.1.1.**  $\text{SmBa}_2\text{Cu}_3\text{O}_x$  crystals' size and conditions of oxygenation.

| Sample                               | Symbol | X, Y, Z (mm) <sup>a</sup> | x, y, z (mm) <sup>b</sup> | Oxygenation parameters |                |              |
|--------------------------------------|--------|---------------------------|---------------------------|------------------------|----------------|--------------|
|                                      |        |                           |                           | Temperature (°C)       | Pressure (bar) | Time (hours) |
| $\text{SmBa}_2\text{Cu}_3\text{O}_x$ | S0     | 2.70, 1.50, 0.96          | 1.00, 0.75, 0.40          | 510                    | 0.005          | 45           |
| $\text{SmBa}_2\text{Cu}_3\text{O}_x$ | S1     | 2.00, 2.60, 0.93          | 0.75, 0.80, 0.40          | 490                    | 0.009          | 100          |
| $\text{SmBa}_2\text{Cu}_3\text{O}_x$ | S2     | 3.09, 3.00, 0.65          | 1.05, 0.90, 0.30          | 505                    | 0.05           | 150          |
| $\text{SmBa}_2\text{Cu}_3\text{O}_x$ | S3     | 3.75, 2.55, 0.90          | 0.87, 0.85, 0.40          | 490                    | 0.1            | 310          |
| $\text{SmBa}_2\text{Cu}_3\text{O}_x$ | S4     | 3.77, 2.59, 0.90          | 0.95, 0.85, 0.45          | 497                    | 0.4            | 620          |

<sup>a</sup> Dimensions of large crystals studied by SQUID magnetometer

<sup>b</sup> Dimensions of small crystals studied by torque magnetometer

The underdoped cuprates have relatively low carrier concentration which results in a small magnetic moment induced when such sample is placed in a magnetic field. Here, to obtain more accurate data, bigger crystals were used in the magnetization measurements performed using SQUID magnetometer. Small crystals were studied applying torque magnetometry. Crystals of  $\text{SmBa}_2\text{Cu}_3\text{O}_x$  were oxygenated according to the oxygenation conditions for Y123 [148,175]. Therefore,  $x$  listed in Table 6.1.2 corresponds to the oxygen

content assumed to be reached during oxygenation and does not correspond to the actual oxygen content in the studied crystals.

The lattice constants' characterization was performed on small crystals using Siemens D-5000 diffractometer with Cu  $K\alpha$  radiation, see Table 6.1.2. The XRD-analysis confirmed high crystallographic quality.

**Table 6.1.2.** Abbreviations for the investigated crystals, their lattice constants, critical temperature, the superconducting-to-normal-state transition width, and the projected oxygen content.

| Symbol | $a, b, c$ (nm) <sup>a</sup> | $T_c$ (K)         | $\Delta T_c$ (K)  | $x^d$ |
|--------|-----------------------------|-------------------|-------------------|-------|
| S0     | 0.38691, 0.39076, 1.17856   | 19.6 <sup>b</sup> | 12.4 <sup>b</sup> | 6.60  |
| S1     | 0.38619, 0.39092, 1.17738   | 42.8 <sup>c</sup> | 4.5 <sup>c</sup>  | 6.70  |
| S2     | 0.38573, 0.39131, 1.17585   | 51.5 <sup>c</sup> | 5.9 <sup>c</sup>  | 6.78  |
| S3     | 0.38533, 0.39131, 1.17491   | 56.5 <sup>c</sup> | 4.1 <sup>c</sup>  | 6.85  |
| S4     | 0.38516, 0.39131, 1.17438   | 63.6 <sup>c</sup> | 7.6 <sup>c</sup>  | 6.90  |

<sup>a</sup> X-ray diffraction measurement performed on small crystals

<sup>b</sup> Data from SQUID measurement using DC mode

<sup>c</sup> Data from SQUID measurement using AC mode

<sup>d</sup> Oxygen content assumed to be reached during oxygenation [175]

## 6.2. Intrinsic properties of $\text{SmBa}_2\text{Cu}_3\text{O}_x$

Data of  $M(T)$ , used to determine  $T_c$  values from SQUID magnetometry applying DC mode, are presented in Fig. 6.1.1. The transition temperature and the superconducting-to-normal-state transition width for all investigated crystals are listed in Table 6.1.2. Intrinsic properties were investigated for small crystals. For these crystals  $T_c$  was derived from AC susceptibility measurements performed using a 9 T Physical Property Measurement System (Quantum Design, PPMS) [176,177] with ACMS option, see Fig. 6.1.2. Similar  $T_c$  values were observed for crystals of different size but oxygenated simultaneously. The transition for the crystal denoted as S0, i.e. with the lowest  $T_c = 19.6$  K, starts at temperature as low as 5 K and, therefore, such crystal was not investigated for intrinsic superconducting parameters.

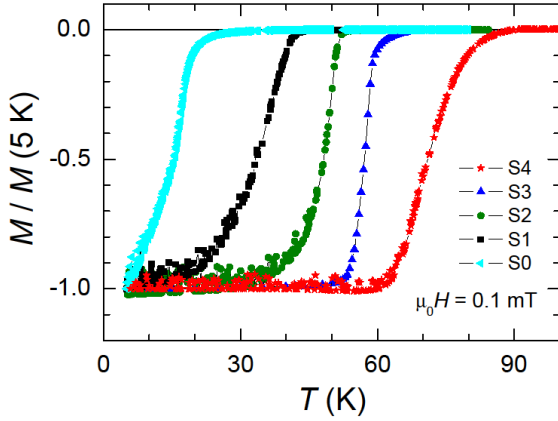


**Fig. 6.1.1.** Temperature dependence of the reduced magnetization for large crystals.

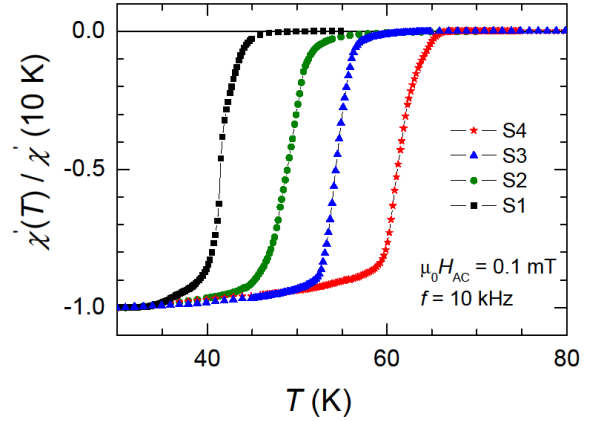


**Fig. 6.1.2.** Temperature dependence of the reduced real part of the susceptibility measured at a field of 0.1 mT and a frequency of 10 kHz for small crystals.

SQUID magnetometer was used to investigate the superconducting state properties. The magnetometer was supplied with a 7 T superconducting magnet and built by Quantum Design (model MPMS XL [178]). The properties were extracted from  $M(H)$  measurements for  $H \parallel c$ -axis and by applying the effective media approach to the experimental data, see Fig. 6.2.1.

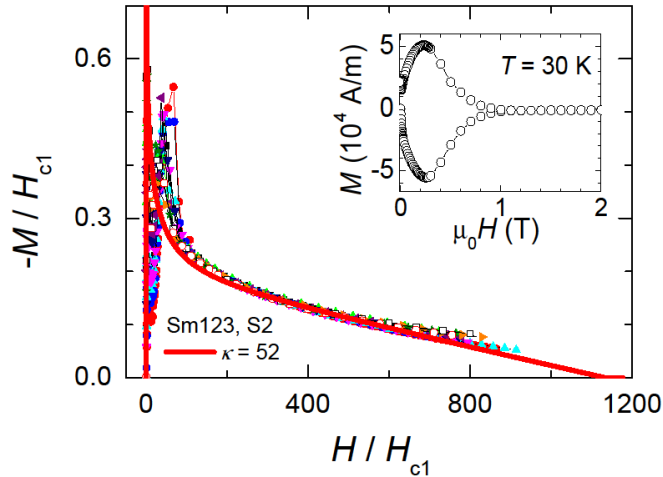


**Fig. 6.2.1.** Magnetization scaling for  $\text{SmBa}_2\text{Cu}_3\text{O}_x$  crystal with  $T_c = 51.5$  K (S2). Inset: field dependence of the magnetization at  $T = 30$  K for  $H \parallel c$ -axis.

A very good agreement between  $H_{c2}$  values determined from the reversible magnetization and the ones from magnetization scaling was found, see Fig. 6.2.2. This and

other parameters determined from the effective media approach ( $T_c$  and  $\gamma$  were determined differently) are listed in Table 6.2.1.

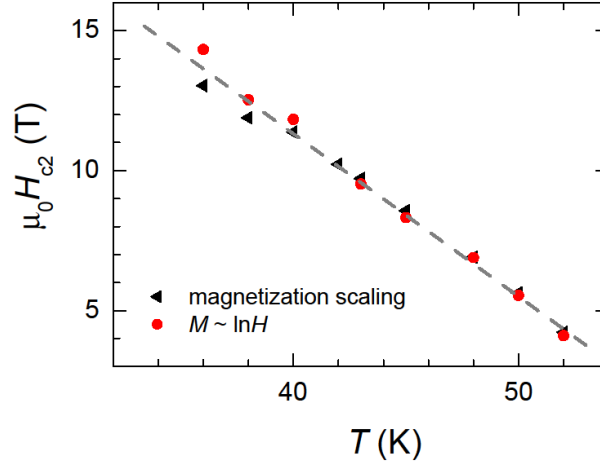


**Fig. 6.2.2.** Comparison between the upper critical fields for  $H \parallel c$ -axis obtained by applying the effective media approach to the experimental data and from extrapolation of the logarithmic  $M \sim \ln H$  dependence, see Eq. (2.1.4). The dashed line presents slope of  $dH_{c2}/dT$  fitted to the experimental data.

**Table 6.2.1.** Abbreviations for the investigated  $\text{SmBa}_2\text{Cu}_3\text{O}_x$  crystals, their transition temperature, coherence length, penetration depth, Ginzburg-Landau parameter, thermodynamic critical field, slope of  $dH_{c2}/dT|_{T=T_c}$ , upper critical field, lower critical field, and the averaged anisotropy parameter.

| Sample | $T_c$<br>(K) | $\xi_{ab}(0)$<br>(nm) | $\lambda_{ab}(0)$<br>(nm) | $\kappa^{\parallel c}$ a | $\mu_0 H_c(0)$<br>(T) | $\mu_0 dH_{c2}^{\parallel c}/dT _{T=T_c}$<br>(T/K) | $\mu_0 H_{c2}^{\parallel c}(0)$<br>(T) <sup>b</sup> | $\mu_0 H_{c1}^{\parallel c}(0)$<br>(mT) | $\gamma$ |
|--------|--------------|-----------------------|---------------------------|--------------------------|-----------------------|--|---|---|----------|
| S1     | 42.8         | 6.6                   | 345                       | 48                       | 0.17                  | -0.24  | 7.5   | 6.6                                     | 56.4     |
| S2     | 51.5         | 4.4                   | 244                       | 52                       | 0.23                  | -0.45  | 16.8  | 12.3                                    | 40.1     |
| S3     | 56.5         | 3.7                   | 191                       | 50                       | 0.26                  | -0.60  | 24.6  | 19.8                                    | 29.5     |
| S4     | 63.6         | 2.6                   | 183                       | 60                       | 0.45                  | -1.05  | 48.5  | 23.3                                    | 25.0     |

<sup>a</sup> Determined from the numerical solution of the Ginzburg-Landau equation

<sup>b</sup> Assuming clean limit and WHH dependence [165]

The anisotropy parameters were evaluated from measurements performed on PPMS with a torque option. A rough comparison between values obtained for  $\text{SmBa}_2\text{Cu}_3\text{O}_x$  and Y123 crystals leads to the conclusion that the anisotropy dependence on  $T_c$  is very similar for both cuprate superconductors (for an extensive analysis of the anisotropy parameter in underdoped  $\text{SmBa}_2\text{Cu}_3\text{O}_x$  see Sections 6.3, 6.4, and 6.5), see Fig. 6.2.3.

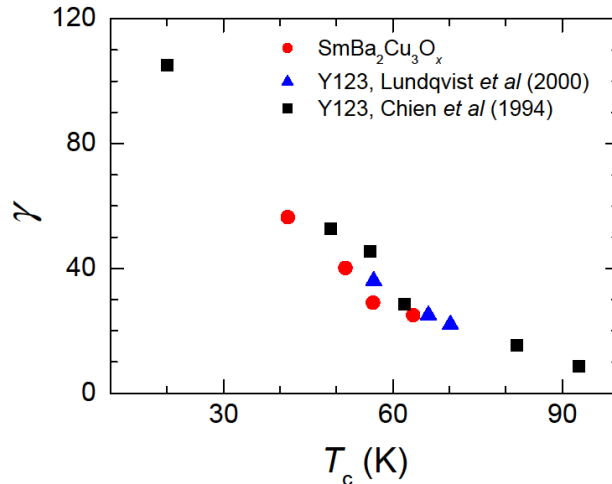


**Fig. 6.2.3.** Dependence of the anisotropy parameter on the critical temperature for  $\text{SmBa}_2\text{Cu}_3\text{O}_x$  (circles) and Y123 (from Refs [179,180], triangles and squares, respectively).

In Y123 the anisotropy parameter increases from 5 – 10 for optimally doped crystals, i.e. with  $T_c \sim 92$  K, to about 40 for a crystal with  $T_c \sim 50$  K [179]. The anisotropy parameter of 56.4 and 25.0 was found for  $\text{SmBa}_2\text{Cu}_3\text{O}_x$  crystals with  $T_c = 42.8$  K (i.e. S1) and  $T_c = 63.6$  K (i.e. S4), respectively. Removal of oxygen from the conducting  $\text{CuO}$  chains increases the effective mass anisotropy. The observed increase in  $\gamma$  value is related to a reduction of the coupling strength between adjacent  $\text{CuO}_2$  planes, as it was discussed already [181].

### 6.3. Historical remarks about the temperature dependence of the anisotropy parameter

The simplest description of anisotropy in layered superconductors relies on the classical anisotropic Ginzburg-Landau theory, which assumes a single band anisotropic system and temperature and field independent effective masses, as it was discussed already [182]. AGLT does neither account for the occurrence of an in-plane anisotropy in the tetragonal basal plane nor for the positive curvature of  $H_{c2}(T)$ . The first breakdown of a description within the AGLT approach was reported for niobium [183]. The non-spherical Fermi surface was proposed to be responsible for the observed temperature dependence of the upper critical field anisotropy [184]. It was shown later that the anisotropy of the electron-phonon interaction and of the Fermi velocity can indeed explain the superconducting properties of Nb [185,186]. A large (for a cubic material) anisotropy of

$H_{c2}$  was reported for  $\text{V}_3\text{Si}$  [187]. Moreover, anisotropy effects were observed in the basal plane of  $\text{Cs}_{0.1}\text{WO}_{2.9}\text{F}_{0.1}$  with sixfold symmetry, which fails to agree with AGLT which predicts an isotropic effective mass tensor [188]. In both materials, the anisotropy effects were suggested to be due to the shape and anisotropy of the Fermi surface [188,189]. Temperature dependent anisotropy parameters and a pronounced upward curvature of  $H_{c2}(T)$  were reported for  $\text{NbSe}_2$  and  $\text{LuNi}_2\text{B}_2\text{C}$  and originally attributed to nonlocal effects [190,191]. A nonlocal relation [192,193] between the current and the vector potential provides a formal bridge between the Fermi system of electrons in a given crystal and the interacting vortices in the superconducting condensate [194]. Such effects may be relevant for high purity samples. Initially, the borocarbides had been considered as simple *s*-wave superconductors [195] and the analysis of  $H_{c2}(T)$  using an anisotropic single gap model in  $\text{LuNi}_2\text{B}_2\text{C}$  resulted in anisotropic electron-phonon coupling and an anisotropy of the Fermi velocity [196]. Recently, strong support for multiband superconductivity in  $\text{LuNi}_2\text{B}_2\text{C}$  was provided [197] which should be followed by a re-examination of the previous analysis. An unusually strong temperature dependence of the anisotropy parameter was found for  $\text{MgB}_2$  (Refs [16,17]). An anisotropic single gap model, which results in an incorrect gap anisotropy of the order of 10, could not explain the temperature dependence of the anisotropy parameter, see Ref. [198] and references therein. It was suggested that the existence of different gaps was responsible for the temperature dependence of the anisotropy [17,171,198,199,200]. Recently, strong evidence for a temperature dependent anisotropy and indications for multiband superconductivity were reported for the iron-based superconducting pnictides [172,173,201,202,203,204].

#### 6.4. First evidence for a temperature dependent anisotropy in cuprates

Highly accurate anisotropy parameters can be obtained by applying torque magnetometry. For accurate investigation the temperature and the field range should, on one hand, be as broad as possible keeping  $H(T) < H_{c2}(T)$  and, on the other hand, minimize the torque hysteresis at angles close to  $90^\circ$ , i.e., for the  $H \parallel ab$ -plane. Here, underdoped  $\text{SmBa}_2\text{Cu}_3\text{O}_x$  crystals with  $T_c$ 's varying between 42.8 and 63.6 K were studied by torque magnetometry in a broad range of magnetic fields and temperatures. In all torque measurements a nearly reversible signal was obtained for clockwise and counterclockwise rotating the crystal in the full angular range in steps of  $0.5^\circ$ , see example in Fig. 6.4.1.

Therefore, excellent fits of Eq. (5.1.4) to the torque data were obtained which makes errors due to averaging of the torque negligible and the derived anisotropy parameter highly reliable. If temperature is too close to  $T_c$ , critical fluctuations are too strong and it is not possible to evaluate anisotropy parameter from Eq. (5.1.4) [205,206]. Therefore, temperatures very close to  $T_c$  were avoided.

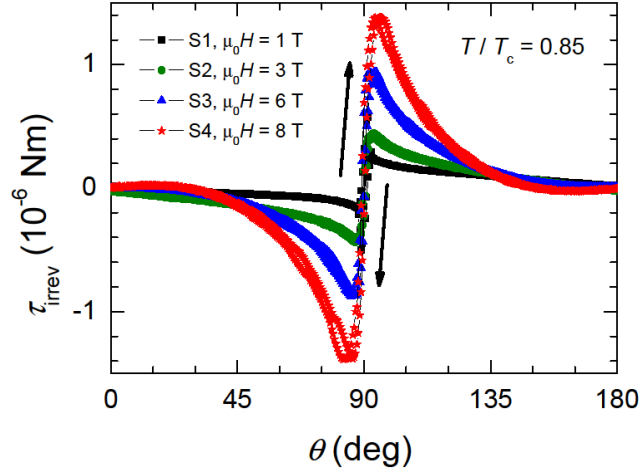


**Fig. 6.4.1.** Clockwise and anticlockwise angular dependence of the torque for all crystals recorded at a reduced temperature  $T/T_c = 0.85$  in different magnetic fields.

There is a paramagnetic background contribution to the superconducting torque (separated from the torque signal prior evaluation of the results). Such contribution does not affect  $\gamma$  significantly, see Fig. 6.4.2, in contrast to the effect on  $H_{c2}^{\parallel c}$ , which may easily differ by 50%. An example of a raw torque data before and after subtracting the background and a background contribution are shown in Fig. 6.4.2. Therefore, it is reasonable to fix  $H_{c2}^{\parallel c}$  using  $H_{c2}^{\parallel c}(T)$  values obtained using another method, thus reducing number of free parameters in Eq. (5.1.4). Additionally, as already shown [172], small errors in the  $H_{c2}$  values do not affect much the anisotropy parameter extracted from the fit of Eq. (5.1.4) for the angular torque dependence. The value  $\eta$  was fix to 1, as is commonly set in such analysis. The remaining parameters of Eq. (5.1.4) are then extracted simultaneously in the torque fitting procedure. The temperature dependence of  $A(T)$  is usually well approximated by  $A(T) = C_1/T + C_2$ , which is consistent with a Curie-Weiss paramagnetism.



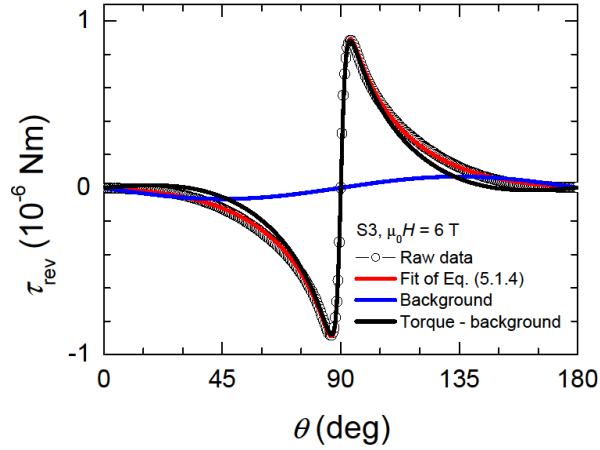


**Fig. 6.4.2.** The reversible torque before and after subtracting the paramagnetic background contribution with the amplitude  $A$  described by the Eq. (5.1.4).

In order to overcome significant irreversibility at angles near  $90^\circ$  the measurements had to be performed in applied fields close to  $H_{c2}^{\parallel c}$ , i.e. for  $H > 0.6H_{c2}^{\parallel c}(T)$ . In those cases the fit of Eq. (5.1.4) to the torque was performed in a reduced, e.g.  $60^\circ < \theta < 120^\circ$ , angular range to fulfil the condition  $H \ll H_{c2}$ . No significant curvature of  $H_{c2}^{\parallel c}(T)$  was observed in the vicinity of  $T_c$ , which is common for cuprates in fields applied along the uniaxial axis.

The measurements performed in a constant magnetic field show an increase of the anisotropy parameter with decreasing temperature. This behaviour was found for all  $\text{SmBa}_2\text{Cu}_3\text{O}_x$  crystals studied, see Fig. 6.4.3. For the crystal with the lowest  $T_c = 42.8$  K, the anisotropy, recorded in a magnetic field of 2 T, increases from  $35.9 \pm 0.8$  to  $59.2 \pm 1.2$  while lowering the temperature from 40 to 36 K. For  $\text{SmBa}_2\text{Cu}_3\text{O}_x$  with the highest  $T_c = 63.6$  K, the observed increase in the same magnetic field is from  $13.6 \pm 0.2$  to  $21.8 \pm 0.1$  upon decreasing the temperature from 62 to 59 K. The increase of the anisotropy parameter amounts to over 50 % in both cases. Due to the very different upper critical field values among the crystals, a comparison of the temperature dependence of the anisotropy parameters can be presented at constant  $H/H_{c2}^{\parallel c}$  values, see Fig. 6.4.3.

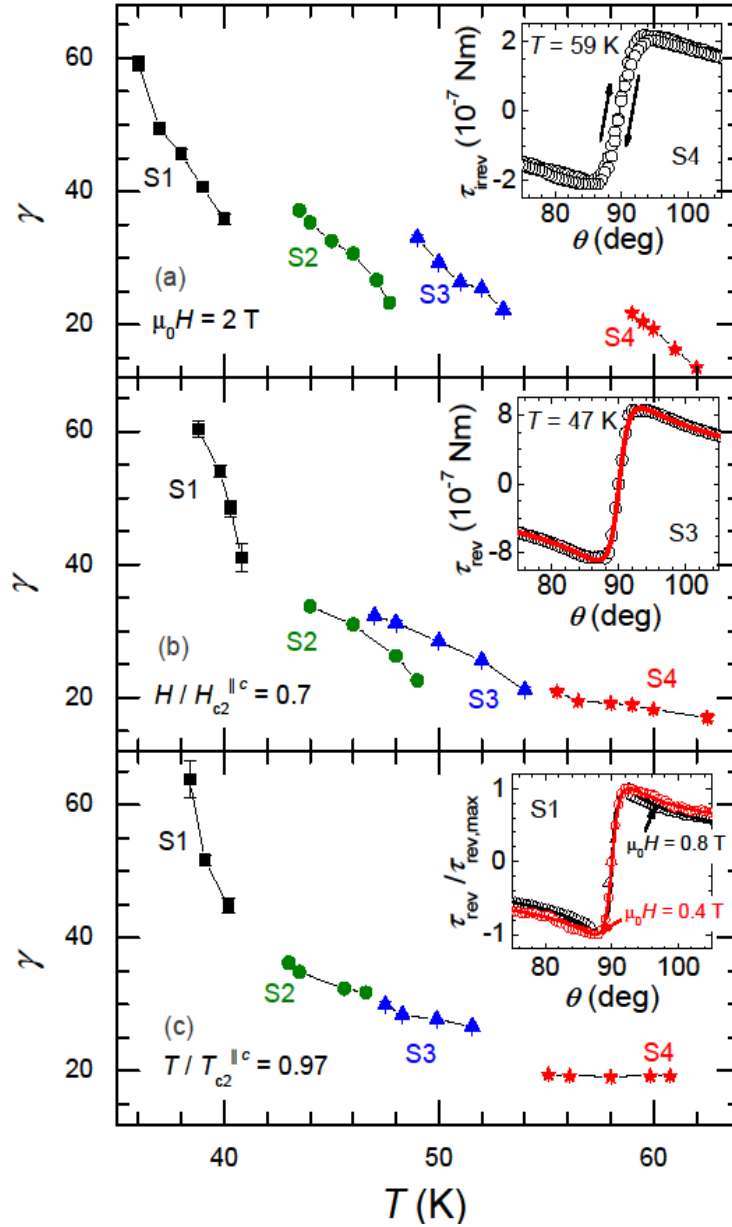


**Fig. 6.4.3.** Temperature dependence of the anisotropy parameter a) at  $\mu_0 H = 2$  T, b) at a reduced field  $H/H_{c2}^{||c}$  of 0.7, c) at a reduced temperature  $T/T_{c2}^{||c}$  of 0.97. Insets: a) example of the clockwise and anticlockwise angular dependence of the torque at  $\mu_0 H = 2$  T and  $T = 59$  K. b) Example of the reversible torque at  $H/H_{c2}^{||c} = 0.7$  and  $T = 47$  K fitted with Eq. (5.1.4). c) Example of the reduced reversible torque at  $T/T_{c2}^{||c} = 0.97$  and  $\mu_0 H$  equal 0.4 and 0.8 T fitted with Eq. (5.1.4).

The anisotropy parameter decreases with increasing temperature and appears to be in first approximation a linear function of temperature with a slope that depends on the  $T_c$  of the crystal. This slope changes from  $-8.6 \text{ K}^{-1}$  to  $-0.5 \text{ K}^{-1}$  for the crystals with  $T_c$  increasing from 42.8 to 63.6 K. Additionally, in order to verify that the temperature dependence of the anisotropy parameter is not influenced by thermal fluctuations, data points in Fig. 6.4.3

are presented at constant  $T/T_{c2}^{\parallel c}$  values. Here,  $T_{c2}^{\parallel c}$  is the temperature of the superconducting-to-normal state transition in a magnetic field applied along the crystallographic  $c$ -axis. Again, a clear dependence of the anisotropy parameter on the temperature is visible. An example of the reversible torque at two different temperatures/fields with the fits of Eq. (5.1.4) is presented in the inset of Fig. 6.4.3. Such a comparison provides evidence for an increase of the anisotropy parameter with decreasing temperature. Taking the above into account, we conclude that the temperature dependence of the anisotropy parameter is an intrinsic property of  $\text{SmBa}_2\text{Cu}_3\text{O}_x$ . The anisotropy increases with decreasing temperature for underdoped  $\text{SmBa}_2\text{Cu}_3\text{O}_x$  and appears to depend more strongly on temperature for the crystals with lower  $T_c$ , i.e. for more strongly underdoped crystals.

Despite large anisotropy values and no shaking technique used in evaluation of torque data for  $\text{SmBa}_2\text{Cu}_3\text{O}_x$ , very good fits of Eq. (5.1.4) to the experimental data were obtained. Vortex shaking is based on the application of an additional oscillating magnetic field perpendicular to the main field, which pushes the vortices from weak pinning centres and extends the reversible region in the  $(H, T)$  phase diagram [71]. In  $\text{SmBa}_2\text{Cu}_3\text{O}_x$ , hysteresis peaks at  $\theta \sim 90$  deg were not observed hence no indications for intrinsic pinning were reported. This is probably due to large density of point-like defects. Point defect mask the pinning of vortex lines between the  $\text{CuO}_2$  planes. On the other hand, removal of oxygen from the conducting  $\text{CuO}$  chains leads to a more pronounced 2D behaviour. Therefore, the temperature of the 3D-2D crossover and the crossover field should be examined for underdoped cuprate. As an example, for  $\text{SmBa}_2\text{Cu}_3\text{O}_x$  crystal with  $T_c = 56.5$  K, denoted as S3, and at  $T = 50$  K, values of  $H_{c2}^{\parallel c} = 3.9$  T and  $\xi_{ab} = 9.2$  nm can be evaluated. Then the anisotropy parameter  $\gamma(50 \text{ K}) \approx 28$  gives  $\xi_c = 0.33$  nm. This coherence length is much shorter than the  $\text{CuO}_2$  interplanar distance  $s \sim 0.8$  nm [91]. The crossover field  $H_{\text{cr}}$  and temperature  $T_{\text{cr}}$  for crystal S3 is 2.64 T and 54.5 K, i.e.  $T_{\text{cr}} = 0.96T_c$ , respectively. The 2D-3D crossover in the investigated underdoped cuprate occurs at very low fields and/or high temperatures. As a comparison, in the case of  $\text{La}_{1.925}\text{Sr}_{0.075}\text{CuO}_4$  torque measurements [207] indicated a 2D-3D crossover at  $T_{\text{cr}} = 0.8T_c$ . Since for all of the underdoped  $\text{SmBa}_2\text{Cu}_3\text{O}_x$  crystals values of  $\xi_c(T)$  are smaller than the interplanar distance, the magnetic torque should be described within the 2D LD approach. In reality, deviations from the 3D London approach are due to the scaling function  $\varepsilon(\theta)$ , see Section 2.1, and become only important for angles  $\theta < \theta_0 = \tan^{-1}(1/\gamma)$ , [208] i.e., for angles of the order of  $1^\circ$  away from the  $ab$ -plane geometry in

the case of HTSC. Moreover, it was shown that the 3D London model successfully applies to the highly anisotropic Bi-based and Hg-based superconductors [209,210] with anisotropy higher than that of  $\text{SmBa}_2\text{Cu}_3\text{O}_x$ . Finally, lack is of a theory describing the anisotropy in strongly layered HTSC that would reconsider the interlayer coupling in highly underdoped cuprates. Therefore, the AGLT approach was applied for the analysis of the underdoped  $\text{SmBa}_2\text{Cu}_3\text{O}_x$  data.

It was shown that in the case of the  $\text{MgB}_2$  and pnictides, superconductors where a strong temperature dependence of the anisotropy parameter was found, two anisotropy parameters, namely of the penetration depth,  $\gamma_\lambda(T)$ , and of the upper critical field,  $\gamma_{H_{c2}}(T)$ , were distinguished. The evidence for the existence of two parameters was found due to application of two different techniques of measurements. While anisotropy in small magnetic field was investigated, i.e. by investigating the lower critical field, anisotropy parameter corresponding to the anisotropy of the penetration depth was probed in  $\text{MgB}_2$  [171,211]. The anisotropy parameter investigated by the torque technique, i.e. with magnetic fields  $H_{c2}^{\parallel c} \ll H \ll H_{c2}^{\parallel ab}$ , corresponds to the anisotropy of the upper critical field in  $\text{MgB}_2$  [16,17]. In  $\text{MgB}_2$   $\gamma_\lambda$  decreases with decreasing temperature from about 2 to 1.1, whereas  $\gamma_{H_{c2}}$  increases from about 2 at  $T_c$  to values of up to 6 at low temperatures. In the pnictides superconductors, a similar situation appears to be present, but with reversed signs of the slopes of  $\gamma_\lambda(T)$  and  $\gamma_{H_{c2}}(T)$ . The anisotropy parameter investigated by the torque technique corresponds to the anisotropy of the penetration depth which exhibits a pronounced increase with decreasing temperature. According to recent resistivity measurements  $\gamma_{H_{c2}}$  decreases with decreasing temperature [173]. Close to  $T_c$  both anisotropies have very similar values of  $\gamma_\lambda(T_c) \approx \gamma_{H_{c2}}(T_c) \approx 7$ , whereas at low temperatures the magnetic penetration depth anisotropy  $\gamma_\lambda(0) \approx 19$  and the upper critical field anisotropy  $\gamma_{H_{c2}}(0) \approx 2$  [172].

It would be of interest to compare the anisotropy parameters for  $\text{SmBa}_2\text{Cu}_3\text{O}_x$  extracted from the torque for  $T \rightarrow T_c$  with those for the anisotropy of  $H_{c2}$  near  $T_c$ . However, for strongly underdoped samples, the anisotropy is very sensitive to the oxygen content. Hence, to make the comparison, measurements should be performed on the samples annealed at the same conditions. No attempts to obtain the upper critical field anisotropy directly from magnetization measurements were made because of the large anisotropy (as in the underdoped cuprate superconductors) as well as a paramagnetic background contribution (which could be avoided e.g. in the case of  $\text{MgB}_2$ ). The large anisotropy makes the crystal's orientation for  $H$  along the  $ab$ -plane critical in deriving the exact  $\gamma$  value. High value of

the anisotropy parameter of underdoped crystals may exclude accurate determination of anisotropy of the upper critical field in transport measurements due to problems with  $H \parallel ab$  orientation of the sample.

In contrast to the clear temperature dependence in  $\text{SmBa}_2\text{Cu}_3\text{O}_x$ , the dependence of the anisotropy parameter on the magnetic field is rather weak. The anisotropy decreases somewhat for higher magnetic fields at the same temperature, see Fig. 6.4.4. Nevertheless, since this effect is not so pronounced, it cannot be rule out that it results from systematic errors coming e.g. from a systematic change of the hysteresis width with magnetic field. Strong pinning close to the  $ab$ -plane affects the positions of the peaks in the reversible (averaged) torque and hence makes the derived anisotropy parameter uncertain. The weak decrease of the anisotropy parameter with increasing magnetic field may as well be due to the reduced angular range of the fit of Eq. (5.1.4) to the data, when the field approaches  $H_{c2}^{\parallel c}$ , see the inset of Fig. 6.4.4.

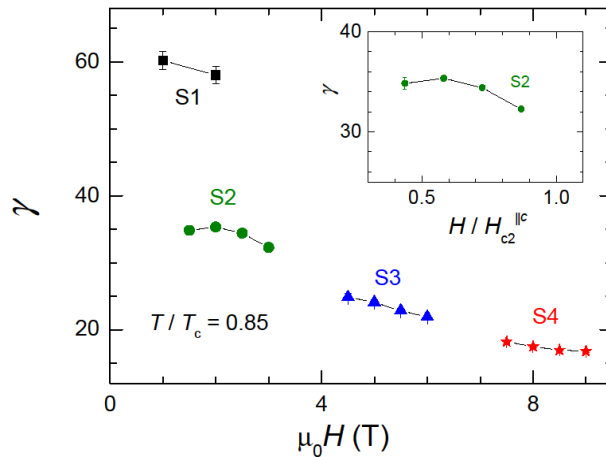


**Fig. 6.4.4.** Field dependence of the anisotropy parameter at fixed reduced temperature. Inset: reduced field dependence of the anisotropy parameter for the crystal with  $T_c = 51.5$  K (S2).

The field dependence of the anisotropy parameter in  $\text{MgB}_2$  was reported [212] to monotonically increase with increasing field, at least for fields up to 1.5 T. In the lowest fields, this rise seems to be much steeper than above 0.5 T. The strong field dependence was explained qualitatively by a faster suppression with  $H$  of superconductivity in the more isotropic bands and increasing the relative contribution of the highly anisotropic bands. Such a suppression is consistent with the overall decrease of  $\lambda_{ab}^{-2}$  [212], see below. No field

dependence of the anisotropy parameter was reported in pnictides, at least for field up till 1.4 T [213].

The field dependence of the superfluid density in  $\text{SmBa}_2\text{Cu}_3\text{O}_x$  was investigated by extracting the values of  $\lambda_{ab}$  from the torque measurements performed in a wide range of temperatures. Representative torque data collected on two  $\text{SmBa}_2\text{Cu}_3\text{O}_x$  crystals in various magnetic fields are presented in Fig. 6.4.5. with the angular dependence approximated by Eq. (5.1.4). The in-plane penetration depth does not show a significant variation with magnetic field, see the representative data in the insets of Fig. 6.4.5.

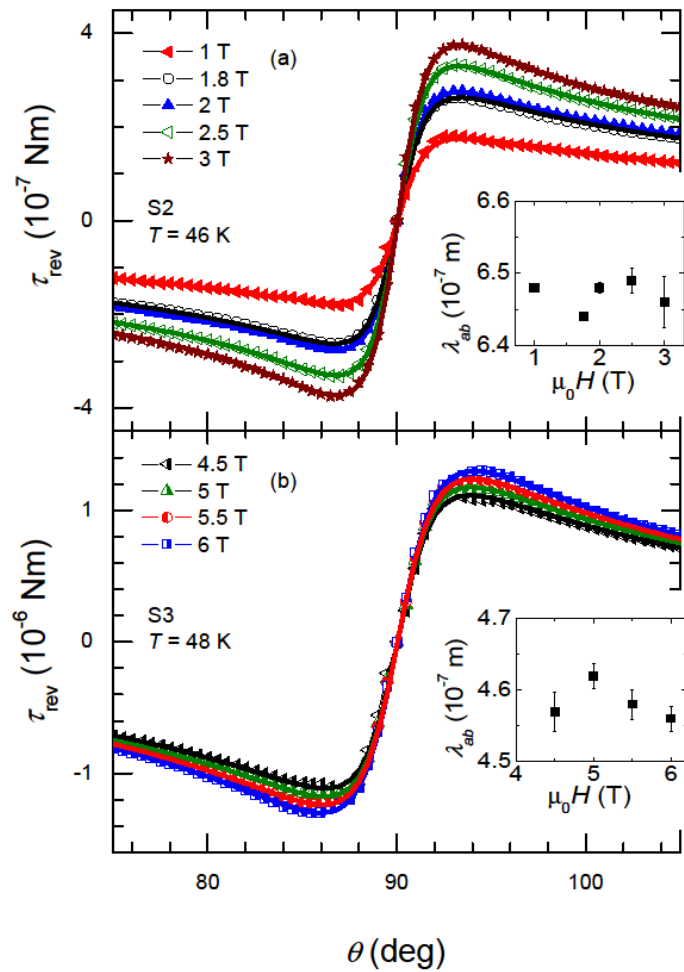


**Fig. 6.4.5.** Reversible angular torque for the crystals with  $T_c = 51.5$  K (S2) and with  $T_c = 56.5$  K (S3) fitted by Eq. (5.1.4), panel a) and b), respectively. Insets: a) example of the field dependence of the penetration depth for S2; b) same for S3.

The lack of a field dependence superfluid density in underdoped cuprates remains in contrast to observation in other HTSC. The superfluid density in  $\text{MgB}_2$  (Refs [212,214,215]), in the pnictides, [203] and in  $\text{La}_{1.83}\text{Sr}_{0.17}\text{CuO}_4$  (Ref. [216]) was found to be field dependent. It was found that  $\lambda_{ab}^{-2}$  decreases with increasing magnetic field for  $\text{MgB}_2$  and the pnictides [203,214], both materials for which a temperature dependent anisotropy parameter was reported. Multiband superconductivity was reported in  $\text{MgB}_2$  [14,15,16] and was suggested for the pnictides [172,217,218] or the cuprates [219,220,221]. It was pointed out, that superconducting gaps, characterized by different symmetries, show different field dependences. The suppression of the superfluid density with magnetic field in a  $d$ -wave gap is proportional to  $H^{1/2}$  (Ref. [222]) while it has a  $1/H^{1/2}$  dependence [221] in an  $s$ -wave gap.

### 6.5. Possible origins of the temperature dependence of the anisotropy in underdoped cuprates

The origin of the observed temperature dependence of the anisotropy parameter in  $\text{SmBa}_2\text{Cu}_3\text{O}_x$  may be related to one of at least five situations, as it was already explained extensively [182]: (i) multiband superconductivity, [211,213,223,224,225,226,227,228,229, 230] (ii) Fermi surface anisotropy, [231,232,233] (iii) unconventional pairing and anisotropy of the superconducting energy gap, [234,235,236,237,238,239,240,241] (iv) strong coupling, [242,243,244] (v) real limitations of AGLT in the case of highly underdoped superconductors due to their strictly layered structure. Nonlocality, which becomes observable when the mean free path becomes larger than the superconducting coherence length, may be a necessary ingredient for the situations (i)-(iii).

Multiband superconductivity was proposed as an extension of the conventional BCS theory [223] and the phenomenon of two-gap superconductivity was observed in several systems [224,225]. The temperature dependence of the anisotropy parameter may be explained by the existence of two topologically very different Fermi surfaces [171,198,211]. Some implications for multiband superconductivity in the cuprates appeared [220,245,246], but were not confirmed to date, see also [227]. The Fermi surface in the cuprates [229] is not yet fully understood and only recently an unambiguous observation of quantum oscillations in the Hall resistance of underdoped Y123 proved the existence of a well developed Fermi surface [230]. No evidence for a field dependent penetration depth was found in  $\text{SmBa}_2\text{Cu}_3\text{O}_x$ . However, for  $\text{SmBa}_2\text{Cu}_3\text{O}_x$ , the observed behaviour of  $1/\lambda_{ab}^2$  may be due to

the range of applied fields, which was dictated by the torque hysteresis and the  $H_{c2}^{\parallel c}$  values. Firstly, too small fields might not be large enough to suppress superconductivity in any of the bands. On the other hand, the smallest field used here was 1 T (in order to make the torque signal sufficiently strong), which might be already too large, as the suppression of one of the superconducting gaps was visible for fields below approximately 0.3 T in the case of  $\text{La}_{1.83}\text{Sr}_{0.17}\text{CuO}_4$  (Ref. [219]).

Detailed Fermi surface structures are essential to describe the upper critical field in type-II superconductors, as first noticed by Hohenberg and Werthamer [247] and shown later explicitly [231,232]. The calculations presented by Kita and Arai [232] clearly indicate that the Fermi surface anisotropy can be the main source of the upward curvature in  $H_{c2}$  near  $T_c$  and, therefore, may explain the temperature dependence of the anisotropy parameter. When the Fermi surface anisotropy is fully taken into account in energy band calculations, the numerical results excellently reproduce the experimental  $H_{c2}(T)$  values of conventional superconductors [233]. Due to the lack of knowledge of the Fermi surface structure in the underdoped cuprates, it is impossible to eliminate this scenario as the origin of the temperature dependence of the anisotropy parameter in  $\text{SmBa}_2\text{Cu}_3\text{O}_x$ .

Anisotropic  $d$ -wave pairing even in a superconductor with an isotropic Fermi surface can result in an upward curvature of  $H_{c2}(T)$  near  $T_c$ . An additional temperature dependence of the anisotropy parameter is obtained when assuming an anisotropic effective mass [234]. The gap symmetry in the cuprates appears not to be a pure  $d$ -wave [235,236,237,238] and indications of a mixed, i.e. ( $d + s$ ), symmetry in the cuprates have been concluded by many groups [237,239,240]. It has been shown so far, that the anisotropy of the superconducting order parameter can lead to changes in anisotropy with temperature of the order of 20% [241]. At present, the scenario, in which the temperature dependence of the anisotropy parameter observed in  $\text{SmBa}_2\text{Cu}_3\text{O}_x$  results from the anisotropy of the superconducting gap, must probably be included, although more investigations are needed to arrive at a final conclusion.

The main effect of having included strong-coupling corrections to  $H_{c2}(T)$  is to alter the electron effective mass, i.e. the Fermi velocity, from the band mass value [242]. A strong polaron coupling approach, proposed as a further extension of the BCS phonon-mediated superconductivity for the cuprates, [243,244] could possibly be included in this scenario. However, when detailed calculations are made, [244] strong coupling gives only minor



modifications to  $H_{c2}(T)$  and cannot explain the observed strong temperature dependence of the anisotropy parameter.

For  $\text{MgB}_2$  and the pnictides, two different anisotropy parameters were invoked following Kogan's approach [172,212,248]. For  $\text{SmBa}_2\text{Cu}_3\text{O}_x$ , with no significant field dependence of the anisotropy, this would imply the same temperature dependence for both  $\gamma_{H_{c2}}$  and  $\gamma_\lambda$ . No peculiarities in the angular dependence of the torque would suggest that  $\gamma_{H_{c2}}$  and  $\gamma_\lambda$  would not differ much. However, a direct determination of  $H_{c2}$  and of its anisotropy from the angular dependence of the torque was not possible. Furthermore, additional independent anisotropy measurements that would indicate different anisotropies, i.e. of the penetration depth and the coherence length, are lacking. Therefore, it would be highly speculative at present to suggest that the temperature dependence of  $\gamma$  may originate from two anisotropy parameters.

At last, the observed strong temperature dependence of the anisotropy in the underdoped  $\text{SmBa}_2\text{Cu}_3\text{O}_x$  may also have quite a different origin as mentioned above. A temperature independent effective mass anisotropy is one of the basic assumptions of AGLT, leading, for a single gap superconductor, to a temperature independent anisotropy of the penetration depth and of the coherence length. However, this may not be true for highly underdoped superconductors. For a strongly layered superconductor with Josephson coupled planes, a reduction of the interlayer coupling with temperature would imply an increase in the anisotropy parameter. According to the LD model,  $\xi_c = \xi_{ab} (m_{ab} / m_c)^{1/2} \propto \xi_{ab} t_\perp$ , where  $t_\perp$  is the interlayer coupling constant, which was found to be temperature dependent in a 2D system [249]. Therefore, it may be necessary to reconsider the temperature dependence of the interlayer coupling in highly underdoped cuprates and to formulate a new theory describing the anisotropy in strongly layered HTSC.

## 6.6. Extrinsic properties of $\text{SmBa}_2\text{Cu}_3\text{O}_x$

Extrinsic properties of all large size single crystals of  $\text{SmBa}_2\text{Cu}_3\text{O}_x$  were investigated by SQUID magnetometer. Measurements of  $M(H)$  for  $H \parallel c$ -axis were performed in a wide range of temperatures. Upon increasing the oxygen content in underdoped  $\text{SmBa}_2\text{Cu}_3\text{O}_x$ , the significant fields like the irreversibility field and the peak field shift, but the qualitative form of the hysteresis loop remains the same, see Fig. 6.6.1.

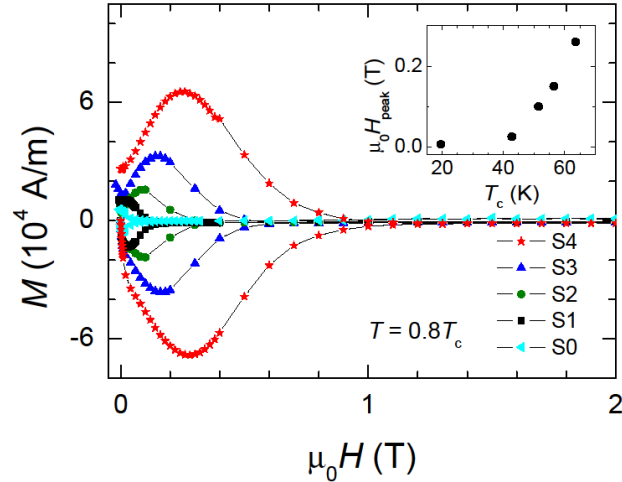


**Fig. 6.6.1.** Field dependence of the magnetization for studied crystals. Inset: relation between the field of the peak and  $T_c$  of the crystals.

There are two sources of hysteresis in magnetization, in particular bulk pinning and barriers to flux penetration. In the case of bulk pinning, besides reversible part of the magnetization, magnetization due to pinning is present. For  $\text{SmBa}_2\text{Cu}_3\text{O}_x$  crystal with the lowest  $T_c$  equal to 19.6 K, i.e. S0, the magnetization curve becomes asymmetric with respect to the zero magnetic field, which suggests that bulk pinning is very weak and contribution to hysteresis from barriers to vortex entry dominate. For crystals with higher  $T_c$ , bulk pinning provides major contribution to the hysteresis.

Since the discovery of HTSC, the phenomenon of the peak or fishtail effect (PE) [250] has been especially controversially discussed and numerous explanations have been proposed. The explanations of PE includes an increase in the microscopic pinning force, a matching effect, field induced granularity or pinning site activation, a crossover of pinning regimes, or a phase transition in the vortex matter [251]. In underdoped  $\text{SmBa}_2\text{Cu}_3\text{O}_x$  the field of the fishtail peak,  $H_{\text{peak}}$ , moves to higher fields for crystals with higher  $T_c$ , see inset of Fig. 6.6.1. This is expected as it is due to strengthening of the vortex pinning for crystals with higher  $T_c$ .

The irreversibility field at temperature of  $0.5 T_c$  shifts from 5.20 to 0.55 T while lowering  $T_c$  from 62.9 to 19.6 K, see Fig. 6.6.2. The irreversibility line shifts to lower fields in crystals with lower oxygen content, which agrees with the behaviour observed in Y123 [73,252].

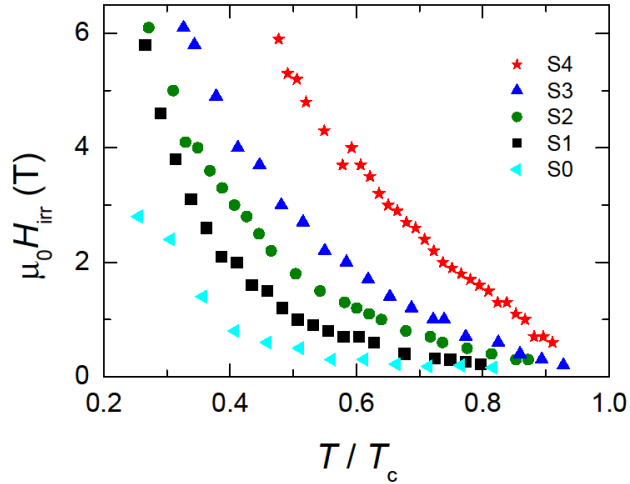


**Fig. 6.6.2.** Temperature dependence of the irreversibility line for  $H \parallel c$ -axis

In the temperature dependence of  $H_{\text{irr}}$ , presented in log-log scale, two slopes are visible, see Fig. 6.6.3. At fields equal  $H_{\text{cr}}$ , a change from a power law dependence, see Eq. (5.2.1), with  $\alpha$  around 1.5, to a more rapid temperature dependence at higher fields,  $\alpha = 3.2 \sim 4.8$ , was observed. Such increase of the exponent  $\alpha$  for higher fields is an indication of increasing two-dimensionality of the system at lower temperatures [252].

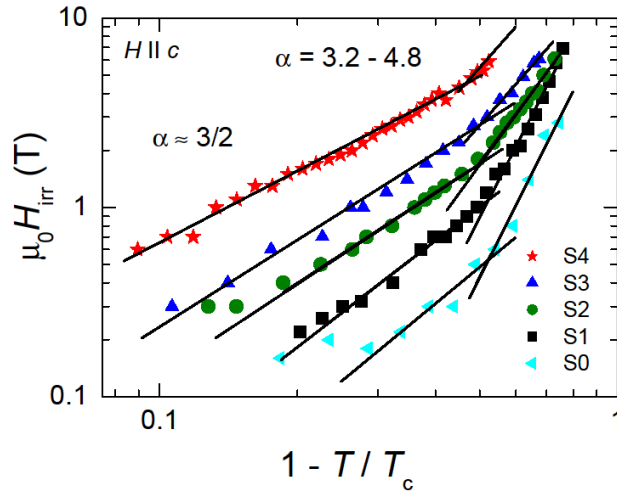


**Fig. 6.6.3.** Temperature dependence of the irreversibility line for  $H \parallel c$ -axis with log-log scale.

The crossover field  $H_{\text{cr}}$  for  $\text{SmBa}_2\text{Cu}_3\text{O}_x$  shifts from 4.1 to 0.53 T while lowering the  $T_c$  from 62.9 to 19.6 K. The crossover between three-dimensional and two-dimensional systems is due to a reduction of the in-plane hole concentration and matches the behaviour reported already for Y123 [180]. Nevertheless, values of  $H_{\text{cr}}$  for  $\text{SmBa}_2\text{Cu}_3\text{O}_x$  are

systematically higher than those found for Y123 single crystals, see Fig 6.6.4. This is due to more efficient vortex pinning in the former. Critical current density for  $\text{SmBa}_2\text{Cu}_3\text{O}_x$  was determined and is shown in Fig. 6.6.5.

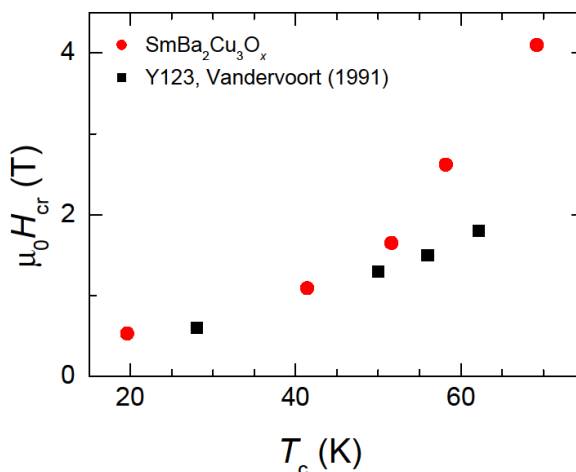


**Fig. 6.6.4.** Crossover field dependence on the transition temperature for  $\text{SmBa}_2\text{Cu}_3\text{O}_x$  and Y123 [253].

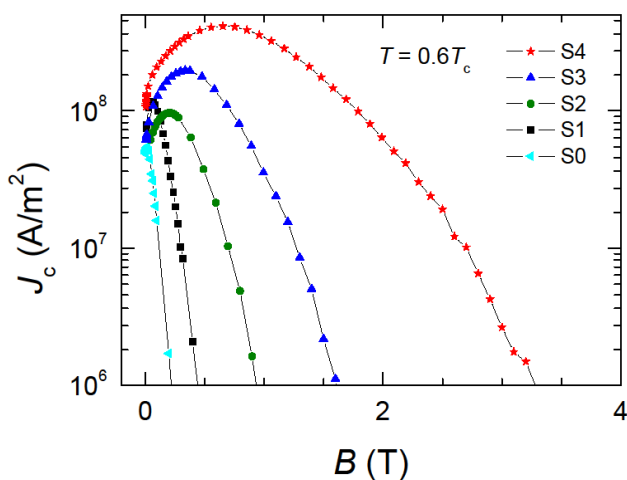


**Fig. 6.6.5.** Field dependence of the critical current density at reduced temperature.

Lower critical current density and a fast diminish of  $J_c(B)$  for higher field are due to highly reduced pinning force density for  $\text{SmBa}_2\text{Cu}_3\text{O}_x$  crystals with lower  $T_c$ , see inset of Fig. 6.6.6. The maximum pinning force density increases about 30 times when the  $T_c$  increases from 42.8 to 63.6. This agrees very well with the fact that the fishtail peak shifts to higher fields for crystals with higher oxygen content, see Fig. 6.6.1. In underdoped  $\text{SmBa}_2\text{Cu}_3\text{O}_x$  there are rather different mechanisms for pinning of the vortex lines on defects

at various temperatures. This is related to the lack of scaling of the reduced pinning force density for various crystals, see Fig. 6.6.6. For each of the studied crystal, position of the PE maximum shifts in the direction to  $B/B_k = 0.5$ , see representative on Fig. 6.6.7. Such a shift is a strong indication for increasing importance of the  $\delta T_c$ -type pinning at higher temperatures.

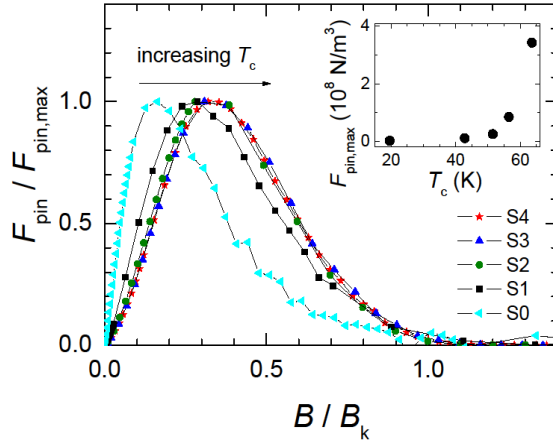


**Fig. 6.6.6.** Field dependence of the reduced pinning force density at  $T = 0.6T_c$ . Inset: dependence of the maximum pinning force density on the critical temperature of  $\text{SmBa}_2\text{Cu}_3\text{O}_x$  crystals.

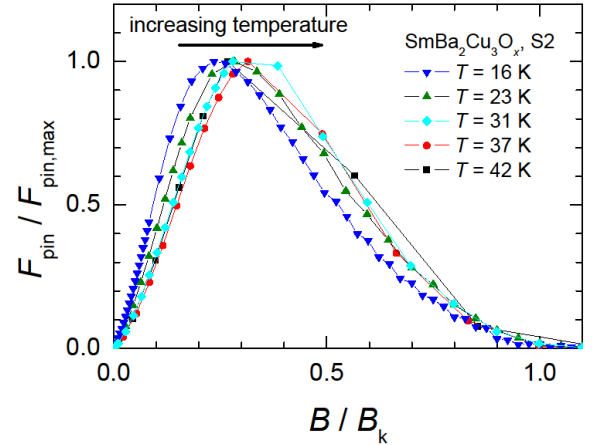


**Fig. 6.6.7.** Example of the field dependence of the reduced pinning force density at various temperatures, here for the crystal with  $T_c = 51.5$  K (S2).

## 6.7. Brief summary of the oxygen deficiency effect in $\text{SmBa}_2\text{Cu}_3\text{O}_x$

Underdoped single crystals of  $\text{SmBa}_2\text{Cu}_3\text{O}_x$  with  $T_c$  varying from 42.8 to 63.6 K were studied by SQUID and torque magnetometry. Irreversibility lines, crossover fields, and anisotropy parameters for  $\text{SmBa}_2\text{Cu}_3\text{O}_x$  were assessed and compared with those of  $\text{YBa}_2\text{Cu}_3\text{O}_{7-\delta}$  single crystals. The anisotropy dependence on  $T_c$  is very similar for both superconductors, but  $\text{SmBa}_2\text{Cu}_3\text{O}_x$  shows higher crossover fields than that of Y123 which are related to better vortex pinning in the former.

A careful study of the anisotropy in underdoped  $\text{SmBa}_2\text{Cu}_3\text{O}_x$  evidenced its temperature dependence. The anisotropy parameter decreases with increasing temperature and appears to be in first approximation a linear function of temperature with a slope that depends on the  $T_c$  of the crystal. This slope changes from  $-8.6 \text{ K}^{-1}$  to  $-0.5 \text{ K}^{-1}$  for the crystals with  $T_c$  increasing from 42.8 to 63.6 K. This effect is indeed intrinsic and its origin may be related to multiband superconductivity, Fermi surface anisotropy, unconventional pairing and

anisotropy of the superconducting energy gap, and/or strong coupling. However, it may also be necessary to reconsider the temperature dependence of the interlayer coupling in highly underdoped cuprates and to formulate a new theory describing the anisotropy in strongly layered HTSC. Only a very weak dependence of the anisotropy parameter on magnetic field was observed, but it cannot be excluded that this is the result of performing measurements at fields close to  $H_{c2}^{\parallel c}$ . No dependence of the superfluid density on the magnetic field was found. However, the observed behaviour of  $1/\lambda_{ab}^2$  may be due to the limited range of applied fields investigated, which was dictated by the torque hysteresis and the  $H_{c2}^{\parallel c}$  values.



## 7. Low level Pr substitution in $\text{YBa}_2\text{Cu}_3\text{O}_{7-\delta}$ : experimental results and discussion

Ions of Pr substituted in the place of Y in Y123 destroy superconductivity at substitution level of 55% of Pr and Pr123 is antiferromagnetic insulator [45,254]. The reason for the destruction of superconductivity remains unclear despite that several models have been analysed, including localization of holes [255,256], hole filling due to mixed valence of  $\text{Pr}^{3+}$  and  $\text{Pr}^{4+}$  ions [257,258] or pair breaking phenomena consistent with the classical Abrikosov-Gorkov pair-breaking theory [259,260]. Introduction of Pr ions causes insignificant changes in  $T_c$  of the parent compound at low substitution level [49] and it does not significantly affect the oxygen concentration [261]. Nevertheless, the effect of magnetic ions' concentration on the superconducting state parameters should be investigated for crystals with the same oxygen content. Increasing Pr ion concentration presumably affects both intrinsic and bulk, i.e. extrinsic, pinning. Moreover, it may be expected that introducing additional defects into HTSC, magnetic ions in particular, is an efficient way to modify the superconducting state anisotropy. A non-monotonic decrease of the superconducting state anisotropy parameter from  $\gamma \approx 6$  to around 3 with increasing Pr content from 0 to 10% (with simultaneous reduction of  $T_c$  by 6 K) was reported [258].

In this Section influence of Pr ions on superconducting state properties of  $\text{Y}_{1-x}\text{Pr}_x\text{Ba}_2\text{Cu}_3\text{O}_{7-\delta}$  (YPr123) single crystals with  $x = 0, 0.008, 0.013, \text{ and } 0.024$  is discussed. First, investigations to which extent low level Pr substitution influences the superconducting state parameters and the flux pinning properties in YPr123 were performed. Techniques of SQUID magnetometry and Hall probe scanning were used. Second, the torque magnetometry measurements of the superconducting state anisotropy are presented and analysed. That technique was also applied to examine transitions in the flux line lattice due to intrinsic pinning.

### 7.1. Single crystals of $\text{Y}_{1-x}\text{Pr}_x\text{Ba}_2\text{Cu}_3\text{O}_{7-\delta}$

Crystals of YPr123 were grown by TSSG technique in air. They were annealed in flowing oxygen at 500 °C. Normal pressure of the oxygen gas was used and the oxygenation lasted for 72 hours. Following oxygenation, two cooling procedures were applied to form two sets of samples. Slow cooling process is when crystals were cooled down with the speed of



20 °C/hour. Oppositely, furnace cooling procedure, i.e. fast cooling, is when the cooling speed exceeds 100 °C/hour. With the slow cooling, oxygen content close to the maximum, i.e.  $7-\delta \approx 7$ , can be achieved, see Tables 7.1.1 and 7.1.2. Finally, the small crystals were cut from bigger ones prior investigations applying torque magnetometer.

**Table 7.1.1.** Abbreviations for the investigated crystals, the crystals' size, and conditions of oxygenation.

| Sample   | Symbol   | X, Y, Z (mm) <sup>a</sup> | x, y, z (mm) <sup>b</sup> | Oxygenation temperature (°C) | Cooling |
|--|----------|---------------------------|---------------------------|------------------------------|---------|
| $\text{YBa}_2\text{Cu}_3\text{O}_{7-\delta}$                                 | 90K-Y123 | 4.30, 4.10, 1.00          | 1.09, 1.13, 0.41          | 500                          | slow    |
| $\text{Y}_{0.992}\text{Pr}_{0.008}\text{Ba}_2\text{Cu}_3\text{O}_{7-\delta}$ | YPr 0.8% | 1.25, 1.75, 0.52          | 1.05, 1.00, 0.45          | 500                          | furnace |
| $\text{Y}_{0.987}\text{Pr}_{0.013}\text{Ba}_2\text{Cu}_3\text{O}_{7-\delta}$ | YPr 1.3% | 5.20, 3.70, 1.20          | 1.05, 0.98, 0.30          | 500                          | slow    |
| $\text{Y}_{0.976}\text{Pr}_{0.024}\text{Ba}_2\text{Cu}_3\text{O}_{7-\delta}$ | YPr 2.4% | 4.70, 3.35, 2.10          | 0.85, 0.85, 0.20          | 500                          | slow    |

<sup>a</sup> Oxygenated crystals

<sup>b</sup> Crystals after cutting into smaller size for torque investigations

The XRD-analysis was performed to examine the crystals' quality and to determine lattice constants, see Table 7.1.2.

**Table 7.1.2.** Abbreviations for the investigated crystals, their lattice constants, critical temperature, the superconducting-to-normal state transition width, and the oxygen content.

| Symbol   | a, b, c (nm)              | $T_c$ (K) | $\Delta T_c$ (K) | $7-\delta^a$ |
|----------|---------------------------|-----------|------------------|--------------|
| 90K-Y123 | 0.38178, 0.38857, 1.16849 | 90.1      | 1.16             | 6.973        |
| YPr 0.8% | 0.38188, 0.38869, 1.16901 | 91.2      | 1.42             | 6.934        |
| YPr 1.3% | 0.38173, 0.38858, 1.16846 | 89.9      | 1.16             | 6.971        |
| YPr 2.4% | 0.38177, 0.38867, 1.16849 | 90.2      | 1.16             | 6.973        |

<sup>a</sup> According to Kruger *et al.*[97K134]

The oxygen content was calculated assuming the linear dependence of the  $c$ -axis lattice constant on  $7-\delta$ , as presented in Eq. (4.2.2). In the analysis, the  $c$ -axis parameter was the only one taken into account due to structural twinning, see Section 4.1. There is a very good correlation between the estimated oxygen content and the transition temperature of

the studied crystals, i.e. the lattice constants for crystals with almost identical values of  $T_c$  are almost identical.

The Pr content in YPr123 crystals was determined by an inductively coupled plasma (ICP) technique. ICP is an analytical technique used for the detection of trace metals in environmental samples. The primary goal of ICP is to get elements to emit characteristic wavelength specific light which can then be measured.

All crystals studied in this Section were naturally twinned. A typical example of the sample surface, obtained by polarized light microscopy, is shown in Fig. 7.1.1. The twin structure, its periodicity, and the width of domains vary among the crystals. Besides twins, growth-steps are visible, but they are generally present only on the surface and have a very weak pinning performance compared to the defects in the bulk. Twin structure was also evidenced in the XRD-analysis through double peaks in reflections characteristic for the in-plane directions.

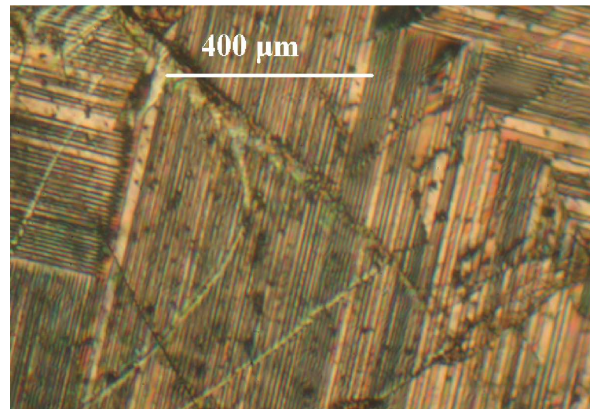


**Fig. 7.1.1.** Twin structure in the  $ab$ -plane of 90K-Y123.

Despite of a significant difference between ionic radius of Pr and Ba, probability for occurrence of the Pr-Ba substitutions, as mentioned in Section 4.3, should be examined. So far, only a limited substitution level has been reported, e.g. at 2.4% Pr only 0.3% of the Pr content substitutes on the Ba site with the remainder substituting on the Y site [262,263,264]. Secondly, superconductivity in  $\text{PrBa}_2\text{Cu}_3\text{O}_{7-\delta}$  was reported with  $T_c \approx 90$  K for a crystal that did not reach zero resistivity and only 7% of the sample volume showed the Meissner effect [265]. Bulk superconductivity in  $\text{PrBa}_2\text{Cu}_3\text{O}_{7-\delta}$  was reported in single crystals with  $T_c$  below 80 K [266]. The results presented here refer to single crystals with  $T_c$  and lattice constants

comparable to unsubstituted Y123. Therefore, any changes of the intrinsic superconducting parameters due to Pr substitution should be mainly caused by Pr substitution on Y site.

## 7.2. Influence of praseodymium ions on the intrinsic properties of $\text{Y}_{1-x}\text{Pr}_x\text{Ba}_2\text{Cu}_3\text{O}_{7-\delta}$

The influence of Pr ions on the intrinsic parameters was examined only for crystals with approximately the same oxygen content, i.e. oxygen content of  $7-\delta \approx 6.97$ . Transition temperature was determined from SQUID magnetometry using DC mode. No difference in  $T_c$ , within experimental error, was observed, see Fig. 7.2.1.

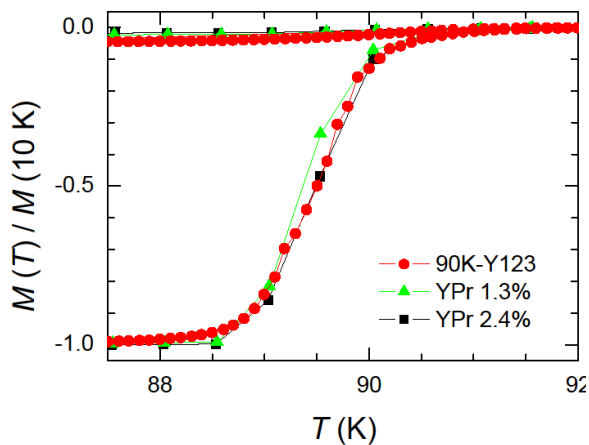


**Fig. 7.2.1.** Normalized temperature dependence of magnetization for YPr123 single crystals.

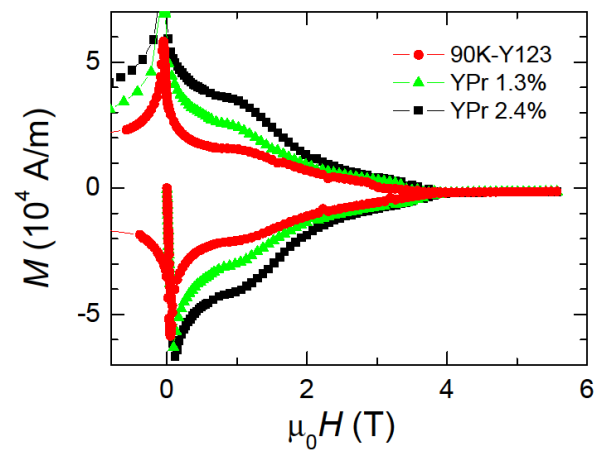


**Fig. 7.2.2.** Field dependence of magnetization for YPr123 crystals at  $T = 80$  K.

Measurements of magnetization  $M(H)$  for  $H \parallel c$ -axis were performed in broad range of temperatures using SQUID magnetometry. It is worth noting that upon Pr substitution, the relevant fields shift, but the qualitative form of the hysteresis loop remains the same, see Fig. 7.2.2. This is contradictory to the influence of defects created by fast neutron irradiation [267]. The different behaviour can be explained by the different defect structure: fast neutron irradiation leads to improved pinning properties due to collision cascades (extended defects of spherical shape, which act as strong pinning centres) and agglomerates of smaller defects, whereas in the case of Pr substitution defects are point-like and uncorrelated.

Analysis (fitting) of isothermal  $M(H)$  data, based on a rigorous approach to predict the  $M(H)$  behaviour, was performed to obtain superconducting state parameters, see

Fig. 7.2.3. Labusch-Doyle treatment [268,269] was applied. All of the superconducting state parameters evaluated for Pr-doped  $\text{YBa}_2\text{Cu}_3\text{O}_{7-\delta}$  single crystals are presented in Table 7.2.1. The value of  $H_{c2}^{\parallel c}$  extracted for 90K-Y123 agree very well with the data obtained by other authors [270].

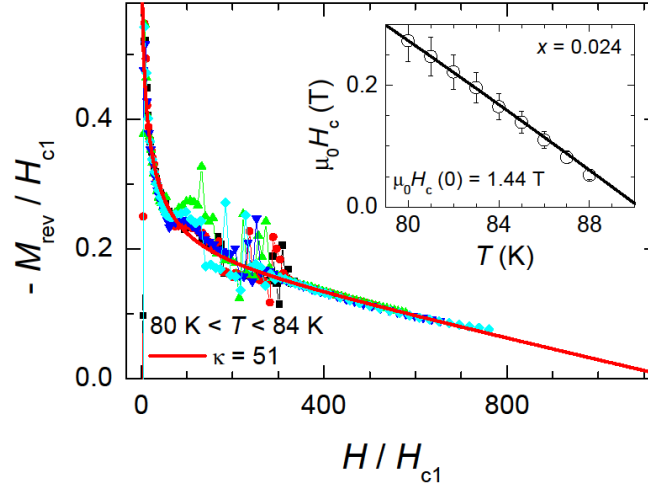


**Fig. 7.2.3.** Magnetization scaling for YPr 2.4%. The scatter of the experimental points below the reversible region is expected and related to the fishtail effect. Inset: fit of the theoretical expression, Eq. (5.2.2), to the thermodynamic critical field values.

**Table 7.2.1.** Coherence length, penetration depth, Ginzburg-Landau parameter, thermodynamic critical field, slope  $dH_{c2}/dT|_{T=T_c}$ , upper critical field, lower critical field, and the anisotropy parameter for YPr123 single crystals derived from torque magnetometry.

| Sample   | $\xi_{ab}(0)$<br>(nm) | $\lambda_{ab}(0)$<br>(nm) | $\kappa^{\parallel c}$ <sup>a</sup> | $\mu_0 H_c(0)$<br>(T) | $\mu_0 dH_{c2}^{\parallel c}/dT _{T=T_c}$<br>(T/K) | $\mu_0 H_{c2}^{\parallel c}(0)$<br>(T) <sup>b</sup> | $\mu_0 H_{c1}^{\parallel c}(0)$<br>(mT) | $\gamma$   |
|----------|-----------------------|---------------------------|-------------------------------------|-----------------------|--|---|---|------------|
| 90K-Y123 | 1.66                  | 86.3                      | 49                                  | 1.33                  | -1.83  | 119.6   | 97                                      | 7.17(0.17) |
| YPr 0.8% | 1.61                  | 105.4                     | 62                                  | 1.10                  | -1.93  | 127.7   | 68                                      | 7.87(0.21) |
| YPr 1.3% | 1.59                  | 84.3                      | 50                                  | 1.38                  | -2.00  | 130.5   | 102                                     | 7.38(0.30) |
| YPr 2.4% | 1.55                  | 84.0                      | 51                                  | 1.44                  | -2.09  | 136.6   | 103                                     | 7.38(0.47) |

<sup>a</sup> Determined from the numerical solution of the Ginzburg-Landau equation

<sup>b</sup> Assuming clean limit and WHH dependence [165]

For crystals with the same oxygenation level, low level Pr substitution is not expected to significantly change the intrinsic properties. This is consistent with a constant value of the GL parameter, within experimental error, obtained here. The similar values of

the coherence length suggest that defects of similar dimensions should be equally effective for vortex pinning in all crystals. The lower values of the penetration depth for 90K-Y123, YPr 1.3%, and YPr 2.4%, as compared with the value for YPr 0.8%, indicate an increase of the superconducting carrier density in the former. This agrees well with the shift to the overdoped region in the  $T_c(\delta)$  phase diagram. Both the upper critical field and the thermodynamic critical field, increase for higher Pr concentration in evenly oxygenated YPr123. Higher  $H_c$  values indicate higher values of the activation energy. Relation between the intrinsic parameters, the vortex pinning properties, and the change in the  $J_c(B)$  behaviour is discussed below.

The anisotropy of the upper critical field was determined as the anisotropy of the two slopes in the field dependence of the reversible magnetization, see Eq. (2.1.4) and Eq. (2.1.5), for  $H \parallel c$ -axis and  $H \parallel ab$ -plane with  $\lambda_a = \lambda_b = \lambda_{ab}$ . The anisotropy parameter is around 6.5, see Fig. 7.2.4 and agrees well with the values reported elsewhere [270,271]. Attempts to investigate the in-plane anisotropy were made, nevertheless, since investigated crystals are twinned (see Sections 4.1 and 7.1), such data cannot be treated as reliable and are not presented here.

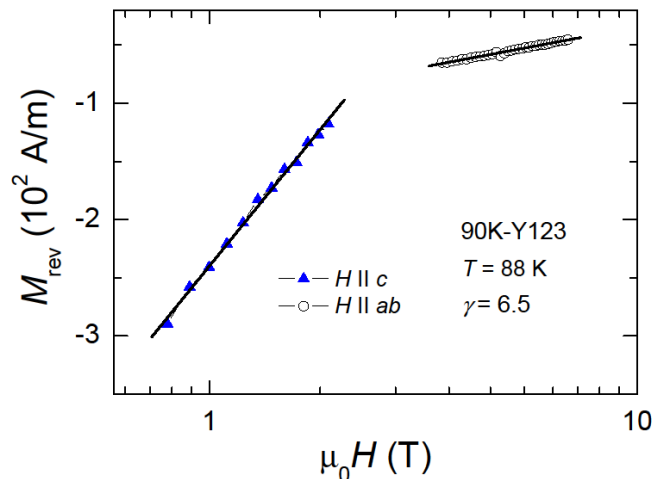


**Fig. 7.2.4.** Field dependence of the reversible magnetization for determination of the anisotropy parameter, with linear fits of Eq. (2.1.4) and Eq. (2.1.5) for  $H \parallel c$ -axis and  $H \parallel ab$ -plane, respectively.

For more accurate evaluation of the anisotropy parameter, torque magnetometry was applied, as discussed already extensively in Ref. [272]. An example of the angular torque dependence, measured for YPr 0.8%, is presented in Fig. 7.2.5. In the angular range  $0 - 70^\circ$

and  $110 - 180^\circ$ , the dependence of the torque for increasing and decreasing angles coincides, while two separate curves are observed in the angular range  $70 - 110^\circ$ . The first angular range corresponds to the reversible torque regime, the second to the irreversible regime. These two regions are distinguishable due to the angular dependence of the irreversibility lines, because  $H_{\text{irr}}$  in the  $H(T)$  phase diagram is much higher for  $H \parallel ab$  than for  $H \parallel c$ , as usual for cuprates. In the irreversible torque two well separated maxima are visible. The first, relatively wide, is located somewhat far from the  $ab$ -plane and its angular position is mainly related to the anisotropy parameter. The reversible torque in the angular range corresponding to the first torque maximum is well described by Eq. (5.1.4). The second maximum is located very close to the  $ab$ -plane. The reversible, i.e. averaged, torque at angles very close to  $90^\circ$  cannot be described within the 3D model and this maximum is attributed to intrinsic pinning, see Section 2.5.

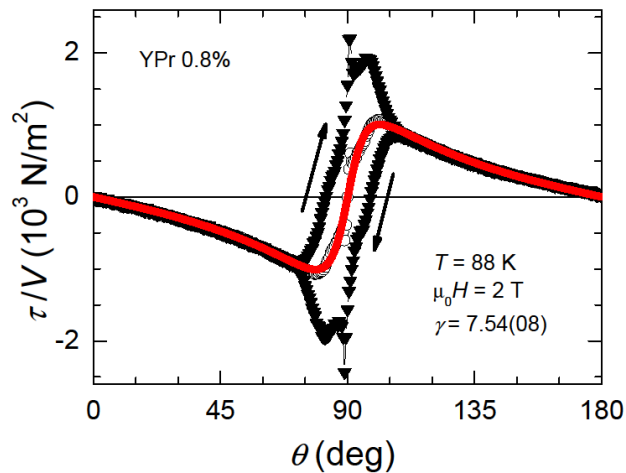


**Fig. 7.2.5.** Angular dependence of the torque for YPr 0.8%. Triangles denote the irreversible (clockwise and counterclockwise) and circles denote the reversible (averaged) torque. The solid line shows a fit of Eq. (5.1.4) to the data.

In this torque analysis  $H_{c2}^{\parallel c}(T)$  values were fixed to the ones extracted from magnetization scaling. As previously for  $\text{SmBa}_2\text{Cu}_3\text{O}_x$ ,  $\eta = 1$  was set. Anisotropy parameter extracted for 90K-Y123 by torque technique for various fields and temperatures,  $\gamma = 7.17 \pm 0.17$ , differs significantly from the parameter extracted from the reversible magnetization. In magnetization (or transport) measurements the crystal's orientation for  $H$  along the  $ab$ -plane is critical in deriving the exact  $\gamma$  value. Anisotropy values determined in those measurements are often underestimated. This is related to the scaling relation for

the upper critical field in case when magnetic field is not applied along the main crystallographic axis, namely  $H_{c2}(\theta) = H_{c2}^{\parallel c} / \varepsilon(\theta)$ . Even small misalignment of the crystal's  $ab$ -plane with respect to direction of the magnetic field leads to an errors in  $\gamma$  value according to the scaling function  $\varepsilon(\theta) = (\cos^2 \theta + \sin^2 \theta / \gamma^2)^{1/2}$ .

No change of the anisotropy parameter upon introduction of Pr ions was found, within experimental accuracy, for the Pr-doped Y123 crystals with Pr contents between 0 and 2.4% and oxygen deficiency  $\delta \approx 0.03$ , see Fig. 7.2.6.

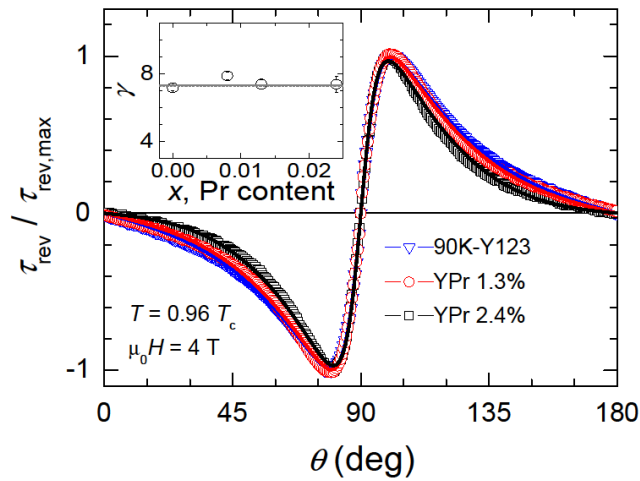


**Fig. 7.2.6.** Angular dependence of the normalized reversible torque and the corresponding fit of Eq. (5.1.4) to the data: 90K-Y123 (triangles), YPr 1.3% (circles), YPr 2.4% (squares). Inset: dependence of the anisotropy on the Pr content for all crystals, the line corresponds to the averaged anisotropy parameters for crystals with  $\delta \approx 0.03$ .

Examples of the torque data obtained at different temperatures for YPr 2.4% are presented in Fig. 7.2.7 and examples of the torque data in different fields for YPr 0.8% in Fig. 7.2.8. The insets of these Figures present the temperature dependence of the anisotropy parameter for YPr 2.4% and the field dependence of the anisotropy parameter for YPr 0.8%. Here, the error of the anisotropy was estimated from the difference between the anisotropy parameter derived from the fit of Eq. (5.1.4) to the reversible, i.e. averaged, torque and the parameter derived from the fit of Eq. (5.1.4) to the clockwise or counterclockwise angular dependence of the torque only. Thus, the quoted error represents the upper limit of errors due to the torque hysteresis, which is pronounced at low temperatures, see inset of Fig. 7.2.7, and at low fields, see inset of Fig. 7.2.8.

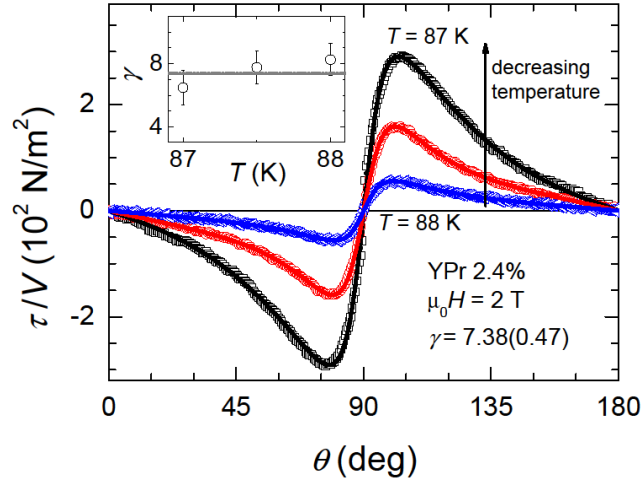


**Fig. 7.2.7.** Angular dependence of the reversible torque for YPr 2.4% at temperatures from 87 to 88 K at  $\mu_0 H = 2$  T and the corresponding fit of Eq. (5.1.4) to the data. Inset: temperature dependence of the anisotropy parameter with maximal errors due to torque hysteresis. The line is a guide to the eye.

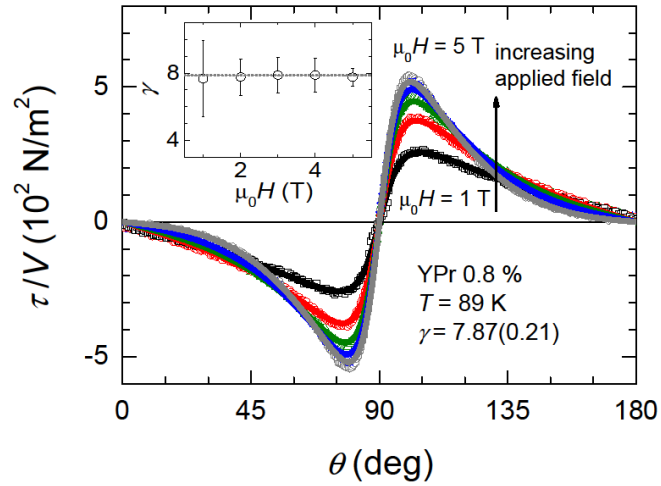


**Fig. 7.2.8.** Angular dependence of the reversible torque for YPr 0.8% at applied magnetic fields between 1 and 5 T at  $T = 89$  K and the corresponding fit of Eq. (5.1.4) to the data. Inset: field dependence of the anisotropy parameter with maximal errors due to torque hysteresis. The line is a guide to the eye.

Neither a temperature nor a field dependence of the anisotropy was found within experimental accuracy. However, it should be noted that, due to significant pinning, measurements were performed in a relatively narrow temperature range, much narrower than accessible for underdoped cuprates, see Section 6, and, therefore, the data cannot completely rule out a temperature or field dependence of the anisotropy parameter in overdoped or optimally doped HTSC.



The temperature dependence of  $\lambda_{ab}$  was extracted by fitting Eq. (5.1.4) to the experimental torque data. The values agree reasonably well with that obtained from magnetization scaling ( $\lambda_{ab}$  at  $T = 0.97T_c$ : for YPr 1.3%: 481 nm (torque), 426 nm (scaling); for 90K-Y123: 564 nm (torque), 455 nm (scaling)), see Fig. 7.2.9.

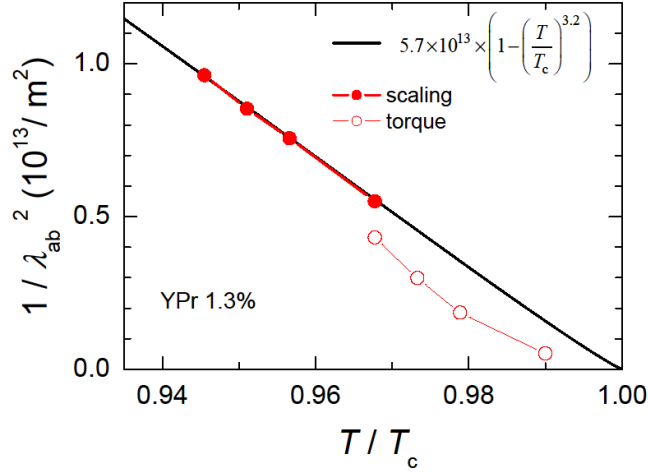


**Fig. 7.2.9.** Comparison of the penetration depth values at various temperatures obtained from magnetization scaling method and torque measurements for YPr 1.3%.

In general, the penetration depth may be described by following power law relation:

$$\lambda_{ab}^{-2}(T) = \lambda_{ab}^{-2}(0) \left[ 1 - \left( \frac{T}{T_c} \right)^n \right]. \quad (7.2.1)$$

Parameter  $n = 3.2$  was extracted for YPr 1.3%, which is somewhat smaller than  $n = 4$  characteristic for a superconductor in the very strong coupling limit [273]. On the other hand, the value of  $\lambda_{ab}(0)$  obtained from the power law fitting may only be a rough estimate since the torque measurements were performed only in a narrow temperature range close to  $T_c$ . Therefore, more accurate values for the penetration depth are expected to result from magnetization scaling. The zero temperature penetration depths obtained from magnetization scaling are listed in Table 7.2.2 and agree very well with the data obtained by other authors [274].

The temperature of the 3D-2D crossover, see Eq. (5.5.3), occurs in the temperature range 61 – 80 K for the investigated crystals. The parameters used in the calculation are as follows:  $\gamma = 5 - 8$ ,  $\zeta_{ab} = 1.6$  nm [266],  $T_c = 89.9 - 91.2$  K,  $s = 0.8$  nm [91,275]. The field corresponding to the 3D-2D crossover, see Eq. (5.5.2), is in the range 50 – 130 T, i.e. at

values much higher than those reached in the measurements. As a result, the assumption of continuous vortex lines and cores, made in the 3D anisotropic model, i.e. in Eq. (5.1.4), is valid in the full range of investigated temperatures and magnetic fields.

### 7.3. Influence of praseodymium ions on the bulk pinning in $\text{Y}_{1-x}\text{Pr}_x\text{Ba}_2\text{Cu}_3\text{O}_{7-\delta}$

Analysis of the vortex pinning was based on magnetization measurements and evaluation of the critical current density and on fitting of the experimental  $M(H)$  using algorithm for  $B_{\text{eq}}(H)$  with included formula for  $J_c(B)$ . The fitting was performed by taking into account both background and PE contributions to the critical current density, see Section 2.7, and was extensively discussed in Ref. [276]. In the fitting procedure, the total critical current is described by following equation:

$$J_c = J_{c1} \exp\left(-\alpha \frac{B}{B_{\text{peak}}}\right) + J_{c2} \left(\frac{B}{B_{\text{peak}}}\right) \exp\left\{\left[1 - \left(\frac{B}{B_{\text{peak}}}\right)^n\right] \frac{1}{n}\right\}. \quad (7.3.1)$$

Parameter  $\alpha$  is due to an experimentally manifested background vortex pinning that is generally evident at low fields. Such background pinning is mainly related to geometrical effects and/or self-fields [110]. The self-field describes the maximum shielding field that reduces  $J_c$  at low external magnetic field. Parameter  $n$  depends on the influence of the applied field on the vortex structure and is associated with PE phenomenon. The smaller  $n$ , the less sensitive is pinning to changes of magnetic field. The parameters  $J_{c1}$  and  $J_{c2}$  correspond to the critical current density amplitudes due to pinning at low fields and due to the actual interaction of vortex matter with the pinning structure, respectively. Because the above parameters scale with  $H_{c1}$ , it is often better to use  $\beta = J_{c2}/J_{c1}$ , the relative critical current density amplitude.

Measurements on 90K-Y123 were performed in a broad temperature range. In the temperature range 55 – 89 K a fishtail effect for  $T \leq 60$  K and for  $80 \text{ K} \leq T \leq 87$  K was found. The lack of temperature scaling of the normalized pinning force density (see inset of Fig. 7.3.1) suggests that more than one type of defects is present in this crystal. Twin boundaries do not play a dominant role when the spacing between twins is large compared to the flux lattice spacing, i.e. twins should only play a role at low fields. Therefore, oxygen

vacancies and twin boundaries are responsible for pinning in the high and low field regimes, respectively.

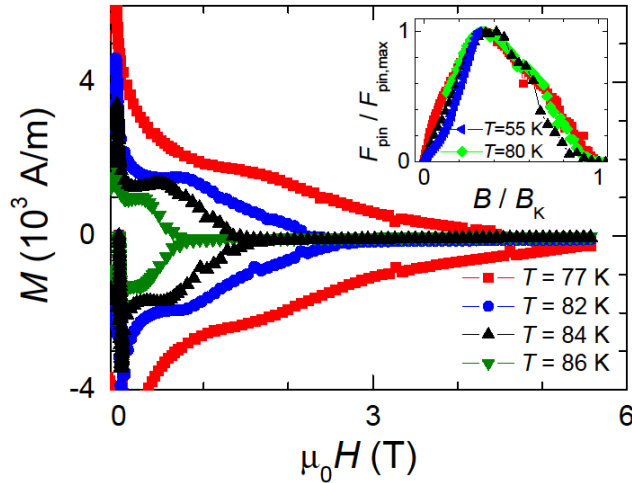


**Fig. 7.3.1.** Hysteresis loops for 90K-Y123. Inset: normalized pinning force density at 55, 77, 80, and 84 K.

The largest value of the parameter  $\alpha$  ( $\alpha = 2.5$ ), see Fig. 7.3.2, indicates that the applied field strongly affects the background pinning. A change from field independent pinning due to defects being effective in a broad field-range ( $n = 1.6$ ) at low temperature, to more field-sensitive ( $n = 2.3$ ) pinning sites occurs, see upper inset of Fig. 7.3.2, and indicates thermally activated flux flow already above  $T = 79$  K. Generally, small  $n$ -value was obtained, which indicates that stable defects, i.e. effective in a broad range of fields, play a dominant role in flux pinning in the fish-tail region. The observed increase of the parameter  $\beta$  is most likely caused by a better interaction between the vortex matter and the pinning structure for larger and/or stronger defects. When the temperature reaches 86 K, the defects are no longer able to pin vortices, hence,  $\beta$  suddenly drops, see the lower inset of Fig. 7.3.2.

In the samples with partial substitution of Y by Pr, defects introduced by the magnetic ions are present in addition to oxygen vacancies and twins. No universal behaviour of the normalized pinning force density at high fields for samples with different Pr content was observed, whereas a common behaviour was reported at low fields [277]. Pinning at low fields is probably due to oxygen vacancies and the small amount of Pr ions has no effect here. At high fields, on the other hand, the pinning force density strongly depends on the Pr content. Magnetization curves for Y123 substituted with Pr are presented in Figs 7.2.2 and

7.3.3. The PE shifts to lower fields for higher Pr substitution, see inset of Fig. 7.3.3, which is due to the strengthening of vortex pinning.

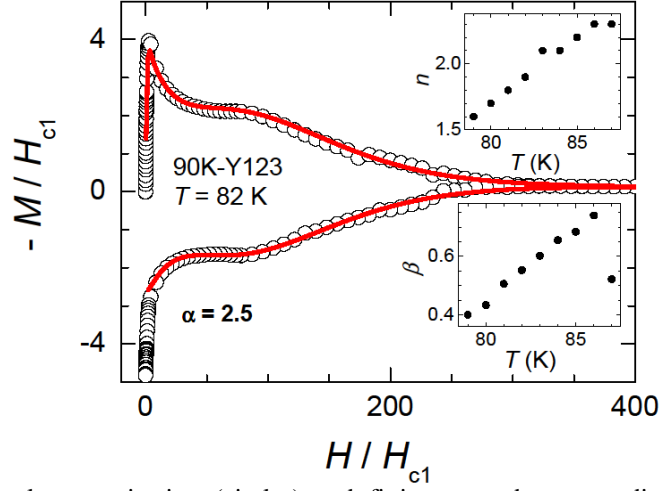


**Fig. 7.3.2.** Experimental magnetization (circles) and fitting procedure according to Eq. (7.3.1) (line) for 90K-Y123. Upper and lower insets: temperature dependence of pinning parameters  $n$  and  $\beta$ , respectively.

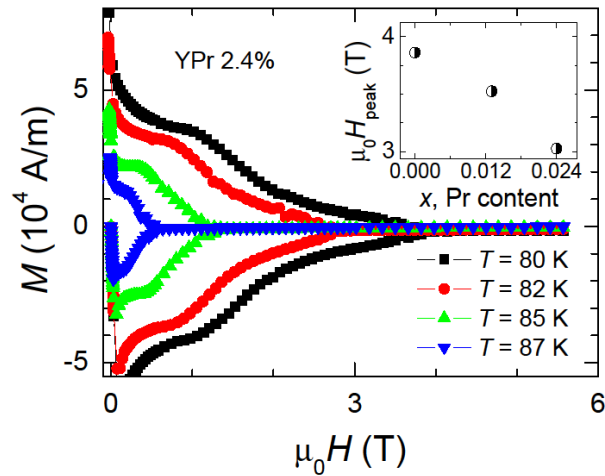


**Fig. 7.3.3.** Measured hysteresis loops of YPr 2.4%. Inset: dependence of the magnetic field, at which the magnetization maximum corresponding to the fishtail appears ( $H_{\text{peak}}$ ), on the Pr content at  $T = 85 \text{ K}$ .

The constant value of the parameter  $n$  over a wide temperature range for YPr 2.4% crystal, see upper inset of Fig. 7.3.4, suggests that the pinning structure is more stable as compared to the one in Y123. More stable vortex pinning means it is less sensitive to changes of field in the region of the fishtail effect, i.e. where the increase of the pinning force is related

to the increase of the Pr content. The rapid increase of the  $n$ -value with increasing temperature suggests that thermally activated flux flow sets in at a temperature of 85 K. This occurs at a higher temperature than in the case of Y123, confirming stronger pinning due to the introduced Pr ions. The parameter  $\beta$  is not changed much as compared to 90K-Y123 crystal. A decrease of the parameter  $\alpha$  for higher Pr content suggests that the applied field affects the background pinning less for Y123 crystals with a higher Pr substitution.

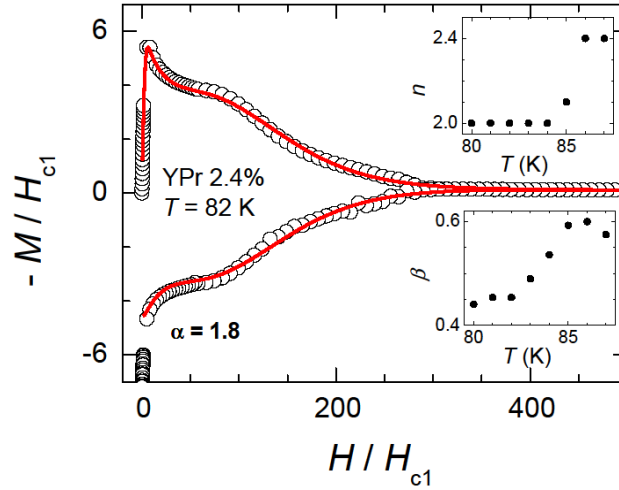


**Fig. 7.3.4.** Experimental magnetization (circles) and fitting procedure according to Eq. (7.3.1) (solid line) for YPr 2.4%. Upper and lower insets: temperature dependence of pinning parameters  $n$  and  $\beta$ , respectively.

Summary of the pinning force parameters  $\alpha$ ,  $\beta$ , and  $n$  is presented in Table 7.3.1.

**Table 7.3.1.** Values of the pinning parameters introduced in Eq. (7.3.1), with the relative pinning strength,  $\beta$ .

| Sample   | $\alpha$ | $\beta$  | $n$                                      | Comments  |
|----------|----------|--|--|---|
| 90K-Y123 | 2.5      | $T < 86$ K: increases;<br>$T \geq 86$ K: decreases | increases with<br>increasing temperature | Pinning due to twins in low fields<br>and due to oxygen vacancy in high<br>fields |
| YPr 1.3% | 2.2      | $T < 86$ K: increases;<br>$T \geq 86$ K: decreases | increases for $T > 84$ K                 | Pining due to oxygen vacancy and/or<br>twins in low fields and due to Pr ions     |
| YPr 2.4% | 1.8      | $T < 87$ K: increases;<br>$T \geq 87$ K: decreases | increases for $T > 85$ K                 | and oxygen vacancy in high fields   |

Influence of an increase of the Pr content on the background pinning, since the similar geometry of the measured crystals, may be due to a change in the self-fields. Obtained results suggest flux flow phenomenon for  $\text{Y}_{1-x}\text{Pr}_x\text{Ba}_2\text{Cu}_3\text{O}_{7-\delta}$ . Increase of the Pr content shifts the characteristic temperature of the flux flow activation to higher temperatures. The effect of the disorder landscape on the dynamics of a driven vortex system is captured by the macroscopic pinning force density  $F_{\text{pin}}$ . When  $F = F_{\text{pin}}$ , the vortices are “depinned” and start to move. The relative pinning strength,  $\beta = F_{\text{pin1}} / F_{\text{pin2}}$ , where pinning forces  $F_{\text{pin1}}$  and  $F_{\text{pin2}}$  correspond to the strength of the pinning at low fields and of the actual interaction of vortex matter with the pinning structure, respectively, corresponds to strengths of pinning due to defects with respect to the background, i.e. without defects, pinning.

The irreversibility lines and the field dependence of the critical current densities are presented in Figs 7.3.5 and 7.3.6. For the comparison, data for the nearly optimally doped crystal, i.e. with  $7-\delta \approx 6.92$ , YPr 0.8%, are presented. The irreversibility line in all crystals is consistent with  $H_{\text{irr}} \propto (1-T/T_c)^{3/2}$ . Overdoped crystals have higher values of the superconducting carrier density, i.e. lower penetration depth values, see Table 7.3.1, and higher  $H_c$  values, which leads to higher values of the irreversibility fields. For crystals with the same oxygen content, lack of change of the  $H_{\text{irr}}(T)$  for higher Pr substitution could be due to the constant anisotropy value. The irreversibility field was reported to scale with  $\gamma^{-2}s^{-1}$ , see Ref. [278]. This agrees with the fact that the  $c$ -axis parameter does not change upon Pr substitution indicating that the distance between neighbouring  $\text{CuO}_2$  planes remains constant.

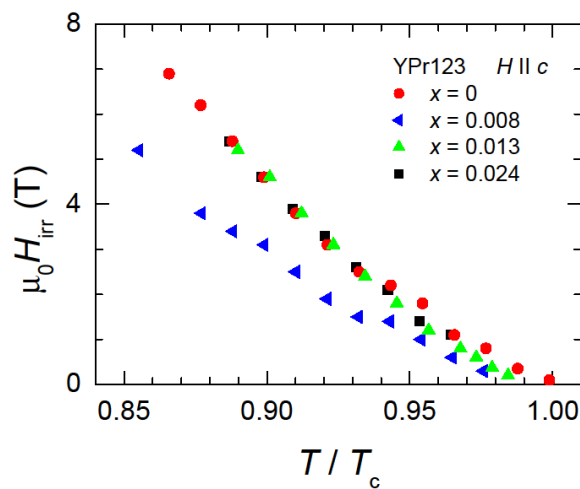
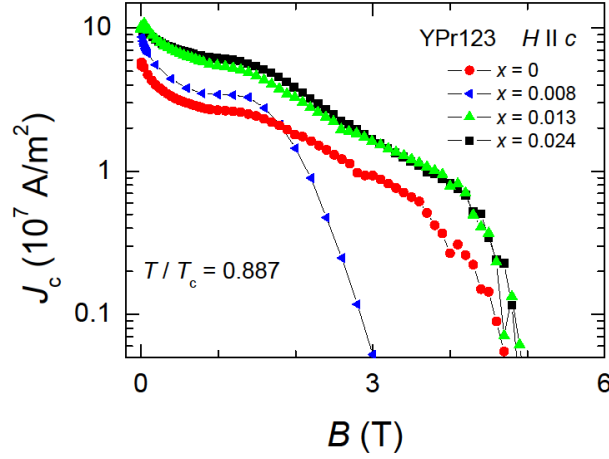
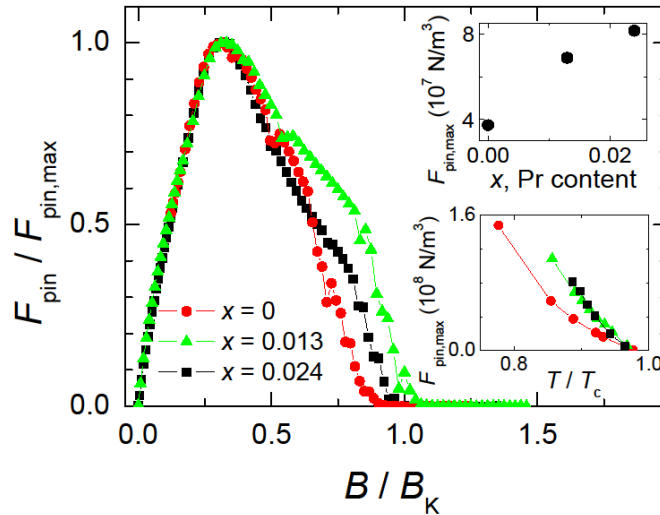


Fig. 7.3.5. Temperature dependence of the irreversibility fields.



**Fig. 7.3.6.** Field dependence of the critical current density at a reduced temperature of  $0.887T_c$ .

Field dependence of the maximum pinning force density is shown in Fig. 7.3.7. The value of  $F_{\text{pin,max}}$  increases in YPr123 as compared with 90K-Y123, see lower inset of Fig. 7.3.7, with no significant changes in  $T_c$ ,  $H_c$ , and  $\lambda$ . Pinning at high fields was suggested to be due to oxygen vacancies and Pr ions. The increase of the Pr content from 0 to 2.4% in Y123 doubles the maximum pinning force density (see upper inset of Fig. 7.3.7) with no effect on  $H_{\text{irr}}$  (Fig. 7.3.5).



**Fig. 7.3.7.** Normalized pinning force density for YPr123 with  $\delta \approx 0.03$  at  $T = 80$  K. Upper inset: increase of  $F_{\text{pin,max}}$  with increasing Pr substitution at  $T = 80$  K. Lower inset: temperature dependence of  $F_{\text{pin,max}}$ .

Despite the macroscopic increase of the pinning force density for higher Pr content in YPr123, it seems to be worth to analyze the local vortex pinning at the surface of the sample.

Therefore, Hall probe scanning was performed in a liquid nitrogen bath. First, crystals were cooled down and magnetized in external magnetic field of a strong permanent magnet NdFeB (the remnant magnetization exceeds 1 T). After removal of the magnetic field and relaxation delay of about 15 min, the remnant magnetization was scanned by a Hall probe.

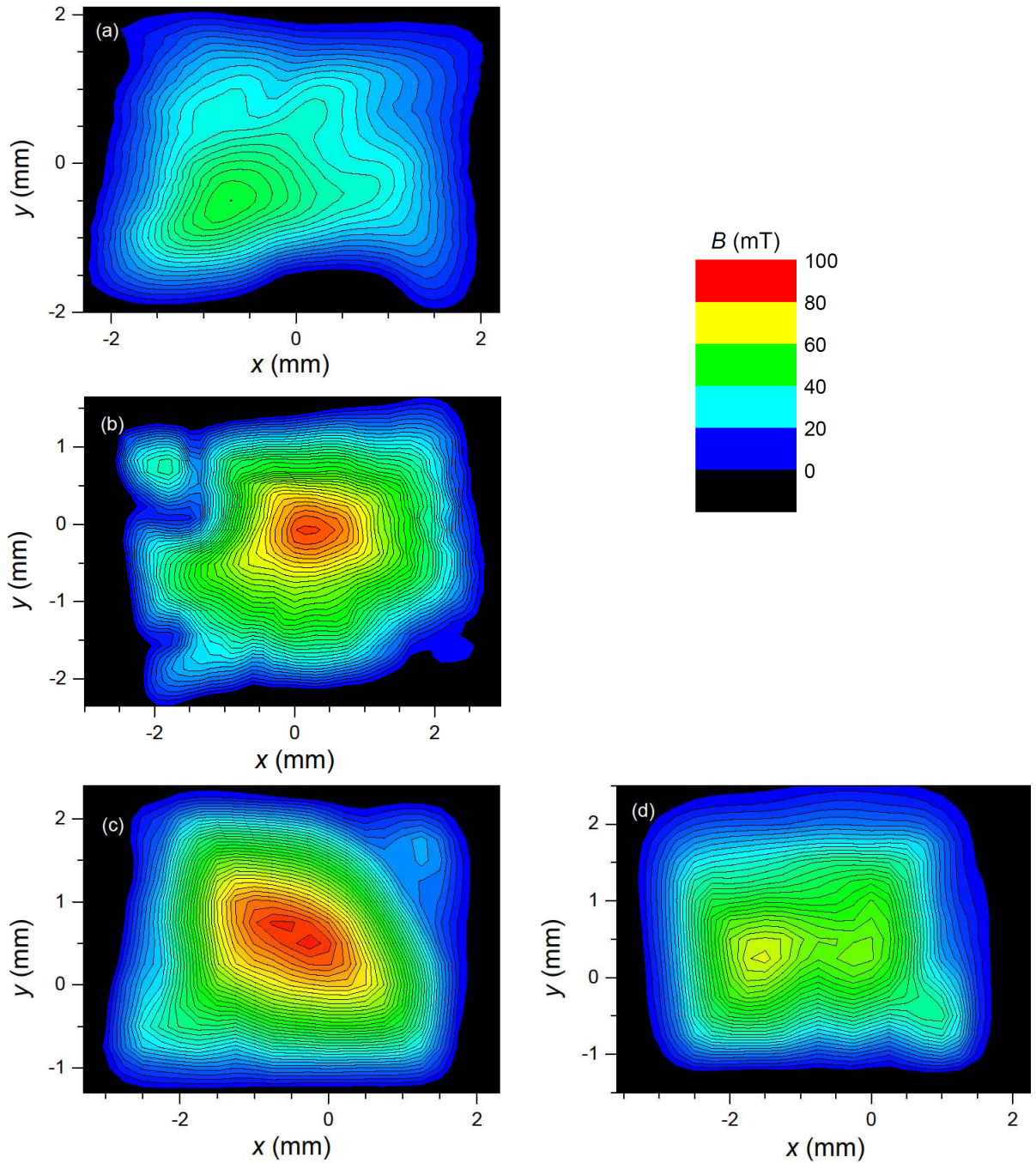


**Fig. 7.3.8.** Hall probe scanning of (a) 90K-Y123, (b) YPr 1.3%, (c) top side of YPr 2.4%, and (d) bottom side of YPr 2.4%. Scale is the same over all of the figures.



Field distribution in Hall scan profile maps, see Figs 7.3.8 and 7.3.9a, implies that the defects (oxygen deficiency, twin boundaries, and Pr ions) are distributed homogeneously within the sample. For YPr 2.4% crystal a difference between profiles at the top and at the bottom sides of the sample has been observed. It may indicate a difference in the distance from the seed crystal and an improvement/degradation of the crystals' quality during the crystals' growth. Praseodymium ions may not be equally distributed as a function of time during the growth process. Difference in the maximum trapped field,  $B_t$ , values between both crystal's sides is of 26%. Value of  $B_t$  increases for crystals with higher Pr content, see Fig. 7.3.9b, and was discussed in Ref. [277]. These results are consistent with the increase of the  $J_c(B)$  for crystals with higher substitution of Y by Pr in Y123. The maximum trapped field is 0.097 T, see Fig. 7.3.9b, which is due to small sample size. Much higher values of the trapped field than the ones reported here have been found for Gd123 and Sm123 superconducting bulks of 30 mm in diameter. For such bulks trapped fields of 0.88 T and 1.52 T were found, respectively [279].

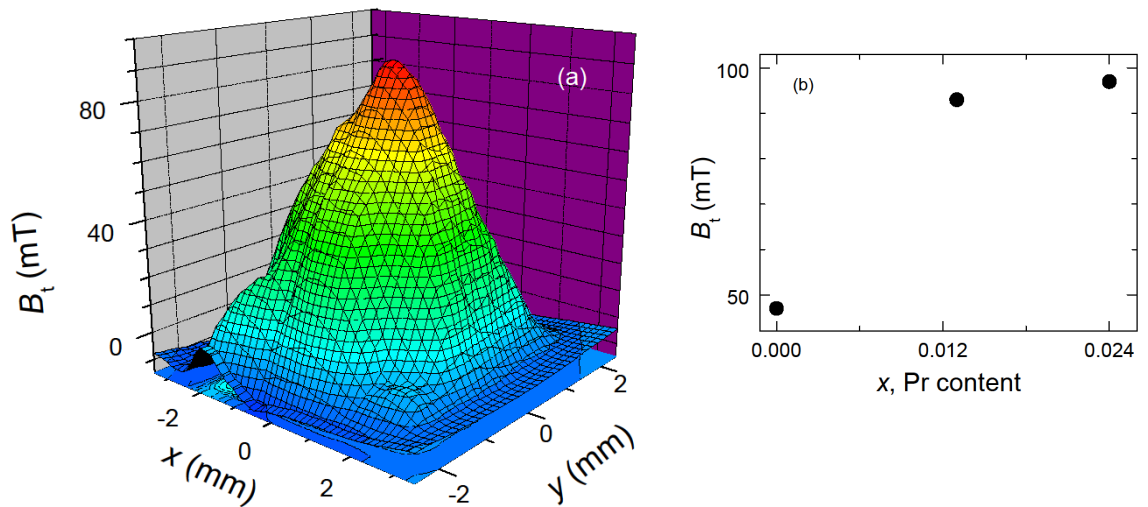


**Fig. 7.3.9.** (a) Trapped field profile of YPr 1.3% single crystal where  $x$  and  $y$  denote the scanning area; (b) increase of the maximum trapped field for crystals with higher Pr content.

#### 7.4. Influence of Pr ions on the intrinsic pinning

Intrinsic pinning is strongly pronounced for all crystals already at temperatures very close to  $T_c$ , as was extensively discussed in Ref. [272]. The angle of the torque maximum corresponding to the intrinsic pinning varies between  $90.5^\circ$  and  $91^\circ$ , depending on crystal, see Fig. 7.4.1.

All of the investigated YPr123 crystals are naturally twinned and additional complication due to this fact may occur in describing the angular torque dependence [95Z52]. However, it was shown [97] that for twinned crystals, additional temperature onset of intrinsic pinning occurs above the onset of twin-boundary pinning. Intrinsic pinning by the layered structure is dominant at temperatures close to  $T_c$ , whereas pinning by twin boundaries is dominant at slightly lower temperatures and is present only for vortices aligned with the twin boundaries [97].

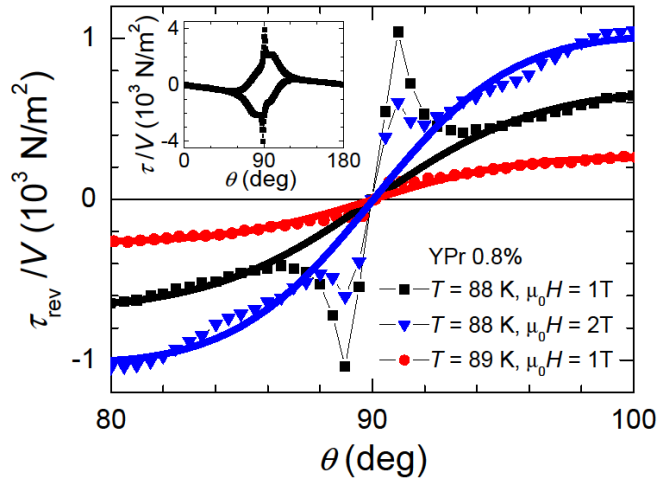


**Fig. 7.4.1.** Angular dependence of the reversible torque for YPr 0.8% obtained by averaging the irreversible torque dependence upon clockwise and counterclockwise rotating the sample, indicating deviations from the dependence according to Eq. (5.1.4) (represented by straight lines). Inset: example of the angular dependence of the irreversible torque with pronounced intrinsic pinning close to the  $ab$ -plane.

Torque (or magnetization) maximum at angles around  $90^\circ$  is often interpreted as evidence for a lock-in of vortex lines between the  $\text{CuO}_2$  planes. However, it is known that the lock-in transition occurs only at fields below  $H_{c1}^{\parallel c}$  [91,280]. The lock-in angle is of the order of  $H_{c1}^{\parallel c}/H$  and the transition is difficult to observe even at low fields [281]. Strong bulk pinning reduces the angle of the lock-in transition even further [282]. Nevertheless, intrinsic pinning is not negligible even at high temperatures. This is due to the fact that the vortex core energy modulation remains sizeable even very close to  $T_c$  and the total area of the core is  $\xi_c \cdot \xi_{ab}$ , [281] with  $\xi_c > s$  and  $\xi_{ab} > \lambda_L$  ( $\lambda_L$  is the Josephson length,  $\lambda_L \approx 5 \text{ nm}$  for Y123). Therefore, the only contribution to intrinsic pinning, relevant at temperature and field

range investigated here, is pinning of vortices by the kink structure. Hence, the angle of the torque maximum is marked as  $\theta_{\text{kink}}$ .

Following analysis of Kugel *et al.* [283], pinning in YPr123 crystals at angles  $\theta \leq \theta_{\text{kink}}$  is probably associated with 2D (intrinsic) pinning, whereas with 3D (bulk) pinning occurs at angles  $\theta > \theta_{\text{kink}}$ . Influence of the Pr content on the intrinsic pinning was studied, see Fig. 7.4.2.

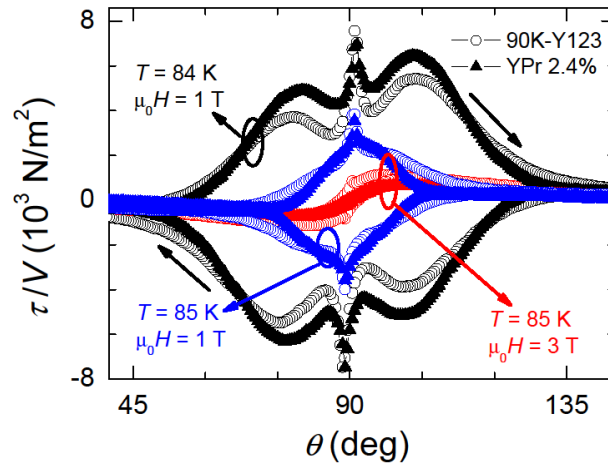


**Fig. 7.4.2.** Angular dependence of the irreversible torque for two crystals with the same oxygen content; open symbols: 90K-Y123, full symbols: YPr 2.4%. The torque maxima corresponding to intrinsic pinning at  $\theta \approx 90^\circ$  are clearly visible.

A larger irreversibility of the torque is evidenced at lower temperature for the Pr-doped crystal than for the pure Y123 crystal. At the same time the angular range, where vortex pinning is efficient for YPr 2.4% is narrower than that for 90K-Y123. Intrinsic pinning seems to be stronger in 90K-Y123 than in YPr 2.4% since the maximum in the latter, corresponding to vortex pinning by kinks, diminishes faster with increasing field. Vortex lattice changes from kinked to tilted for higher fields. Reduction of the torque maximum for YPr123, as compared to Y123, suggests that kinks can be traced up to higher fields in Y123. This is probably related to a higher rate of nucleation of kinks at the defect sites as a result of Pr substitution in YPr 2.4%. The part of the kink structure parallel to the  $c$ -axis, pinned by defects located in the planes, may be the reason for the increase of the critical current at higher Pr concentration as reported in [276]. Then, the critical current density due to trapping of perpendicular to the planes part of the kink structure saturates faster [284] for YPr 2.4% than for pure Y123. This is probably related to the observed [276] shift of the magnetic field,

at which the magnetization maximum corresponding to the fishtail effect appears, to lower fields with increasing Pr content in YPr123.

### **7.5. Brief summary of low level Pr substitution in $\text{YBa}_2\text{Cu}_3\text{O}_{7-\delta}$**

Influence of the Pr ions on the superconducting state properties of  $\text{Y}_{1-x}\text{Pr}_x\text{Ba}_2\text{Cu}_3\text{O}_{7-\delta}$  (YPr123) single crystals with  $x = 0, 0.008, 0.013,$  and  $0.024$  was investigated by SQUID and torque magnetometry as well as using Hall probe scanning technique. Superconducting state parameters in Pr-doped  $\text{YBa}_2\text{Cu}_3\text{O}_{7-\delta}$  crystals were derived and related to the vortex pinning and critical current characteristics. For crystals with similar types of defects, the shift of the irreversibility line to higher fields and higher temperatures is mainly due to the change in the intrinsic parameters. Higher temperatures of flux flow activation for crystals with higher Pr-content was revealed. The introduction of small amounts of Pr strengthens pinning most effectively at moderate and/or high fields. The observed increase of the trapped field is consistent with the observed increase of the critical current density for crystals with higher Pr content.

The averaged superconducting state anisotropy was evaluated to be 7.4. It is independent on the Pr content or on the temperature and field. Intrinsic pinning was observed in all crystals via a pronounced peak of the irreversible torque signal, when the magnetic field deviates by  $0.5 - 1^\circ$  from the direction parallel to the  $ab$ -plane. The peak in the torque was attributed to the kinked state of vortices. The intrinsic pinning is stronger in pure Y123 than in YPr 2.4%, probably due to a higher nucleation rate of kinks at the defects in the Pr-doped crystal.



## 8. Rare earth substitutions into Y position in $\text{YBa}_2\text{Cu}_3\text{O}_{7-\delta}$ : experimental results and discussion

Since high temperature superconductors were discovered much effort has been made to improve the superconducting properties for engineering applications such as magnetic bearings, flywheels, magnetic separation, etc. [285,286,287]. Magnets with windings made of Y123 are already capable of producing magnetic field of 30 T [288]. Understanding the pinning mechanisms would be beneficial for delivering industrially-available even more functional materials where the highest  $T_c$ ,  $H_{irr}$ , and  $H_{c2}$  are of great importance. Compared to Y123, the (Nd,Sm)123 superconductors attract significant attention because of their higher superconducting transition temperature and higher critical current density, especially in medium magnetic fields [289,290].

It is difficult to fully eliminate the (Nd,Sm)-Ba substitutions and such substitutions may lead [291] to formation of stripes, i.e. magnetic charge modulations. The origin of stripes is due to inhomogeneous distribution of the charge carriers in  $\text{CuO}_2$  layers of HTSC [292] during the doping process [293]. Such distribution has been predicted theoretically [294,295,296,297,298,299]. Also mounting experimental evidence exists for microscopic charge inhomogeneities in cuprate alloys [292,300,301,302,303,304,305,306], including Y123 system [307], but stripes were observed only for materials with specific hole doping rates. Stripes are suspected to be the source of the peak effect [308]. Stripe pattern in  $\text{LRE}_{1+y}\text{Ba}_{2-y}\text{Cu}_3\text{O}_{7-\delta}$  has been reported in the literature on atomic force and scanning tunnelling microscope investigations [291,308,309]. However, none of such investigations were performed in course of this thesis and it would be highly speculative to suggest that stripes may form in the investigated (Nd,Sm)123 superconductors.

In this Section, the influence of various ions substitutions on the superconducting state parameters of  $\text{REBa}_2\text{Cu}_3\text{O}_{7-\delta}$  is discussed. Vortex pinning properties for optimally oxygenated crystals of Y123, Nd123, and Sm123 were investigated applying SQUID magnetometry. In several passages, comparison between optimally oxygenated and overdoped Y123 crystals, i.e. 92K-Y123 and 90K-Y123, is presented.

### 8.1. Single crystals of $\text{REBa}_2\text{Cu}_3\text{O}_{7-\delta}$

Single crystals of Y123 and  $(\text{Nd,Sm})_{1+y}\text{Ba}_{2-y}\text{Cu}_3\text{O}_{7-\delta}$ , i.e. (Nd,Sm)123, solid solutions [310,311] were grown by TSSG method in air. Crystals were annealed in flowing oxygen at temperature of 500 °C for 72 hours in the case of Y123 and at temperature of 350 °C for 200 hours in the case of (Nd,Sm)123. Normal pressure of the oxygen gas was applied. Cooling conditions, as introduced in Section 7.1, are presented in Table 8.1.1.

**Table 8.1.1.** Abbreviations for the investigated crystals, the crystals' size, and conditions for oxygenation.

| Sample   | Symbol   | $x, y, z$ (mm)   | Oxygenation temperature (°C) | Cooling |
|--|----------|------------------|------------------------------|---------|
| $\text{YBa}_2\text{Cu}_3\text{O}_{7-\delta}$                   | 92K-Y123 | 1.96, 1.92, 1.24 | 500                          | furnace |
| $\text{Nd}_{1+y}\text{Ba}_{2-y}\text{Cu}_3\text{O}_{7-\delta}$ | Nd123    | 3.17, 0.98, 0.66 | 350                          | slow    |
| $\text{Sm}_{1+y}\text{Ba}_{2-y}\text{Cu}_3\text{O}_{7-\delta}$ | Sm123    | 3.50, 2.90, 1.45 | 350                          | slow    |

The oxygen content in Y123 was calculated assuming linear dependence of the lattice constant on  $7 - \delta$ , as proposed by Kruger *et al.* [154], see Table 8.1.2. Only the  $c$ -axis parameter was taken into account due to structural twinning, see Eq. (4.2.2).

As already mentioned, complete elimination of (Nd,Sm)-Ba substitutions is very challenging task. Rare earth ions like Sm and Nd substituting for Ba cations in the (Nd,Sm)123 structure lead to higher than 7 oxygen content, which increases with increasing the  $(\text{Sm,Nd})_{1+y}\text{Ba}_{2-y}$  substitution level [312]. The substitution limit of Sm at the Ba sites is remarkably smaller than that of Nd at a high temperature [313]. Estimation of the oxygen content from the lattice constants for the measured crystals assuming  $y = 0$  corresponds to  $\delta = 0.45$  and  $\delta = 0.37$  for Nd123 [314] and Sm123 [315], respectively. Vanishing of  $T_c$  at orthorhombic-to-tetragonal transition at  $\delta = 0.45$  for Nd123 was claimed to be an inherent property of pure (nonsubstituted) system [314]. Orthorhombic-to-tetragonal transition occurs at  $\delta = 0.4$  for nonsubstituted Sm123 [315]. Those results are in contradiction with high  $T_c$  observed in measured crystals which is evidence for increased rare earth ion occupancy in (Nd,Sm)123. An increase of Sm occupancy up to 1.05 and of Nd occupancy up to 1.1 was derived for Sm123 [316] and Nd123 [317], respectively. It is believed that

formation of  $(\text{Nd,Sm})_{1+y}\text{Ba}_{2-y}\text{Cu}_3\text{O}_{7-\delta}$  type solid solution occurs, as it is given in Table 8.1.2, thus creating additional pinning centres which will be discussed in more detail in Section 8.4.

In order to determine the exact chemical substitution level in  $(\text{Nd,Sm})_{123}$  crystals, accurate analytical methods are needed. Spectrometric analysis methods, e.g. ICP atomic emission spectrometry, atomic absorption spectrometry, spectrophotometry, XRD or electron spectrometric techniques are most common methods of choice applied to characterize such materials. Chemical methods include titrimetry, coulometry or gravimetry. These accurate analytical methods are suitable e.g. for testing the stoichiometric correctness of initial samples, determination of the phase composition and the homogeneity range of different phases, and identification of secondary phases of the material, see Ref. [318] and references therein. Although it may seem necessary, none of the above analytical methods were successfully used (atomic emission spectrometry was applied, although led to unreliable results) to determine the exact stoichiometric composition in  $(\text{Nd,Sm})_{123}$ . Thus, only a rough estimation of the composition, based on lattice constant investigated by the XRD-analysis, was made.

**Table 8.1.2.** Abbreviations for the investigated crystals, their lattice constants, critical temperature, the superconducting-to-normal state transition width, oxygen content, and the rare earth occupancy in  $(\text{Nd,Sm})_{1+y}\text{Ba}_{2-y}\text{Cu}_3\text{O}_{7-\delta}$ .

| Symbol   | $a, b, c$ (nm)            | $T_c$ (K) | $\Delta T_c$ (K) | $7-\delta$        | $y$               |
|----------|---------------------------|-----------|------------------|-------------------|-------------------|
| 92K-Y123 | 0.38197, 0.38886, 1.16925 | 92.6      | 0.51             | 6.92 <sup>a</sup> | -                 |
| Nd123    | 0.39028, 0.39026, 1.18140 | 93.5      | 3.79             | 7.05 <sup>b</sup> | 0.10 <sup>b</sup> |
| Sm123    | 0.38944, 0.39077, 1.18295 | 91.6      | 2.16             | 7.10 <sup>c</sup> | 0.05 <sup>c</sup> |

<sup>a</sup> According to [154]

<sup>b</sup> According to [317,319], analysis for  $\text{Nd}_{1+y}\text{Ba}_{2-y}\text{Cu}_3\text{O}_{7-\delta}$ ,  $y \geq 0$

<sup>c</sup> According to [316], analysis for  $\text{Sm}_{1+y}\text{Ba}_{2-y}\text{Cu}_3\text{O}_{7-\delta}$ ,  $y \geq 0$

All crystals studied in this Section are naturally twinned. A typical example of the sample surface, obtained by polarized light microscopy, is shown in Fig. 8.1.1.



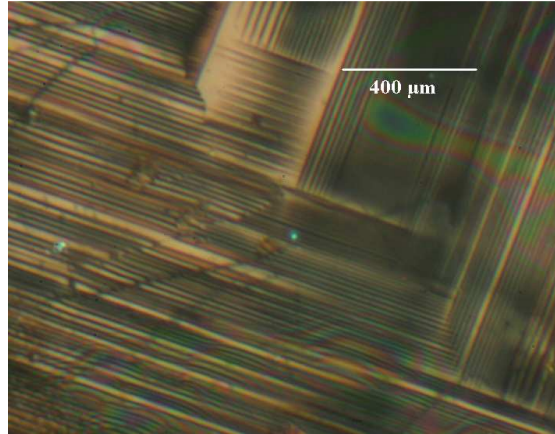


**Fig. 8.1.1.** Naturally twinned structure in the  $ab$ -plane of Sm123.

## 8.2. Influence of rare earth ions on the intrinsic properties of $\text{REBa}_2\text{Cu}_3\text{O}_{7-\delta}$

The superconducting-to-normal state transition of the three optimally oxygenated crystals was investigated by SQUID magnetometry using DC mode and is presented in Fig. 8.2.1. The broad transition in the case of (Sm,Nd)123 crystals has been attributed to the presence of the LRE-Ba substitutions, as mentioned in Sections 4.4 and 8.1.

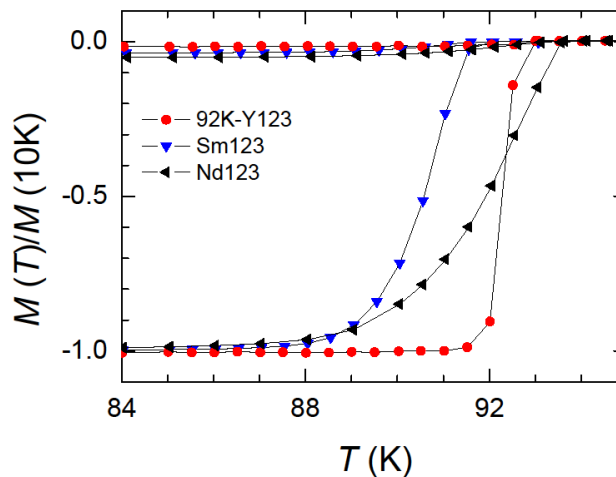


**Fig. 8.2.1.** Normalized temperature dependence of the magnetization for the optimally oxygenated RE123 single crystals.

The superconducting state parameters were derived from magnetization measurements and applying effective media approach and are presented in Table 8.2.1. Measurements of  $M(H)$  were performed applying SQUID magnetometry for  $H \parallel c$ -axis and for  $H \parallel ab$ -plane. The highest values of the upper critical fields were found for Sm123 which, despite the lowest

value of  $T_c$  among crystals investigated in this Section, is characterized by the steepest slope of  $dH_{c2}/dT$ . The Sm123 crystal is also characterized by the largest thermodynamic critical field and the largest GL parameter, see Table 8.2.1.

After reducing the oxygen content from 6.97 (which corresponds to over-oxygenated Y123 crystal with  $T_c = 90.1$  K) to 6.92 (optimally oxygenated Y123 crystal with  $T_c = 92.6$  K), values of  $T_c$ ,  $\mu_0 H_{c2}^{\parallel c}(0)$ , and the GL parameter increase by 2.5 K, 17 T, and 9, respectively. Simultaneously, decrease of  $\mu_0 H_{c1}^{\parallel c}(0)$  and  $\mu_0 H_c(0)$  by 15 mT and 0.2 T was observed, respectively. The increase of  $T_c$  with increasing carrier concentration is due to the specific phase diagram of  $T_c(\delta)$ , as presented in Fig. 4.1 and discussed in Section 4.3. For 90K-Y123, the concentration of the superconducting charge carriers is higher than for 92K-Y123. This leads to higher values of the thermodynamic critical field, lower penetration depth, and higher values of  $H_{c1}$  in the overdoped 90K-Y123. These implications can be related to the vortex pinning properties, which will be discussed in the next Section.

**Table 8.2.1.** Samples  $T_c$  values, coherence length, penetration depth, Ginzburg-Landau parameter, thermodynamic critical field, slope  $dH_{c2}/dT$ , upper critical field, and lower critical field for the investigated crystals.

| Sample   | $T_c$ (K) | $\xi_{ab}(0)$<br>(nm) | $\lambda_{ab}(0)$<br>(nm) | $\kappa^{\parallel c}$ <sup>a</sup> | $\mu_0 H_c(0)$<br>(T) | $\mu_0 dH_{c2}^{\parallel c}/dT$<br>(T/K) | $\mu_0 H_{c2}^{\parallel c}(0)$<br>(T) <sup>b</sup> | $\mu_0 H_{c1}^{\parallel c}(0)$<br>(mT) |
|----------|-----------|-----------------------|---------------------------|-------------------------------------|-----------------------|---|---|---|
| 92K-Y123 | 92.6      | 1.57                  | 96.2                      | 58                                  | 1.17                  | -2.00                                     | 134.4   | 81                                      |
| Nd123    | 93.5      | 1.53                  | 112.9                     | 70                                  | 1.13                  | -2.08                                     | 141.2   | 61                                      |
| Sm123    | 91.6      | 1.32                  | 104.8                     | 75                                  | 1.20                  | -2.83                                     | 188.1   | 72                                      |

<sup>a</sup> Determined from the numerical solution for the Ginzburg-Landau equation

<sup>b</sup> Assuming clean limit and WHH dependence [WHH]

The anisotropy parameter in optimally doped RE123 single crystals is around 5-10 [270,271], i.e. much smaller than in underdoped crystals. The small anisotropy implicates that the exact value of  $\gamma$  is less sensitive to the crystal's orientation for  $H$  along the  $ab$ -plane. Additionally, contribution of paramagnetic background in magnetization  $M(H)$  measurements could be well separated from superconducting signal (which was not the case of underdoped SmBa<sub>2</sub>Cu<sub>3</sub>O<sub>x</sub>). Therefore, it was possible to estimate the anisotropy parameter in optimally doped RE123 based solely on magnetization measurements. Anisotropy parameter was determined from the ratio between two slopes of  $dM_{rev}/dH$ , see Eq. (2.1.4) and Eq. (2.1.5) for

magnetic field  $H \parallel c$ -axis and  $H \parallel ab$ -plane with  $\lambda_a = \lambda_b = \lambda_{ab}$ . In none of the optimally oxygenated RE123 a temperature dependence of  $\gamma$  was found, nevertheless, only a narrow temperature range was investigated. As previously in Section 7.2, no data on the in-plane anisotropy are presented here due to the crystals' twinning. For the optimally doped Y123, anisotropy parameter of 6.1 was found, see Fig. 8.2.2, which is consistent with the value reported in literature and comparable to the anisotropy parameter determined from magnetization measurements for 90K-Y123 [271]. The general property of Y123 system is that the anisotropy parameter decreases for crystals with higher oxygen content [271]. Nevertheless, no such property was observed for  $\gamma$  values obtained from magnetization measurements. This can be due to comparison of anisotropy parameters obtained from the magnetization and not torque measurements, where the latter technique provides a more reliable anisotropy data, see Section 7.2.

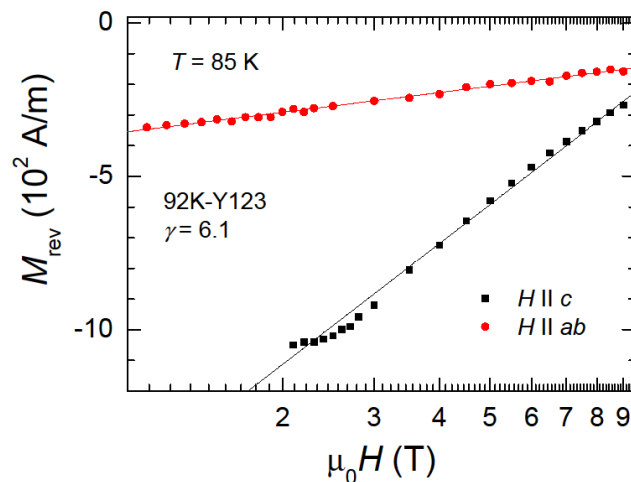


**Fig. 8.2.2.** Field dependence for the reversible magnetization used for determination of the anisotropy parameter. Lines are the linear fits of Eq. (2.1.4) and Eq. (2.1.5) to the reversible magnetization for  $H \parallel c$ -axis and for  $H \parallel ab$ -plane, respectively.

The anisotropy parameter of Sm123, determined from the reversible part of magnetization, is around 10, see Fig. 8.2.3. Substitution of Sm in the place of Y in Y123 leads to an increase of the anisotropy parameter by 62 % which has been attributed to larger ionic radius of Sm, equal to 0.096 nm, as compared to radius 0.090 nm for Y [156] and larger  $c$ -axis lattice constant in case of Sm123, see Table 8.1.2. The increase of the distance between superconducting  $\text{CuO}_2$  planes promotes the Josephson coupling between superconducting layers [320]. Josephson coupling acts similarly to normal state tunnelling and therefore it's

characteristics depend exponentially on the distance between neighbouring  $\text{CuO}_2$  planes. The 0.7 % change in the  $c$ -axis parameter leads to a 62 % increase of the anisotropy parameter, in agreement with result reported in Ref. [321].

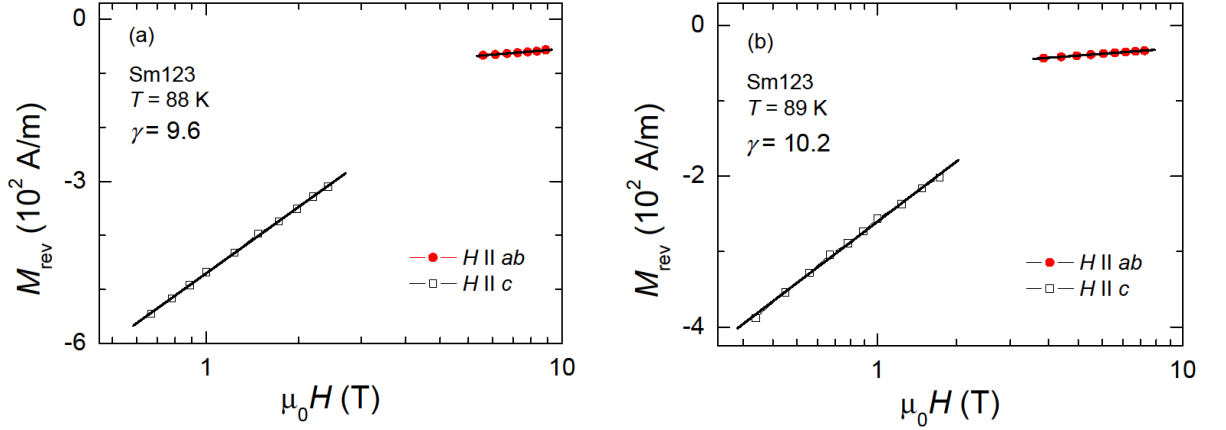


**Fig. 8.2.3.** Field dependence for the reversible magnetization of Sm123 at (a)  $T = 88$  K and (b)  $T = 89$  K. Lines are the linear fits of Eq. (2.1.4) and Eq. (2.1.5) to the magnetization for  $H \parallel c$ -axis and  $H \parallel ab$ -plane, respectively.

### 8.3. Influence of rare earth ions on the extrinsic properties of $\text{REBa}_2\text{Cu}_3\text{O}_{7-\delta}$

The analysis of vortex pinning was performed using numerical algorithm for  $B_{\text{eq}}(H)$  and with  $J_c(B)$  relation, as introduced in Section 7.3.

In  $\text{YBa}_2\text{Cu}_3\text{O}_{7-\delta}$  crystal with  $T_c = 92.6$  K, the measurements in temperature range 50 K – 90 K reveal a small fishtail effect at temperatures  $T \leq 70$  K. The analysis of the pinning force density, see inset of Fig. 8.3.1, suggests that more than one kind of defect is present in the low fields region. On the other hand, in the high-field region, where only large defects remain active, the normalized pinning force density scales very well with temperature. The transition to the superconducting state was sharp and no strong pinning centres like oxygen clusters are apparent. These observations together with the high  $T_c$  value suggest that either oxygen vacancies or twin boundaries act as pinning sites in this crystal.

Field dependent vortex pinning (large  $n$  parameter) and a small influence of the applied field on background pinning (small value of  $\alpha$ ), was found for 92K-Y123, see Fig. 8.3.2. The non-linear temperature dependence of the parameter  $\beta$  results from different temperature dependences of both critical current components. Among all of single crystals investigated, the parameter  $\beta$  is the smallest in the case of 92K-Y123, which indicates

the weakest interaction of vortex matter with the pinning structure as compared to background pinning. Values of these parameters indicate that existing defects become too weak to sustain pinning of vortex lines at  $T \geq 85$  K and depinning may occur (see both insets of Fig. 8.3.2).

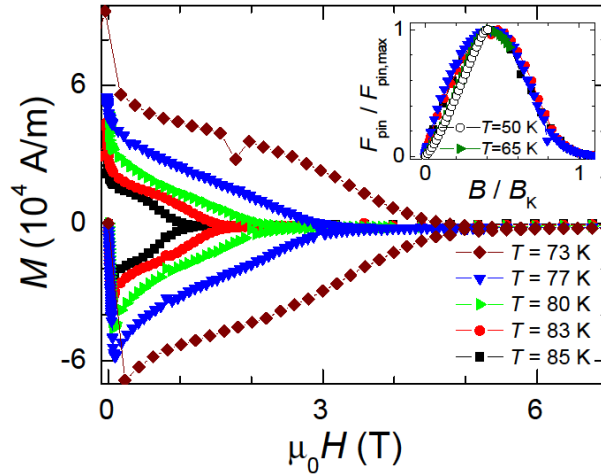


**Fig. 8.3.1.** Hysteresis loops measured for 92K-Y123. Inset: normalized pinning force density at 50, 65, 77, 83, and 85 K.

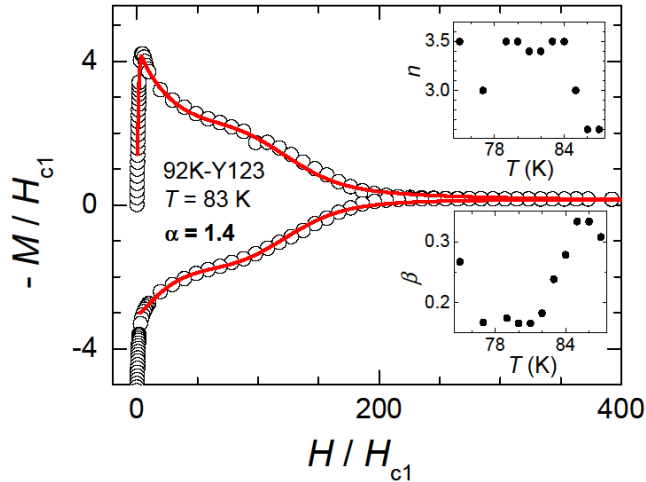


**Fig. 8.3.2.** Experimental results of magnetization measurements (circles) and fitting procedure according (solid line) to Eq. (7.3.1) for 92K-Y123. Upper and lower insets: temperature dependence of pinning parameters  $n$  and  $\beta$ , respectively.

Sm123 single crystals were investigated in temperature range 75 K - 90 K. For  $T < 88$  K, a pronounced fishtail effect was observed and its maximum shifts to higher fields for lower temperatures, see Fig. 8.3.3. All the curves of the field dependence of the normalized pinning force density collapse to a single curve, which implies that in this crystal pinning on only one kind of defects is present, see inset of Fig. 8.3.3.

Pinning parameters were determined using the “fitting procedure” with logarithmic pinning potential and are presented on Fig. 8.3.4. Small value of the parameter  $n$  indicates that pinning sites are active in broad range of fields. Temperature independence of the above parameter implies that pinning on those sites is also stable in a broad range of temperatures. Background pinning, here  $\alpha = 1.6$ , decays relatively fast with applied field, in comparison to that one for other crystals. The parameter  $\beta$  decreases at temperatures above 80 K, which suggests that the interaction of vortex matter with the pinning structure weakens, most probably due to thermal fluctuations, see inset of Fig. 8.3.4.

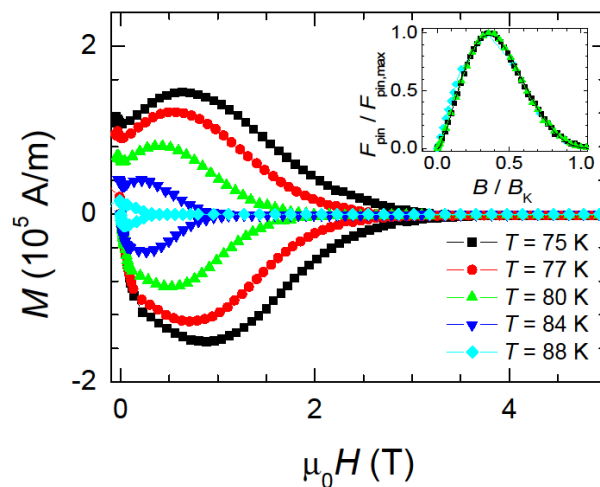


**Fig. 8.3.3.** Selected hysteresis loops for Sm123. Inset: normalized pinning force for temperatures 75, 80, and 88 K only (for clarity).

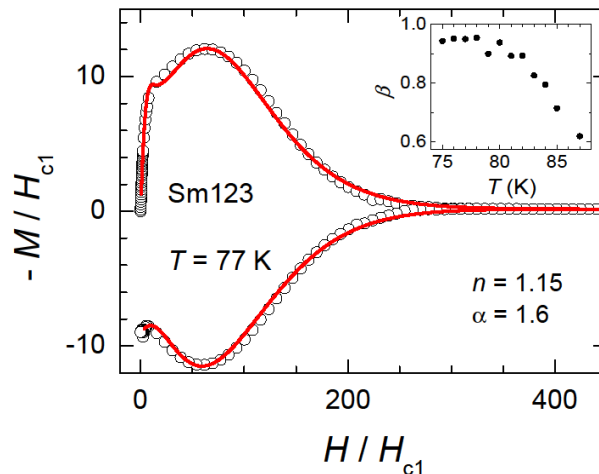


**Fig. 8.3.4.** Experimentally obtained magnetization scaled by  $H_{c1}$  (circles) and fitting procedure according to Eq. (7.3.1) (solid line) for Sm123. Inset: temperature dependence of  $\beta$ .

Properties of Nd123 single crystal were investigated in temperature range 30 K - 90 K. Fishtail effect is very pronounced, see Fig. 8.3.5, and visible in all investigated temperatures. The shift of the PE to higher fields was observed for lower temperatures. Pinning force density analysis, shown in the inset of Fig. 8.3.5, reveals presence of only one pinning mechanism, even at the lowest temperatures.

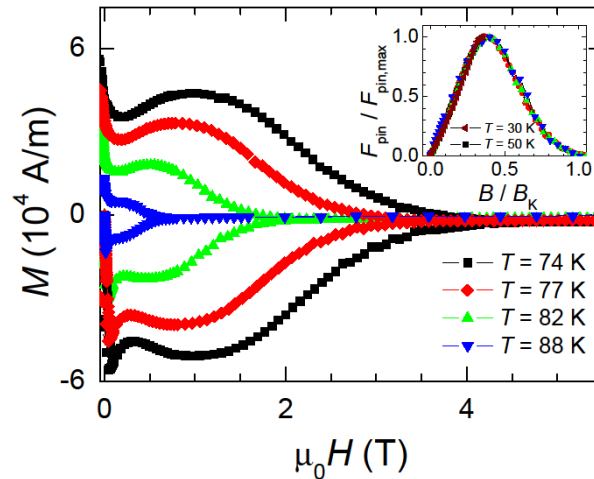


**Fig. 8.3.5.** Selected hysteresis loops for Nd123. Inset: normalized pinning force for temperatures 30, 50, 77, 82, and 88 K only (for clarity).

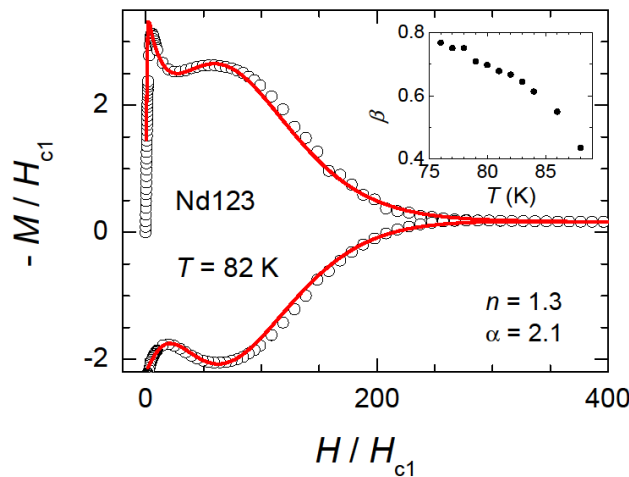


**Fig. 8.3.6.** Experimental magnetization (circles) and fitting procedure according to Eq. (7.3.1) (solid line) for Nd123. Inset: temperature dependence of  $\beta$ .

Small and temperature independent value of the parameter  $n$  suggests that pinning is effective in a broad range of fields and is unaffected by variation of temperatures. Background pinning diminishes fast for higher fields ( $\alpha = 2.1$ ). The parameter  $\beta$  decreases with increasing

temperature, which indicates that the interaction of vortex matter with pinning structure weakens for higher temperatures, see inset of Fig. 8.3.6.

Summary of the pinning force parameters  $\alpha$ ,  $\beta$ , and  $n$ , introduced in Eq. (7.3.1), is presented in Table 8.3.1.

**Table 8.3.1.** Parameters values for the pinning force density, Eq. (7.3.1) with the relative pinning strength,  $\beta$ .

| Sample   | $\alpha$ | $\beta$                          | $n$                               | Comments                               |
|----------|----------|----------------------------------|-----------------------------------|--|
| 92K-Y123 | 1.4      | non continuous behaviour (small) | non continuous behaviour ( $>3$ ) | Pinning due to oxygen vacancy or twins |
| Nd123    | 2.1      | decreases with increasing        | 1.2                               | Pinning due LRE-Ba substitutions       |
| Sm123    | 1.6      | temperature (large)              | 1.1                               |  |

Large value of the parameter  $n$  for 92K-Y123 indicates that vortex pinning is strongly field-dependent. Pinning centres are effective in a broad range of magnetic fields in the case of (Nd,Sm)123. Additionally, a constant value of  $n$  is due to a minimal effect of increasing temperature on the vortex pinning. The (Nd,Sm)-Ba substitutions, where such pinning centres may be of varying size, may be responsible for the small  $n$  value and the PE, see Section 6.3.4. The relative pinning strength, that corresponds to pinning due to defects with respect to the background pinning, diminishes for higher temperature for (Nd,Sm)123. This is due to weaker, although stronger in comparison to Y123, interaction between the vortex matter and the pinning structure in (Nd,Sm)123 when temperature approaches  $T_c$ .

Comparison of the irreversibility lines, upper critical fields and the peak fields for optimally oxygenated RE123 single crystals are summarized in Figs 8.3.7, 8.3.8, 8.3.9, and 8.3.10. Additionally, results for Y123 with the oxygen content higher than optimal, i.e. for 90K-Y123, are presented for comparison. The temperature dependence of the maximum pinning force density is shown in Fig. 8.3.8. The highest, with respect to the temperature and magnetic field, irreversibility line in 90K-Y123 corresponds to the lowest pinning force density in that compound. Correspondingly, (Sm,Nd)123 compounds are characterized by the lowest irreversibility line and the highest pinning force density with respect to the temperature, see Fig. 8.3.8. The irreversibility line observed for all crystals is consistent with  $H_{\text{irr}} \propto (1-T/T_c)^{3/2}$ . The low irreversibility fields are related to the low superconducting



carrier density and the low thermodynamic critical field, see Table 8.2.1. Overdoped crystal, i.e. 90K-Y123, have higher value of  $n_s$ , i.e. lower penetration depth, see Table 7.2.1, and higher  $H_c$ , which leads to the higher values of the irreversibility field. Due to the decrease of oxygen vacancies, a decrease of  $F_{\text{pin,max}}$  is observed, see Fig. 8.3.8. Since the maximum pinning force density is mainly due to pinning at fields close to  $H_{\text{peak}}$ , pinning in (Sm,Nd)123 is mostly effective in intermediate fields, whereas the strongest pinning centres (effective in high fields) are present in 90K-Y123. For the Y123 single crystal with  $T_c = 92.6$  K, i.e. optimally oxygenated, a relatively high critical current density is found for fields below  $H_{\text{peak}}$  (compared to 90K-Y123). Due to the decrease of oxygen vacancies, a decrease of  $J_c$  is observed in 90K-Y123, but only for low fields. Pinning centres in 90K-Y123 are the most effective in high fields.

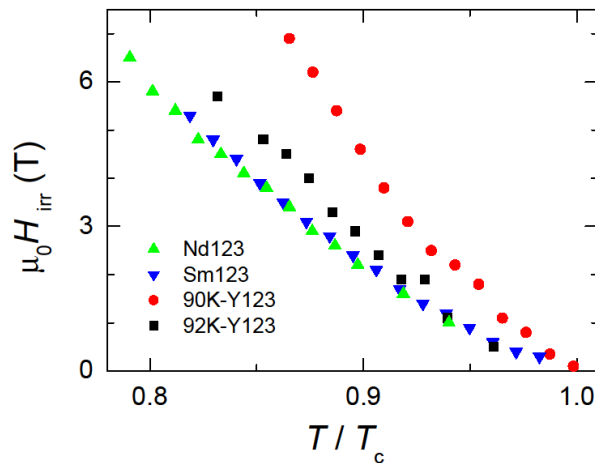


**Fig. 8.3.7.** Temperature dependence of the irreversibility line for Nd123, Sm123, 90K-Y123, and 92K-Y123.

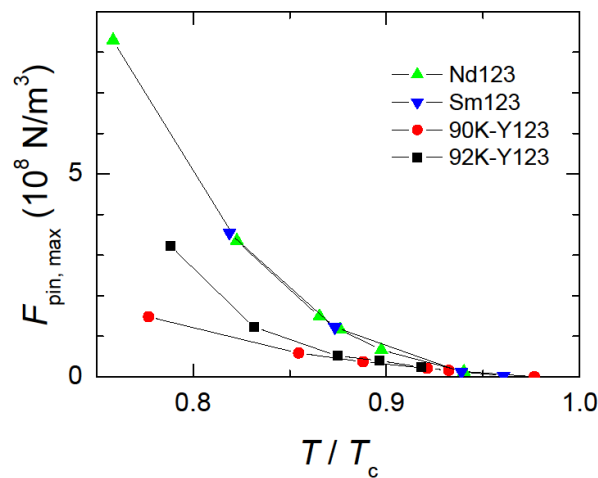


**Fig. 8.3.8.** Temperature dependence of the pinning force density for Nd123, Sm123, 90K-Y123, and 92K-Y123.

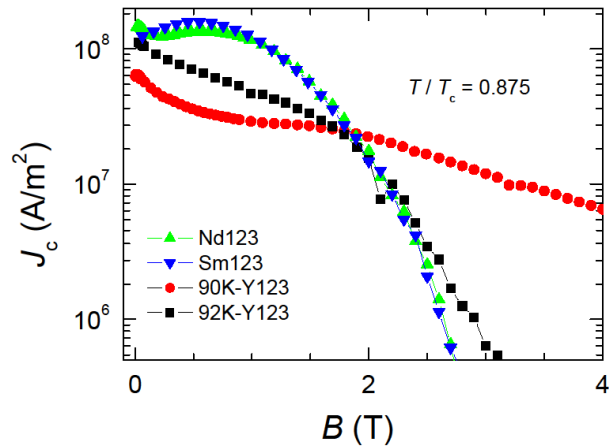


**Fig. 8.3.9.** Field dependence of the critical current density at reduced temperature for Nd123, Sm123, 90K-Y123, and 92K-Y123.

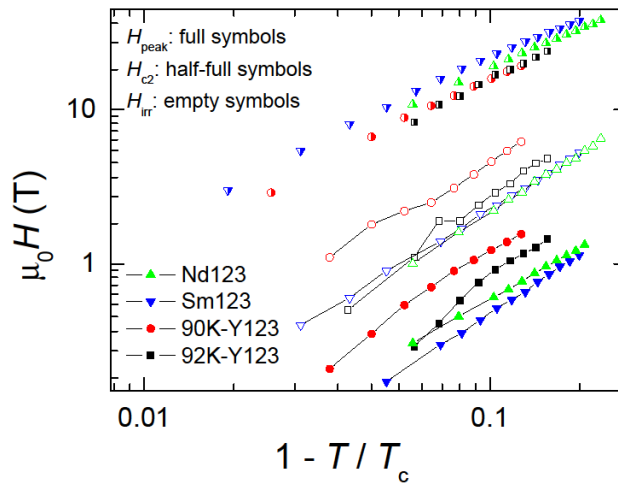


**Fig. 8.3.10.** Temperature dependence of the irreversibility line, upper critical field and the  $H_{\text{peak}}$  for Nd123, Sm123, 92K-Y123, and 90K-Y123.

An interesting property was observed for Nd123 and Sm123, where the pinning force density scales very well for all the investigated temperatures, see insets of Figs 8.3.3 and 8.3.5. Additionally, normalized dependence of the pinning force density is identical for Sm123 and Nd123 crystals, see Fig. 8.3.11. This indicates that the same pinning mechanism is present in both crystals. Moreover, this mechanism is temperature independent. This suggests that pinning centres in (Nd,Sm)123 are of the same origin and they are probably (Nd,Sm)-Ba substitutions.

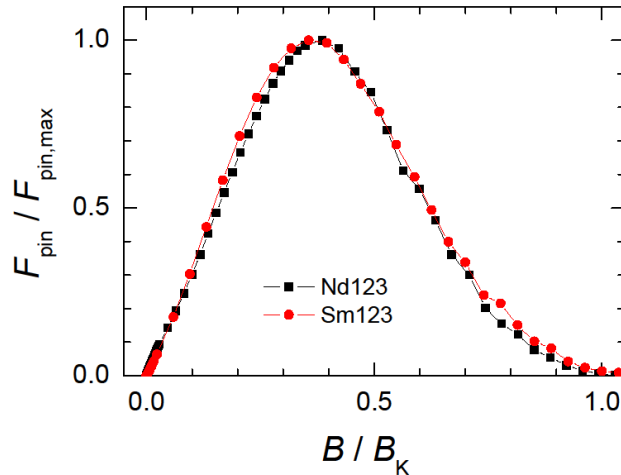


Fig. 8.3.11. Normalized pinning force density at  $T = 0.87T_c$  for (Sm,Nd)123 crystals.

#### 8.4. Brief summary of rare earth substitutions into Y position in $\text{YBa}_2\text{Cu}_3\text{O}_{7-\delta}$

Single crystals of optimally oxygenated Y123 and  $(\text{Nd,Sm})_{1+y}\text{Ba}_{2-y}\text{Cu}_3\text{O}_{7-\delta}$ , i.e. (Nd,Sm)123 solid solutions were investigated by SQUID magnetometry. The anisotropy parameter was investigated for Y123 and Sm123 by magnetization measurements and found to be around 6 and 10, respectively. The highest values of the upper critical fields were found for Sm123 which is characterized by the steepest slope of  $dH_{c2}/dT$  and by the largest thermodynamic critical field and the GL parameter.

The impact of substitution of Y by Nd and Sm ions on the vortex pinning in optimally oxygenated  $\text{YBa}_2\text{Cu}_3\text{O}_{7-\delta}$  single crystals was analysed. It was found that the same mechanism is responsible for vortex pinning in Nd123 and in Sm123. The vortex pinning in Y123 is strongly field-dependent, while a minimal effect of increasing temperature and field on the vortex pinning was found for (Nd,Sm)123. Compounds of (Sm,Nd)123 are characterized by the lowest irreversibility line and the highest pinning force density with respect to the temperature. Pinning centres in (Nd,Sm)123 crystals are more effective than in Y123 and  $(\text{Nd,Sm})_{1+y}\text{Ba}_{2-y}\text{Cu}_3\text{O}_{7-\delta}$  type solid solutions lead probably to the fishtail effect in the former. Pinning in (Sm,Nd)123 is mostly effective in intermediate fields, whereas the strongest pinning centres (effective in high fields) are present in Y123 with the oxygen content higher than optimal.



## 9. Conclusions

In this work, studies of the magnetic properties of single crystals of high temperature superconductors  $\text{REBa}_2\text{Cu}_3\text{O}_{7-\delta}$  (RE123, RE – a rare earth or Y ion) were presented. The oxygen deficiency effect in Sm123, the influence of a partial substitution of Y by Pr ions in the Y123 system, and the influence of different rare earths on the superconducting state parameters of RE123 were investigated. SQUID and torque magnetometry, AC susceptibility, and Hall scans were applied to determine the superconducting state properties.

Much effort has been already made to find a material with the best superconducting properties for engineering applications. A lot of attention was drawn to Sm123 due to its higher  $T_c$  and higher critical current densities as compared to Y123. However, no complete comparison of Sm123 and Y123 superconductors has been presented so far. In particular, the dependence of the thermodynamic parameters on the oxygen content has been studied in detail only for Y123. In this work, the properties of Sm-based cuprates were presented and compared with Y123 for a broad range of doping levels. For Sm123 crystals with  $T_c$  decreasing from 63.6 K to 42.8 K (via the removal of oxygen from the conducting CuO chains during sample preparation) an increase of the effective mass anisotropy from around 25 to 56 was found. The anisotropy dependence on  $T_c$  is very similar for Y123 and Sm123. Nevertheless, higher crossover fields are found for Sm123 than for Y123, which are related to better vortex pinning in the former.

The recent evidence for a strong temperature dependence of the anisotropy parameter,  $\gamma(T)$ , in two high- $T_c$  superconductors, namely  $\text{MgB}_2$  and the pnictides, caused great interest. Deviations from a temperature independent anisotropy parameter are not always caused by multiband superconductivity and have been found in various superconductors. This behaviour is in pronounced contrast to the assumptions of the standard anisotropic Ginzburg-Landau theory with a single anisotropy parameter. In this work, the observation of a strong  $\gamma(T)$  dependence in underdoped cuprates was reported for the first time, which is indeed an intrinsic property. For the investigated crystal with the lowest  $T_c$  of 42.8 K, the anisotropy parameter recorded in a magnetic field of 2 T, increases from  $35.9 \pm 0.8$  to  $59.2 \pm 1.2$  while lowering the temperature from 40 to 36 K. The origin of temperature dependent anisotropy parameters is not clarified so far. The strong temperature dependence of the anisotropy parameter in the underdoped cuprates may be related to several possibilities that were listed and discussed in this work. The Fermi surface of underdoped cuprates has not been resolved

yet. At the same time, the possibility of multiband superconductivity in the cuprates was proposed, but has not been confirmed so far. In order to do so, spectroscopic investigations are needed to probe the superconducting gaps directly. At present, there are no indications for a second superconducting gap in the energy spectrum of the cuprates. In contrast to the strong temperature dependence, only a very weak dependence of the anisotropy parameter on magnetic field was observed, but it cannot be excluded that this is a result of performing the measurements at fields close to  $H_{c2}^{\parallel c}$ . No dependence of the superfluid density on the magnetic field was found. However, a scenario of multiple band or multiple gap superconductivity in the cuprates cannot yet be completely excluded.

Among various methods employed for the enhancement of the pinning force in RE123 superconductors, cationic substitution is known to be effective for significantly increasing  $J_c$ . The Pr ions introduced in the Y position in Y123 are expected to provide effective pinning centres. All previous work focused on a higher substitutions level, i.e. above 10%, where the introduction of Pr resulted in a noticeable decrease of the thermodynamic parameters. In this work, the impact of low level Pr substitution on the thermodynamic properties of Y123 with a high transition temperature and a high thermodynamic critical field was presented. For crystals with similar types of defects, the shift of the irreversibility line to higher fields and higher critical currents were found to be mainly due to the change in the intrinsic parameters ( $n_s$  and  $H_c$ ). An increase in the trapped field,  $B_t$ , for higher Pr content in YPr123 crystals was observed by Hall probe scanning and was consistent with the  $J_c(B)$  increase found in magnetization measurements. The vortex pinning analysis was based on the numerical solution of the Ginzburg-Landau equation with a logarithmic pinning potential and on the pinning force density calculated from the Bean model. Higher temperatures for flux flow activation in YPr123 crystals with higher Pr content were found. The introduction of small amounts of Pr into the sample strengthens pinning most effectively at moderate and high magnetic fields.

It may be expected that introducing additional defects into HTSC, magnetic ions in particular, may be an efficient way to modify the superconducting state anisotropy. In this work the superconducting state anisotropy parameter was investigated by torque magnetometry. In the investigated low level Pr-doped  $\text{YBa}_2\text{Cu}_3\text{O}_{7-\delta}$  crystals with Pr content of up to 2.4% the anisotropy parameter was found to be independent of the Pr content. The average value of the anisotropy is 7.4 and independent of temperature and field. The interplay of intrinsic pinning and disorder leads to a complex behaviour of vortex lines for fields

applied close to the  $ab$ -plane. In this work intrinsic pinning was observed in all crystals via a pronounced peak of the irreversible torque signal for magnetic fields deviating from the direction parallel to the  $ab$ -plane by  $0.5 - 1^\circ$ . The peak in the torque was attributed to the kinked state of vortices.

Understanding the pinning mechanisms is important for achieving industrially more functional materials with the highest possible  $T_c$ ,  $H_{irr}$ , and  $H_{c2}$ . Compared to Y123, the (Nd,Sm)123 superconductors are characterized by better pinning properties, but the full elimination of (Nd,Sm)-Ba substitutions is an issue. The spin-charge stripe order was widely discussed in high- $T_c$  cuprates, but observed only for limited materials with specific hole doping rates. The vortex pinning analysis performed in this work was based on magnetization measurements and the numerical solution of the Ginzburg-Landau equation with a logarithmic pinning potential. Vortex pinning was found to be most field sensitive in optimally oxygenated Y123. In (Nd,Sm)123, vortex pinning is hardly influenced by changing the temperature and the pinning centres are effective in a broad range of magnetic fields. The (Nd,Sm)-Ba substitutions may be responsible for the fishtail effect, most pronounced in (Nd,Sm)123 compounds, and may lead to the formation of stripes.

Investigations of superconductivity in  $MgB_2$  and the pnictides, that led to the discovery of various new phenomena, are still stimulating new research on cuprates. There are striking similarities between the three groups of HTSC and considerable progress has been made in understanding the physics of unconventional superconductors. It is now known that underdoped cuprates, besides multiband superconductors, belong to the same group of superconductors, where the temperature dependence of the anisotropy parameter is an intrinsic property. Although a scenario of multiple band or multiple gap superconductivity in the cuprates cannot be excluded completely, it may be necessary to reconsider the temperature dependence of the interlayer coupling in highly underdoped cuprates and to formulate a new theory describing the anisotropy in strongly layered HTSC. In conclusion, I think that after twenty four years of extensive research we can still discover surprising properties and much about cuprates remains unknown and many problems are waiting to be solved. I'm very happy that I was part of these explorations as I believe that we have to *look and we will find it - what is unsought will go undetected* (by Sophocles).





## Acknowledgements

I am very grateful to the Marie Curie project NESPA for the financial support. I am thankful for the possibility to spend 20 months during 4 years of my studies in Atominstute in the group of Prof. Harald W. Weber, to attend various interesting courses, and to exchange ideas with other NESPA fellows.

Otrzymanie przedstawionych w pracy doktorskiej wyników badań możliwe było dzięki finansowemu wsparciu Ministerstwa Nauki i Szkolnictwa Wyższego w ramach grantu promotorskiego Nr N N202 2412 37 oraz grantu Nr N N202 4132 33 w którym byłam jednym ze współwykonawców.

Dziękuję mojemu promotorowi, Prof. Romanowi Puźniakowi, za możliwość zajmowania się tematem nadprzewodnictwa oraz za nieocenione rady i wskazówki. Dziękuję za zapoznanie mnie z technikami pomiarowymi oraz za cały poświęcony mi czas.

Dziękuję Prof. Andrzejowi Wiśniewskiemu za krytyczne czytanie zarówno tej pracy jak i poprzednich publikacji. Dziękuję nie tylko za cenne uwagi lecz również za ojcowskie wsparcie w trudnych chwilach.

Großer Dank gebührt an dieser Stelle Prof. Harald W. Weber, der mir die Möglichkeit gab, in seiner Forschungsgruppe einen entscheiden Anteil dieser Arbeit zu realisieren. Seine Unterstützung in wissenschaftlicher Hinsicht haben wesentlich zum Erfolg des Projekts beigetragen.

Ich möchte zudem Dr. Martin Zehetmayer für sein großes Engagement bei der Einführung in die Theorie der Supraleitung und die kollegiale Atmosphäre danken.

I would like to thank Prof. Xin Yao and his students, Y. Q. Cai and C. Y. Tang, for providing the crystals and for their help in understanding the crystals' growth process.

Many thanks to Prof. Terry Doyle for the possibility of applying his computation method to the investigated crystals, for his help in understanding equilibrium properties of superconductors, and his general kindness.

Dziękuję Prof. Markowi Berkowskiemu za udostępnienie komory do wygrzewania próbek oraz za życzliwość i pomoc w zrozumieniu technik wzrostu kryształów.

Dziękuję Doc. Kazimierzowi Conderowi za cały czas poświęcony na wygrzanie próbek w Villigen.

Dziękuję pracownikom Oddziału ON3, Viktorowi Domukhovskiemu, Markowi Barańskiemu oraz Witoldowi Adamczukowi, za pomiary dyfrakcji rentgenowskiej oraz pomoc przy technicznej obróbce kryształów.

Niezmiernie wdzięczna jestem przyjaciołom z IFPAN za wsparcie, w szczególności dziękuję Sergiy'owi Truszkiniowi oraz Krzysztofowi Kolwasowi za dyskusje podczas wspólnych obiadów.

Many thanks to friends from Atominstytut for all the fruitful discussions and for valuable and everlasting support in scientific research. Special thanks to Michal Chudy, Dr. Tom Withnell, and Dr. Enric Pardo for sharing the moments during our NESPA projects.

Dziękuję przyjaciołom i rodzinie za wsparcie i otuchę.

## References

- [1] H. K. Onnes, *Comm. Phys. Univ. Leiden*, Nos. 119, 120, 121 (1911).
- [2] F. London and H. London, *Proc. R. Soc. London A* **149**, 71 (1935).
- [3] V. L. Ginzburg and L.D. Landau, *Zh. Eksp. Teor. Fiz.* **20**, 1064 (1950).
- [4] J. Bardeen, L. N. Cooper, and J. R. Schrieffer, *Phys. Rev.* **108**, 1175 (1957).
- [5] *High-Temperature Superconductivity*, edited by V. L. Ginzburg and D. A. Kirzhnits (Consultants Bureau, New York, 1982).
- [6] R. J. Cava, *J. Am. Ceram. Soc.* **83**, 5 (2000).
- [7] M. Tinkham, *Introduction to Superconductivity* (McGraw Hill, New York, 1996).
- [8] J. G. Bednorz and K. A. Müller, *Z. Phys. B* **64**, 189 (1986).
- [9] M. K. Wu, J. R. Ashburn, C. J. Torng, P. H. Hor, R. L. Meng, L. Gao, J. J. Huang, Y. Q. Wang, and S. W. Chu, *Phys. Rev. Lett.* **58**, 908 (1987).
- [10] A. Schilling, M. Cantoni, J. D. Guo, and H. R. Ott, *Nature* **363**, 56 (1993).
- [11] G. F. Sun, K. W. Wong, B. R. Xu, Y. Xin, and D. F. Lu, *Phys. Lett. A* **192**, 122 (1994).
- [12] P. W. Anderson, *Science* **235**, 1196 (1987).
- [13] J. Zaanen, S. Chakravarty, T. Senthil, P. Anderson, P. Lee, J. Schmalian, M. Imada, D. Pines, M. Randeria, Ch. Varma, M. Vojta, and M. Rice, *Nature Phys.* **2**, 138 (2006).
- [14] H. J. Choi, D. Roundy, H. Sun, M. L. Cohen, and S. G. Louie, *Nature* **418**, 758 (2002).
- [15] P. Szabo, P. Samuely, J. Kacmarcik, T. Klein, J. Marcus, D. Fruchart, S. Miraglia, C. Marcenat, and A. G. M. Jansen, *Phys. Rev. Lett.* **87**, 137005 (2001).
- [16] M. Angst, R. Puzniak, A. Wisniewski, J. Jun, S. M. Kazakov, J. Karpinski, J. Roos, and H. Keller, *Phys. Rev. Lett.* **88**, 167004 (2002).
- [17] M. Angst and R. Puzniak, *Focus on Superconductivity Research 2003*, edited by B. P. Martines (Nova Publishers, New York, 2004), pp. 1-49; cond-mat/0305048.
- [18] J. Nagamatsu, N. Nakagawa, T. Muranaka, Y. Zenitani, and J. Akimitsu, *Nature* **410**, 63 (2001).
- [19] Y. Kamihara, T. Watanabe, M. Hirano, and H. Hosono, *J. Am. Chem. Soc.* **130**, 3296 (2008).
- [20] I. I. Mazin and V. P. Antropov, *Physica C* **385**, 49 (2003).
- [21] I. I. Mazin, D. J. Singh, M. D. Johannes, and M. H. Du, *Phys. Rev. Lett.* **101**, 057003 (2008).
- [22] K. Kuroki, S. Onari, R. Arita, H. Usui, Y. Tanaka, H. Kontani, and H. Aoki, *Phys. Rev. Lett.* **101**, 087004 (2008).
- [23] A. S. Alexandrov and N. F. Mott, *Int. J. Mod. Phys.* **8**, 2075 (1994).
- [24] P. Monthoux, A. V. Balatsky, and D. Pines, *Phys. Rev. Lett.* **67**, 3448 (1991).
- [25] S. C. Zhang, *Science* **275**, 5303 (1997).
- [26] J. Zhao, Q. Huang, C. de la Cruz, S. Li, J. W. Lynn, Y. Chen, M. A. Green, G. F. Chen, G. Li, Z. Li, J. L. Luo, N. L. Wang, P. Dai, *Nature Materials* **7**, 953 (2008).

- [27] H. Luetkens, H. H. Klauss, M. Kraken, F. J. Litterst, T. Dellmann, R. Klingeler, C. Hess, R. Khasanov, A. Amato, C. Baines, M. Kosmala, O. J. Schumann, M. Braden, J. Hamann-Borrero, N. Leps, A. Kondrat, G. Behr, J. Werner, and B. Buechner, *Nature Materials* **8**, 305 (2009).
- [28] H. W. Weber, *Supercond. Sci. Technol.* **5**, S19 (1992).
- [29] R. Biswal, J. John, D. Behera, P. Mallick, S. Kumar, D. Kanjilal, T. Mohanty, P. Raychaudhuri, and N. C. Mishra, *Supercond. Sci. Technol.* **21**, 085016 (2008).
- [30] L. Civale, A. D. Marwick, T. K. Worthington, M. A. Kirk, J. R. Thompson, L. Krusin-Elbaum, Y. Sun, J. R. Clem, and F. Holtzberg, *Phys. Rev. Lett.* **67**, 648 (1991).
- [31] J. R. Thompson, Y. R. Sun, H. R. Kerchner, D. K. Christen, B. C. Sales, B. C. Chakoumakos, A. D. Marwick, L. Civale, and J. O. Thomson, *Appl. Phys. Lett.* **60**, 2306 (1992).
- [32] L. Krusin-Elbaum, J. R. Thompson, R. Wheeler, A. D. Marwick, C. Li, S. Patel, D. T. Shaw, P. Lisowski, and J. Ullmann, *Appl. Phys. Lett.* **64**, 3331 (1994).
- [33] T. Haugan, P. N. Barnes, R. Wheeler, F. Meisenkothen, and M. Sumption, *Nature* **430**, 867 (2004).
- [34] T. Higuchi, S. I. Yoo, and M. Murakami, *Phys. Rev. B* **59**, 1514 (1999).
- [35] K. Rogacki, B. Dabrowski, and O. Chmaissem, *Phys. Rev. B* **73**, 224518 (2006).
- [36] H. Huhtinen, V. P. S. Awana, A. Gupta, H. Kishan, R. Laiho, and A. V. Narlikar, *Supercond. Sci. Technol.* **20**, S159 (2007).
- [37] M. Muralidhar, M. Jirsa, N. Sakai, M. Murakami, and I. Hirabayashi, *Materials Structure and Engineering B* **151**, 90 (2008).
- [38] H. Kupfer, Th. Wolf, C. Lessing, A. A. Zhukov, X. Lencon, R. Meiner-Hirmer, W. Schauer, and H. Wuhl, *Phys. Rev. B* **58**, 2886 (1998).
- [39] V. Ginzburg, *Sov. Phys. JETP* **4**, 153 (1957).
- [40] A. A. Abrikosov and L. P. Gor'kov, *Zh. Eksp. Teor. Fiz.* **39**, 1781 (1961) [*Sov. Phys. JETP* **12**, 1243 (1961)].
- [41] P. A. Lee, N. Nagaosa, and X. G. Wen, *Rev. Mod. Phys.* **78**, 17 (2006).
- [42] C. de la Cruz, Q. Huang, J. W. Lynn, J. Li, W. Ratcliff, J. L. Zarestky, H. A. Mook, G. F. Chen, J. L. Luo, N. L. Wang, and P. Dai, *Nature* **453**, 899 (2008).
- [43] *Handbook of High-Temperature Superconductivity: Theory and Experiment*, edited by J. R. Schrieffer and J. Brooks (Springer, Berlin, 2007).
- [44] M. L. Kuclic and I. M. Kuclic, *Physica C* **391**, 42 (2003).
- [45] L. Soderholm, K. Zhang, D. G. Hinks, M. A. Beno, J. D. Jorgensen, C. U. Segre, and I. K. Schuller, *Nature* **328**, 604 (1987).
- [46] A. Kebede, C. S. Jee, J. Schwegler, J. E. Crow, T. Mihalisin, G. H. Myer, R. E. Salomon, P. Schlottmann, M. V. Kuric, S. H. Bloom, and R. P. Guertin, *Phys. Rev. B* **40**, 4453 (1989).
- [47] G. Y. Guo and W. M. Temmerman, *Phys. Rev. B* **41**, 6372 (1990).
- [48] Y. Japha and V. Zevin, *Phys. Rev. B* **46**, 9240 (1992).
- [49] T. Harada and K. Yoshida, *Physica C* **383**, 48 (2002).

- [50] W. Meissner and R. Ochsenfeld, *Naturwiss.* **21**, 787 (1933).
- [51] U. Essmann and H. Trauble, *Phys. Lett.* **24A**, 526 (1967).
- [52] G. Blatter, M. V. Feigelman, V. B. Geshkenbein, A. I. Larkin, and V. M. Vinokur, *Rev. Mod. Phys.* **66**, 1125 (1994).
- [53] E. Zeldov, D. Majer, M. Konczykowski, V. B. Geshkenbein, V. M. Vinokur, and H. Shtrikman, *Nature* **375**, 373 (1995).
- [54] D. R. Nelson, *Phys. Rev. Lett.* **60**, 1973 (1988).
- [55] P. de Gennes, *Superconductivity in Metals and Alloys* (Westview Press, Oxford, 1999)
- [56] V. G. Kogan, A. Gurevich, J. H. Cho, D. C. Johnston, M. Xu, J. R. Thompson, and A. Martynovich, *Phys. Rev. B* **54**, 12386 (1996).
- [57] V. G. Kogan, *Phys. Rev. B* **24**, 1572 (1981).
- [58] V. G. Kogan, M. M. Fang, and S. Mitra, *Phys. Rev. B* **38**, 11958 (1988).
- [59] V. G. Kogan, *Phys. Rev. B* **38**, 7049 (1988).
- [60] L. N. Cooper, *Phys. Rev.* **104**, 1189 (1956).
- [61] L. D. Landau, *Nature* **138**, 840 (1936).
- [62] A. A. Abrikosov, *Zh. Eksp. Teor. Fiz.* **32**, 1442 (1957).
- [63] W. E. Lawrence and S. Doniach, *Proc. of the 12<sup>th</sup> Conf. on Low-Temperature Physics*, ed. E. Kanda, p. 361, Kyoto (1970).
- [64] B. D. Josephson, *Phys. Lett.* **1**, 251 (1962).
- [65] E. H. Brandt, *Phys. Rev. B* **68**, 054506 (2003).
- [66] P. W. Anderson, *Phys. Rev. Lett.* **9**, 309 (1962).
- [67] P. W. Anderson and Y. B. Kim, *Rev. Mod. Phys.* **36**, 39 (1964).
- [68] P. D. Panetta, J. E. Ostenson, D. K. Finnemore, and C. L. Snead, *Phys. Rev. B* **52**, 15570 (1995).
- [69] M. Angst, S. M. Kazakov, J. Karpinski, A. Wisniewski, R. Puzniak, and M. Baran, *Phys. Rev. B* **65**, 094518 (2002).
- [70] A. Schilling, R. A. Fisher, N. E. Phillips, U. Welp, W. K. Kwok, and G. W. Crabtree, *Phys. Rev. Lett.* **78**, 4833 (1998).
- [71] M. Willemin, C. Rossel, J. Hofer, H. Keller, A. Erb, and E. Walker, *Phys. Rev. B* **58**, R5940 (1998).
- [72] M. Willemin, A. Schilling, H. Keller, C. Rossel, J. Hofer, U. Welp, W. K. Kwok, R. J. Olsson, and G. W. Crabtree, *Phys. Rev. Lett.* **81**, 4236 (1998).
- [73] D. Babic, J. R. Cooper, J. W. Hodby, and Ch. Chengkan, *Phys. Rev. B* **60**, 689 (1999).
- [74] K. Kitazawa, J. Shimoyama, H. Ikuta, T. Sasagawa, and K. Kishio, *Physica C* **282**, 335 (1997).
- [75] C. M. Aegerter, S. T. Johnson, W. J. Nuttall, S. H. Lloyd, M. T. Wylie, M. P. Nutley, E. M. Forgan, R. Cubitt, S. L. Lee, D. M. Paul, M. Yethiraj, and H. A. Mook, *Phys. Rev. B* **57**, 14511 (1998).

- [76] P. L. Gammel, L. F. Schneemayer, J. V. Waszczak, and D. J. Bishop, Phys. Rev. Lett. **61**, 1666 (1988).
- [77] J. Shi, X. S. Ling, R. Liang, D. A. Bonn, and W. N. Hardy, Phys. Rev. B **60**, 12593 (1999).
- [78] D. E. Farrell, J. P. Rice, and D. M. Ginsberg, Phys. Rev. Lett. **67**, 1165 (1991).
- [79] H. Safar, P. L. Gammel, D. A. Huse, D. J. Bishop, J. P. Rice, and D. M. Ginsberg, Phys. Rev. Lett. **69**, 824 (1992).
- [80] A. Houghton, R. A. Pelcovits, and A. Sudbo, Phys. Rev. B **40**, 6763 (1989).
- [81] R. Liang, D. A. Bonn, and W. N. Hardy, Phys. Rev. Lett. **76**, 835 (1996).
- [82] J. E. Sonier, J. H. Brewer, and R. F. Kiefl, Rev. Mod. Phys. **72**, 769 (2000).
- [83] G. P. Mikitik and E. H. Brandt, Phys. Rev. B **64**, 184514 (2001).
- [84] E. M. Forgan, S. J. Levett, P. G. Kealey, R. Cubitt, C. D. Dewhurst, and D. Fort, Phys. Rev. Lett. **88**, 167003 (2002).
- [85] V. V. Eremenko, V. A. Sirenko, Y. A. Shabakayeva, R. Schleser, and P. L. Gammel, Low Temp. Phys. **28**, 6 (2002).
- [86] C. Lobb, Phys. Rev. B **36**, 3930 (1987).
- [87] D. Fisher, M. Fisher, and D. Huse, Phys. Rev. B **43**, 130 (1991).
- [88] M. Tachiki and S. Takahashi, Solid State Commun. **70**, 291 (1989).
- [89] G. Blatter, J. Rhyner, and V. M. Vinokur, Phys. Rev. B **43**, 7826 (1991).
- [90] D. Feinberg and C. Villard, Phys. Rev. Lett. **65**, 919 (1990).
- [91] L. N. Bulaevskii, M. Ledvij, and V. G. Kogan, Phys. Rev. B **46**, 366 (1992).
- [92] S. Kohout, T. Schneider, J. Roos, H. Keller, T. Sasagawa, and H. Takagi, Phys. Rev. B **76**, 064513 (2007).
- [93] B. I. Ivlev, Y. N. Ovchinnikov, and V. L. Pokrovskii, Mod. Phys. Lett. **5**, 73 (1991).
- [94] D. Feinberg, J. Phys. III (France) **4**, 169 (1994).
- [95] E. H. Brandt, J. Supercond. **6**, 4 (1993).
- [96] P. A. Mansky, P. M. Chaikin, and R. C. Haddon, Phys. Rev. Lett. **70**, 1323 (1993).
- [97] W. K. Kwok, U. Welp, V. M. Vinokur, S. Fleshler, J. Downey, and G. W. Crabtree, Phys. Rev. Lett. **67**, 390 (1991).
- [98] C. P. Bean, Phys. Rev. Lett. **8**, 250 (1962).
- [99] Y. B. Kim, C. F. Hempstead, and A. R. Strnad, Phys. Rev. Lett. **9**, 306 (1962).
- [100] Y. B. Kim, C. F. Hempstead, and A. R. Strnad, Phys. Rev. **129**, 528 (1963).
- [101] D. X. Chen and A. Sanchez, J. Appl. Phys. **70** (1991) 5463.
- [102] T. H. Johansen, M. R. Koblishka, H. Bratsberg and P. O. Hetland, Phys. Rev. B **56** (1997).
- [103] E. Zeldov, A. I. Larkin, V. B. Geshkenbein, M. Konczykowski, D. Majer, B. Khaykovich, V. M. Vinokur, and H. Shtrikman, Phys. Rev. Lett. **73**, 1428 (1994).
- [104] E. H. Brandt, Phys. Rev. B **60**, 11939 (1999).

- [105] C. P. Bean and J. D. Livingston, Phys. Rev. Lett. **12**, 14 (1964).
- [106] T. B. Berlincourt, R. R. Hake, and D. H. Leslie, Phys. Rev. Lett. **6**, 671 (1961).
- [107] Z. Hao, J. Clem, M. W. McElfresh, L. Civale, A. P. Malozemoff, and F. Holtzberg, Phys. Rev. B **43**, 2844 (1991).
- [108] R. Labusch and T. B. Doyle, European Conference on Applied Superconductivity (2003).
- [109] E. H. Brandt, Phys. Rev. Lett. **78**, 2208 (1997).
- [110] M. Jirsa, L. Pust, D. Dlouhy, and M. R. Koblischka, Phys. Rev. B **55**, 3276 (1997).
- [111] M. Jirsa, M. R. Koblischka, T. Higuchi, M. Muralidhar, and M. Murakami, Physica C **338**, 235 (2000).
- [112] M. Jirsa and L. Pust, Physica C **291**, 17 (1997).
- [113] E. J. Kramer, J. Appl. Phys. **44**, 1360 (1973).
- [114] D. Yin, Ch. Li, and W. Bai, Appl. Supercond. **5**, 147 (1998).
- [115] Y. Yeshurun and A.P. Malozemoff, Phys. Rev. Lett. **60**, 2202 (1988).
- [116] P. Fabricatore, C. Priano, A. Sciutti, G. Gemme, R. Musenich, R. Parodi, F. Gomory, and J. R. Thompson, Phys. Rev. B **54**, 12543 (1996).
- [117] D. Yin, W. Schauer, V. Winde, H. Kupfer, S. Zhang, and J. Chen, Z. Phys. B **94**, 249 (1994).
- [118] B. D. Josephson, Phys. Lett. **1**, 251 (1962).
- [119] B. D. Josephson, Adv. Phys. **14**, 419 (1965).
- [121] D. Martinen, Introduction to AC susceptibility (Quantum Design).
- [120] T. P. Papageorgiou, L. Bauernfeind, and H. F. Braun, J. Low Temp. Phys. **131**, 129 (2003).
- [122] C. Rossel, M. Willemin, A. Gasser, H. Bothuizen, G. I. Meijer, and H. Keller, Rev. Sci. Instrum. **69**, 3199 (1998).
- [123] M. Angst, Ph.D. Thesis, ETH Zurich, 2003.
- [124] M. Eisterer, S. Haindl, T. Wojcik, and H. W. Weber, Supercond. Sci. Technol. **16**, 1282 (2003).
- [125] D. Giller, A. Shaulov, T. Tamegai, and Y. Yeshurun, Phys. Rev. Lett. **84**, 3698 (2000).
- [126] D. Vaknin, S. K. Sinha, D. E. Moncton, D. C. Johnston, J. M. Newsam, C. R. Safinya, and H. E. King, Phys. Rev. Lett. **58**, 2802 (1987).
- [127] J. M. Tranquada, D. E. Cox, W. Kunnmann, H. Moudden, G. Shirane, M. Suenaga, P. Zolliker, D. Vaknin, S. K. Sinha, M. S. Alvarez, A. J. Jacobson, and D. C. Johnston Phys. Rev. Lett. **60**, 156 (1988).
- [128] D. Zech, K. Conder, H. Keller, E. Kaldis, and K. A. Müller, Physica B **219-220**, 136 (1996).
- [129] P. W. Anderson, Science **288**, 480 (2000).
- [130] P. M. Grant, Nature **407**, 139 (2000).
- [131] F. Holtzberg and C. Feild, Eur. J. Solid State Inorg. Chem. **27**, 107 (1990).

- [132] G. A. Emelchenko, A. A. Zhokhov, I. G. Naumenko, G. K. Baranova, S. A. Zverkov, M. Ja. Kartsovnik, A. E. Kovalev, G. Ju. Logvenov, L. N. Pronina and S. S. Khasanov, *Supercond. Sci. Technol.* **7**, 541 (1994).
- [133] T. Aselage and K. Keefer, *J. Mater. Res.* **3**, 1279 (1988).
- [134] Th. Wolf, W. Goldacker, B. Obst, and R. Flükiger, *J. Crystal Growth* **96**, 1010 (1989).
- [135] M. Nakamura, Y. Yamada, and Y. Shiohara, *J. Mater. Res.* **9**, 1946 (1994).
- [136] X. Yao, M. Egami, Y. Namikawa, T. Mizukoshi, Y. Shiohara, and S. Tanaka, *J. Crystal Growth* **165**, 198 (1996).
- [137] X. Yao, T. Izumi, and Y. Shiohara, *Supercond. Sci. Technol.* **16**, L13 (2003).
- [138] X. Yao, private communication.
- [139] M. Berkowski, "Nowe monokryształy tlenkowe wytwarzane metodą Czochralskiego", ISBN 83-89399-60-1, Warszawa (2004).
- [140] W. G. Phann, *Zone melting* (John Wiley and sons, New York, Chapman and Hall, London 1958).
- [141] R. Bayers and T. M. Shaw, *Solid State Phys.* **42**, 135 (1989).
- [142] V. Antal, K. Zmorayova, J. Kovac, V. Kavecansky, P. Diko, M. Eisterer, and H. W. Weber, *Supercond. Sci. Technol.* **23**, 065014 (2010).
- [143] R. Liang, D. A. Bonn, W. N. Hardy, J. C. Wynn, K. A. Moler, L. Lu, S. Larochelle, L. Zhou, M. Greven, L. Lurio, and S. G. J. Mochrie, *Physica C* **383**, 1 (2002).
- [144] L. Xiao, H. T. Ren, Y. L. Jiao, M. H. Zheng, and Y. X. Chen, *Physica C* **386**, 262 (2003).
- [145] J. M. Tarascon, W. R. McKinnon, L. H. Greene, G. W. Hull, and E. M. Vogel, *Phys. Rev. B* **36**, 226 (1987).
- [146] R. J. Cava, B. Batlogg, C. H. Chen, E. A. Rietman, S. M. Zahurak, and D. Werder, *Nature* **329**, 423 (1987).
- [147] R. Bayers, B. T. Ahn, G. Gorman, V. Y. Lee, S. S. P. Parkin, M. L. Ramirez, K. P. Roche, J. E. Vazquez, T. M. Gür, and R. A. Huggins, *Nature* **340**, 619 (1989).
- [148] K. Conder, *Mat. Sci. Eng. R* **32**, 41 (2001).
- [149] M. R. Presland, J. L. Tallon, R. G. Buckley, R. S. Liu, and N. E. Flower, *Physica C* **176**, 95 (1991).
- [150] J. L. Tallon, C. Bernhard, H. Shaked, R. L. Hitterman and J. D. Jorgensen, *Phys. Rev. B* **51**, 12911 (1995).
- [151] Y. J. Uemura, G. M. Luke, B. J. Sternlieb, J. H. Brewer, J. F. Carolan, W. N. Hardy, R. Kadono, J. R. Kempton, R. F. Kiefl, S. R. Kretzmann, P. Mulhern, T. M. Riseman, D. Li. Williams, B. X. Yang, S. Uchida, H. Takagi, J. Gopalakrishnan, A. W. Sleight, M. A. Subramanian, C. L. Chien, M. Z. Cieplak, G. Xiao, V. Y. Lee, B. W. Statt, C. E. Stronach, W. J. Kossler, and X. H. Yu, *Phys. Rev. Lett.* **62**, 2317 (1989).
- [152] P. A. Lee and X. G. Wen, *Phys. Rev. Lett.* **78**, 4111 (1997).



- [153] P. W. Anderson, P. A. Lee, M. Randeria, T. M. Rice, N. Trivedi, and F. C. Zhang, *J. Phys.: Condens. Matter* **16**, 755 (2004).
- [154] Ch. Kruger, K. Conder, H. Schwer, and E. Kaldis, *J. Solid State Chem.* **134**, 356 (1997).
- [155] G. V. M. Williams and J. L. Tallon, *J. Supercond.* **258**, 41 (1996).
- [156] R. D. Shannon, *Acta Cryst.* **A32**, 751 (1976).
- [157] S. I. Yoo, N. Sakai, H. Takaichi, T. Higuchi, and M. Murakami, *Appl. Phys. Lett.* **65**, 663 (1994).
- [158] M. Murakami, S. I. Yoo, T. Higuchi, N. Sakai, J. Weltz, N. Koshizuka, and S. Tanaka, *Jpn. J. Appl. Phys.* **33**, L715 (1994).
- [159] N. H. Babu, Y. Shi, K. Iida, and D. A. Cardwell, *Nature Materials* **4**, 476 (2005).
- [160] I. G. Chen, F. C. Chang, and M. K. Wu, *Supercond. Sci. Technol.* **15**, 717 (2002).
- [161] Y. Shi, N. H. Babu, K. Iida, and D. A. Cardwell, *J. Mater. Res.* **24**, 10 (2009).
- [162] W. Bieger, G. Krabbes, P. Schatzle, L. Zelenina, U. Wiesner, P. Verges, and J. Klosowski, *Physica C* **257**, 46 (1996).
- [163] Y. Watanabe, K. Miyake, A. Endo, K. Murata, Y. Shiohara, and T. Umeda, *Physica C* **280**, 215 (1997).
- [164] J. R. Clem, *Ann. Phys. (N.Y.)* **40**, 268 (1966).
- [165] N. R. Werthamer, E. Helfand, and P. C. Hohenberg, *Phys. Rev.* **147**, 295 (1966).
- [166] T. Schneider, *Phys. Rev. B* **75**, 174517 (2007).
- [167] Z. Bukowski, S. Weyeneth, R. Puzniak, P. Moll, S. Katrych, N. D. Zhigadlo, J. Karpinski, H. Keller, and B. Batlogg, *Phys. Rev. B* **79**, 104521 (2009).
- [168] H. Xiao, T. Hu, C. C. Almasan, T. A. Sayles, and M. B. Maple, *Phys. Rev. B* **73**, 184511 (2006).
- [169] D. Zech, C. Rossel, L. Lesne, H. Keller, S. L. Lee, and J. Karpinski, *Phys. Rev. B* **54**, 12535 (1996).
- [170] N. Chikumoto, S. Ozawa, S.I. Yoo, N. Hayashi, and M. Murakami, *Physica C* **278**, 187 (1997).
- [171] J. D. Fletcher, A. Carrington, O. J. Taylor, S. M. Kazakov, and J. Karpinski, *Phys. Rev. Lett.* **95**, 097005 (2005).
- [172] S. Weyeneth, R. Puzniak, N. D. Zhigadlo, S. Katrych, Z. Bukowski, J. Karpinski, and H. Keller, *J. Supercond. Novel Magn.* **22**, 347 (2009).
- [173] J. Jaroszynski, F. Hunte, L. Balicas, Y. Jo, I. Raicević, A. Gurevich, D. C. Larbalestier, F. F. Balakirev, L. Fang, P. Cheng, Y. Jia, and H. H. Wen, *Phys. Rev. B* **78**, 174523 (2008).
- [174] A. Schilling, M. Willemin, C. Rossel, H. Keller, R. A. Fisher, N. E. Phillips, U. Welp, W. K. Kwok, R. J. Olsson, and G. W. Crabtree, *Phys. Rev. B* **61**, 12535 (2000).
- [175] K. Conder, private communication.
- [176] M. Willemin, C. Rossel, J. Brugger, M. H. Despont, H. Rothuizen, P. Vettiger, J. Hofer, and H. Keller, *J. Appl. Phys.* **83**, 1163 (1998).
- [177] S. Kohout, J. Roos, and H. Keller, *Rev. Sci. Instrum.* **78**, 013903 (2007).

- [178] Quantum Design, Inc., <http://www.qdusa.com>.
- [179] B. Lundqvist, O. Rapp, and M. Andersson, *Phys. Rev. B* **62**, 3542 (2000).
- [180] T. R. Chien, W. R. Datars, B. W. Veal, A. P. Paulikas, P. Kostic, Ch. Gu, and Y. Jiang, *Physica C* **229**, 273 (1994).
- [181] A. Kortyka, R. Puzniak, A. Wisniewski, H. W. Weber, C. Y. Tang, X. Yao, and K. Conder, *Physica C* **470**, S217 (2010).
- [182] A. Kortyka, R. Puzniak, A. Wisniewski, M. Zehetmayer, H. W. Weber, C. Y. Tang, X. Yao, and K. Conder, *Phys. Rev. B* **82**, 054510 (2010).
- [183] D. R. Tilley, G. J. van Gorp, and C. W. Berghout, *Phys. Lett.* **12**, 305 (1964).
- [184] P. C. Hohenberg and N. R. Werthamer, *Phys. Rev.* **153**, 493 (1967).
- [185] H. W. Weber, E. Seidl, C. Laa, E. Schachinger, M. Prohammer, A. Junod, and D. Eckert, *Phys. Rev. B* **44**, 7585 (1991).
- [186] W. Pitscheneder and E. Schachinger, *Phys. Rev. B* **47**, 3300 (1993).
- [187] E. J. Kramer and G. S. Knapp, *J. Appl. Phys.* **46**, 4595 (1975).
- [188] M. R. Skokan, R. C. Morris, and W. G. Moulton, *Phys. Rev. B* **13**, 1077 (1976).
- [189] E. J. Kramer and G. S. Knapp, *J. Appl. Phys.* **46**, 4595 (1975).
- [190] Y. Muto, K. Noto, H. Nakatsuji, and N. Toyota, *Nuovo Cimento Soc. Ital. Fis. B* **38**, 503 (1977).
- [191] V. Metlushko, U. Welp, A. Koshelev, I. Aranson, G. W. Crabtree, and P. C. Canfield, *Phys. Rev. Lett.* **79**, 1738 (1997).
- [192] K. Takanaka, *Phys. Stat. Sol. B* **68**, 623 (1975).
- [193] H. Teichler, *Phys. Stat. Sol. B* **72**, 211 (1975).
- [194] V. G. Kogan, M. Bullock, B. Harmon, P. Miranovic, Lj. Dobrosavljevic-Grujic, P. L. Gammel, and D. J. Bishop, *Phys. Rev. B* **55**, R8693 (1997).
- [195] T. Ekino, H. Fujii, M. Kosugi, Y. Zenitani, and J. Akimitsu, *Physica C* **235-240**, 2529 (1994).
- [196] S. Manalo, H. Michor, M. El-Hagary, G. Hilscher, and E. Schachinger, *Phys. Rev. B* **63**, 104508 (2001).
- [197] B. Bergk, V. Petzold, H. Rosner, S. L. Dreschsler, M. Bartkowiak, O. Ignatchik, A. D. Bianchi, I. Sheikin, P. C. Canfield, and J. Wosnitza, *Phys. Rev. Lett.* **100**, 257004 (2008).
- [198] T. Dahm and N. Schopohl, *Phys. Rev. Lett.* **91**, 017001 (2003).
- [199] A. E. Koshelev and A. A. Golubov, *Phys. Rev. Lett.* **92**, 107008 (2004).
- [200] V. G. Kogan, *Phys. Rev. B* **66**, 020509 (2002).
- [201] P. Szabo, Z. Pribulova, G. Pristas, S. L. Budko, P. C. Canfield, and P. Samuely, *Phys. Rev. B* **79**, 012503 (2009).
- [202] D. Daghero, M. Tortello, R. S. Gonnelli, V. A. Stepanov, N. D. Zhigadlo, and J. Karpinski, *Phys. Rev. B* **80**, 060502 (2009).

- [203] S. Weyeneth, M. Bendele, R. Puzniak, F. Muranyi, A. Bussmann-Holder, N. D. Zhigadlo, S. Katrych, Z. Bukowski, J. Karpinski, A. Shengelaya, R. Khasanov, and H. Keller, *Europhys. Lett.* **91**, 47005 (2010).
- [204] P. Popovich, A. V. Boris, O. V. Dolgov, A. A. Golubov, D. L. Sun, C. T. Lin, R. K. Kremer, and B. Keimer, *Phys. Rev. Lett.* **105**, 027003 (2010).
- [205] T. Schneider, J. Hofer, M. Willemin, J. M. Singer, and H. Keller, *Eur. Phys. J. B* **3**, 413 (1998).
- [206] J. Hofer, T. Schneider, J. M. Singer, M. Willemin, H. Keller, T. Sasagawa, K. Kishio, K. Conder, and J. Karpinski, *Phys. Rev. B* **62**, 631 (2000).
- [207] V. Vulcanescu, G. Collin, H. Kojima, I. Tanaka, and L. Fruchter, *Phys. Rev. B* **50**, 4139 (1994).
- [208] D. Feinberg, *Physica C* **194**, 126 (1992).
- [209] D. Zech, J. Hofer, H. Keller, C. Rossel, P. Bauer, and J. Karpinski, *Phys. Rev. B* **53**, 366 (1996).
- [210] J. C. Martinez, S. H. Brongersma, A. Koshelev, B. Ivlev, P. H. Kes, R. P. Griessen, D. G. de Groot, Z. Tarnawski, and A. A. Menovsky, *Phys. Rev. Lett.* **69**, 2276 (1992).
- [211] L. Lyard, P. Szabo, T. Klein, J. Marcus, C. Marcenat, K. H. Kim, B. W. Kang, H. S. Lee, and S. I. Lee, *Phys. Rev. Lett.* **92**, 057001 (2004).
- [212] M. Angst, D. Di Castro, D. G. Eshchenko, R. Khasanov, S. Kohout, I. M. Savic, A. Shengelaya, S. L. Budko, P. C. Canfield, J. Jun, J. Karpinski, S. M. Kazakov, R. A. Ribeiro, and H. Keller, *Phys. Rev. B* **70**, 224513 (2004).
- [213] S. Weyeneth, R. Puzniak, U. Mosele, N. D. Zhigadlo, S. Katrych, Z. Bukowski, J. Karpinski, S. Kohout, J. Roos, and H. Keller, *J. Supercond. Novel Magn.* **22**, 325 (2009).
- [214] S. Serventi, G. Allodi, R. De Renzi, G. Guidi, L. Romano, P. Manfrinetti, A. Palenzona, Ch. Niedermayer, A. Amato, and Ch. Baines, *Phys. Rev. Lett.* **93**, 217003 (2004).
- [215] R. Cubitt, M. R. Eskildsen, C. D. Dewhurst, J. Jun, S. M. Kazakov, and J. Karpinski, *Phys. Rev. Lett.* **91**, 047002 (2003).
- [216] R. Khasanov, A. Shengelaya, A. Maisuradze, F. La Mattina, A. Bussmann-Holder, H. Keller, and K. A. Müller, *Phys. Rev. Lett.* **98**, 057007 (2007).
- [217] F. Hunte, J. Jaroszynski, A. Gurevich, D. C. Larbalestier, R. Jin, A. S. Sefat, M. A. McGuire, B. C. Sales, D. K. Christen, and D. Mandrus, *Nature* **453**, 903 (2008).
- [218] A. J. Drew, F. L. Pratt, T. Lancaster, S. J. Blundell, P. J. Baker, R. H. Liu, G. Wu, X. H. Chen, I. Watanabe, V. K. Malik, A. Dubroka, K. W. Kim, M. Rossle, and C. Bernhard, *Phys. Rev. Lett.* **101**, 097010 (2008).
- [219] R. Khasanov, A. Shengelaya, A. Maisuradze, F. La Mattina, A. Bussmann-Holder, H. Keller, and K. A. Müller, *Phys. Rev. Lett.* **98**, 057007 (2007).
- [220] R. Khasanov, S. Strassle, D. Di Castro, T. Masui, S. Miyasaka, S. Tajima, A. Bussmann-Holder, and H. Keller, *Phys. Rev. Lett.* **99**, 237601 (2007).
- [221] A. Bussmann-Holder, R. Khasanov, A. Shengelaya, A. Maisuradze, F. La Mattina, H. Keller and K. A. Müller, *Europhys. Lett.* **77**, 27002 (2007).
- [222] H. Won and K. Maki, *Europhys. Lett.* **54**, 248 (2001).

- [223] H. Suhl, B. T. Matthias, and R. R. Walker, *Phys. Rev. Lett.* **3**, 552 (1959).
- [224] G. Binning, A. Baratoff, H. E. Hoenig, and J. G. Bednorz, *Phys. Rev. Lett.* **45**, 1352 (1980).
- [225] T. Yokoya, T. Kiss, A. Chainani, S. Shin, M. Nohara, and H. Takagi, *Science* **294**, 2518 (2001).
- [226] T. Das, R. S. Markiewicz, and A. Bansil, *Phys. Rev. B* **77**, 134516 (2008).
- [227] Ya. G. Ponomarev, N. B. Brandt, Chong Soon Khi, S. V. Tchesnokov, E. B. Tsokur, A. V. Yarygin, K. T. Yusupov, B. A. Aminov, M. A. Hein, G. Müller, H. Piel, D. Wehler, V. Z. Kresin, K. Rosner, K. Winzer, and Th. Wolf, *Phys. Rev. B* **52**, 1352 (1995).
- [228] W. E. Pickett, *Rev. Mod. Phys.* **61**, 433 (1989).
- [229] J. C. Campuzano, G. Jennings, M. Faiz, L. Beaulaigue, B. W. Veal, J. Z. Liu, A. P. Paulikas, K. Vandervoort, H. Claus, R. S. List, A. J. Arko, and R. J. Bartlett, *Phys. Rev. Lett.* **64**, 2308 (1990).
- [230] N. Doiron-Leyraud, C. Proust, D. LeBoeuf, J. Levallois, J. B. Bonnemaïson, R. Liang, D. A. Bonn, W. N. Hardy, and L. Taillefer, *Nature* **447**, 565 (2007).
- [231] W. H. Butler, *Phys. Rev. Lett.* **44**, 1516 (1980).
- [232] T. Kita and M. Arai, *Phys. Rev. B* **70**, 224522 (2004).
- [233] M. Arai and T. Kita, *J. Phys. Soc. Jpn.* **73**, 2924 (2004).
- [234] M. Prohammer and J. P. Carbotte, *Phys. Rev. B* **42**, 2032 (1990).
- [235] C. C. Tsuei and J. R. Kirtley, *Rev. Mod. Phys.* **72**, 969 (2000).
- [236] M. Okawa, K. Ishizaka, H. Uchiyama, H. Tadamoto, T. Masui, S. Tajima, X. Y. Wang, C. T. Chen, S. Watanabe, A. Chainani, T. Saitoh, and S. Shin, *Phys. Rev. B* **79**, 144528 (2009).
- [237] M. F. Limonov, A. I. Rykov, S. Tajima, and Y. Yamanaka, *Phys. Rev. B* **61**, 12412 (2000).
- [238] D. H. Lu, D. L. Feng, N. P. Armitage, K. M. Shen, A. Damascelli, C. Kim, F. Ronning, Z. X. Shen, D. A. Bonn, R. Liang, W. N. Hardy, A. I. Rykov, and S. Tajima, *Phys. Rev. Lett.* **86**, 4370 (2001).
- [239] J. R. Kirtley, C. C. Tsuei, A. C. J. M. Verwijs, S. Harkema, and H. Hilgenkamp, *Nature Phys.* **2**, 190 (2006).
- [240] H. J. H. Smilde, A. A. Golubov, A. G. Rijnders, J. M. Dekkers, S. Harkema, D. H. A. Blank, H. Rogalla, and H. Hilgenkamp, *Phys. Rev. Lett.* **95**, 257001 (2005).
- [241] S. Chakravarty, R. B. Laughlin, D. K. Morr, and C. Nayak, *Phys. Rev. B* **63**, 094503 (2001).
- [242] N. R. Werthamer and W. L. McMillan, *Phys. Rev.* **158**, 415 (1967).
- [243] A. Bussmann-Holder and H. Keller, *J. Supercond. Novel Magn.* **22**, 123 (2009).
- [244] G. Zhao, M. B. Hunt, H. Keller, and K. A. Müller, *Nature* **385**, 236 (1997).
- [245] A. Bussmann-Holder, R. Micnas, and A. R. Bishop, *Eur. Phys. J. B* **37**, 345 (2004).
- [246] T. Das, R. S. Markiewicz, and A. Bansil, *Phys. Rev. B* **77**, 134516 (2008).
- [247] P. C. Hohenberg and N. R. Werthamer, *Phys. Rev.* **153**, 493 (1967).
- [248] V. G. Kogan, *Phys. Rev. Lett.* **89**, 237005 (2002).
- [249] T. Watanabe and A. Matsuda, *Phys. Rev. B* **54**, R6881 (1996).

- [250] C. K. Krutzler, M. Zehetmayer, M. Eisterer, H. W. Weber, N. D. Zhigadlo, and J. Karpinski, *Phys. Rev. B* **75**, 224510 (2007).
- [251] M. Werner, F. M. Sauerzopf, H. W. Weber, and A. Wisniewski, *Phys. Rev. B* **61**, 14795 (2000).
- [252] A. Wisniewski, M. Baran, C. Czurda, H. W. Weber, M. Reissner, W. Steiner, L. Zhou, and P. X. Zhang, *Physica C* **266**, 309 (1996).
- [253] K. G. Vandervoort, Ph.D. Thesis, University of Chicago, Illinois, 1991.
- [254] A. Kebede, C. S. Jee, J. Schwegler, J. E. Crow, T. Mihalisin, G. H. Myer, R. E. Salomon, P. Schlottmann, M. V. Kuric, S. H. Bloom, and R. P. Guertin, *Phys. Rev. B* **40**, 4453 (1989).
- [255] M. W. Pieper, F. Wiekhorst, and T. Wolf, *Phys. Rev. B* **62**, 1392 (2000).
- [256] J. Fink, N. Nucker, H. Romberg, M. Alexander, M. B. Maple, J. J. Neumeier, and J. W. Allen, *Phys. Rev. B* **42**, 4823 (1990).
- [257] Q. B. Meng, Z. J. Wu, and S. Y. Zhang, *Physica C* **306**, 321 (1998).
- [258] Y. X. Jia, J. Z. Liu, M. D. Lan, P. Klavins, R. N. Shelton, and H. B. Radousky, *Phys. Rev. B* **45**, 10609 (1992).
- [259] J. L. Peng, P. Klavins, R. N. Shelton, H. B. Radousky, P. A. Hahn, and L. Bernardez, *Phys. Rev. B* **40**, 4517 (1989).
- [260] M. Anderson, O. Rapp, T. L. Wen, Z. Hegedüs, and M. Nygren, *Phys. Rev. B* **48**, 7590 (1993).
- [261] J. J. Neumeier, M. B. Maple, and M. S. Torikachvili, *Physica C* **156**, 574 (1988).
- [262] E.V. Sampathikumar, A. Suzuki, K. Kohn, T. Shibusya, A. Tohdake, and M. Ishikawa, *Jpn. J. Appl. Phys.* **27**, L584 (1988).
- [263] A. Suzuki, E.V. Sampathikumar, K. Kohn, T. Shibusya, A. Tohdake, and M. Ishikawa, *Jpn. J. Appl. Phys.* **27**, L792 (1988).
- [264] J. M. S. Skakle, *Mat. Sci. Eng. R* **23**, 1 (1998).
- [265] H. A. Blackstead, J. D. Dow, D. B. Chrisey, J. S. Horwitz, A. E. Klunzinger, and D. B. Pulling, *Phys. Rev. B* **54**, 6122 (1996).
- [266] Z. Zou, K. Oka, T. Ito, and Y. Nishihara, *Jpn. J. Appl. Phys.* **36**, L18 (1997).
- [267] Y. Abulafia, A. Shaulov, Y. Wolfus, R. Prozorov, L. Burlachkov, Y. Yeshurun, D. Majer, E. Zeldov, H. Wuhl, V. B. Geshkenbein, and V. M. Vinokur, *Phys. Rev. Lett.* **77**, 1596 (1996).
- [268] R. Labusch and T. B. Doyle, *Physica C* **290**, 143 (1997).
- [269] T. B. Doyle, R. Labusch, and R. A. Doyle, *Physica C* **290**, 148 (1997).
- [270] U. Welp, W. K. Kwok, G. W. Crabtree, K. G. Vanderwoort, and J. Z. Liu, *Phys. Rev. Lett.* **62**, 1908 (1989).
- [271] J. Tajima, K. Tomimoto, N. L. Wang, A. I. Rykov, and I. Terasaki, *J. Low Temp. Phys.* **117**, 413 (1999).
- [272] A. Kortyka, R. Puzniak, A. Wisniewski, M. Zehetmayer, H. W. Weber, Y. Q. Cai, and X. Yao, *Supercond. Sci. Technol.* **23**, 065001 (2010).
- [273] J. Rammer, *Europhys. Lett.* **5**, 77 (1988).

- [274] L. Krusin-Elbaum, A. P. Malozemoff, Y. Yeshurun, D. C. Cronemayer, and F. Holzberg, *Phys. Rev. B* **39**, 2936 (1989).
- [275] A. A. Zhukov, H. Kupfer, G. K. Perkins, A. D. Caplin, T. Wolf, K. I. Kugel, A. L. Rakhmanov, M. G. Mikheev, V. I. Voronkova, M. Klaser, and H. Wuhl, *Phys. Rev. B* **59**, 11213 (1999).
- [276] A. Kortyka, T. B. Doyle, R. Puzniak, A. Wisniewski, H. W. Weber, Y. Q. Cai, and X. Yao, *Supercond. Sci. Technol.* **22**, 105008 (2009).
- [277] A. Kortyka, R. Puzniak, A. Wisniewski, H. W. Weber, T. B. Doyle, Y. Q. Cai, and X. Yao, *J. Phys.: Conf. Ser.* **150**, 052123 (2009).
- [278] T. Sasagawa, K. Kishio, Y. Togawa, J. Shimoyama, and K. Kitazawa, *Phys. Rev. Lett.* **80**, 4297 (1998).
- [279] M. Oda, X. Yao, Y. Yoshida, and H. Ikuta, *Supercond. Sci. Technol.* **22**, 075012 (2009).
- [280] M. Zehetmayer, M. Eisterer, S. Sponar, H. W. Weber, A. Wisniewski, R. Puzniak, P. Panta, S. M. Kazakov, and J. Karpinski, *Physica C* **418**, 73 (2005).
- [281] D. Feinberg and A. M. Ettouhami, *Int. J. Mod. Phys. B* **7**, 2085 (1993).
- [282] M. Tachiki and S. Takahashi, *Solid State Commun.* **72**, 1083 (1989).
- [283] K. I. Kugel, A. L. Rakhmanov, and A. A. Zhukov, *Physica C* **334**, 203 (2000).
- [284] Yu. N. Ovchinnikov and B. I. Ivlev, *Phys. Rev. B* **43**, 8024 (1991).
- [285] M. Murakami, *Int. J. Appl. Ceram. Technol.* **4**, 225 (2007).
- [286] Y. Shiohara and A. Endo, *Mater. Sci. Eng. R* **19**, 1 (1997).
- [287] D. A. Cardwell, *Mater. Sci. Eng. B* **53**, 1 (1998).
- [288] K. Watanabe, S. Awaji, K. Koyama, G. Nishijima, K. Takahashi, and Y. Sasaki, *J. Low Temperature Physics* **159**, 370 (2010).
- [289] N. H. Babu, W. Lo, D. A. Cardwell, and A. M. Campbell, *Appl. Phys. Lett.* **75**, 2981 (1999).
- [290] M. Muralidhar, N. Sakai, N. Chikumoto, M. Jirsa, T. Machi, M. Nishiyama, Y. Wu, and M. Murakami, *Phys. Rev. Lett.* **89**, 237001 (2002).
- [291] A. Hu, M. R. Koblischka, X. Yao, H. Zhou, M. Winter, U. Hartmann, and M. Murakami, *Supercond. Sci. Technol.* **19**, 580 (2006).
- [292] J. M. Tranquada, B. J. Sternlieb, J. D. Axe, Y. Nakamura, and S. Uchida, *Nature* **375**, 561 (1995).
- [293] E. S. Bozin, G. H. Kwei, H. Takagi, and S. J. L. Billinge, *Phys. Rev. Lett.* **84**, 5856 (2000).
- [294] V. J. Emery and S. A. Kivelson, *Physica C* **209**, 597 (1993).
- [295] R. S. Markiewicz, *J. Phys. Chem. Solids* **58**, 1179 (1997).
- [296] J. Zaanen and O. Gunnarsson, *Phys. Rev. B* **40**, 7391 (1989).
- [297] U. Low, V. J. Emery, K. Fabricius, and S. A. Kivelson, *Phys. Rev. Lett.* **72**, 1918 (1994).
- [298] S. R. White and D. J. Scalapino, *Phys. Rev. Lett.* **80**, 1272 (1998).
- [299] S. R. White and D. J. Scalapino, *Phys. Rev. Lett.* **81**, 3227 (1998).

- [300] J. Tranquada, *Physics World*, Nov 1 (1999).
- [301] H. A. Mook and F. Dogan, *Nature* **401**, 145 (1999).
- [302] J. Zaanen, *Nature* **440**, 1118 (2006).
- [303] S. Kivelson, *Nature Phys.* **5**, 343 (2006).
- [304] J. M. Tranquada, J. D. Axe, N. Ichikawa, A. R. Moodenbaugh, Y. Nakamura, and S. Uchida, *Phys. Rev. Lett.* **78**, 338 (1997).
- [305] M. Fujita, H. Goka, K. Yamada, J. M. Tranquada, and L. P. Regnault, *Phys. Rev. B* **70**, 104517 (2004).
- [306] Z. X. Shen, P. J. White, D. L. Feng, C. Kim, G. D. Gu, H. Ikeda, R. Y. Oshizaki, and N. Koshizuka, *Science* **280**, 259 (1998).
- [307] P. Dai, H. A. Mook, and F. Dogan, *Phys. Rev. Lett.* **80**, 1738 (1998).
- [308] M. R. Koblishka, M. Winter, and U. Hartmann, *Supercond. Sci. Technol.* **20**, 681 (2007).
- [309] Y. Q. Cai, X. Yao, A. Hu, X. J. Wu, M. Jirsa, S. Xy, and G. Jin, *Supercond. Sci. Technol.* **19**, 506 (2006).
- [310] M. F. Limonov, E. A. Goodilin, X. Yao, S. Tajima, Y. Shiohara, and Y. E. Kitaev, *Phys. Rev. B* **58**, 12368 (1998).
- [311] E. Goodilin, M. Kambara, Y. Umeda, and Y. Shiohara, *Physica C* **289**, 37 (1997).
- [312] S. Li, E. A. Hayri, K. V. Ramanujachary, and M. Greenblatt, *Phys. Rev. B* **38**, 2450 (1988).
- [313] M. Kuznetsov, C. Krauns, M. Yoshizumi, T. Izumi, Y. Shiohara, and T. Umeda, *Physica C* **357**, 1068 (2001).
- [314] H. Shaked, B. W. Veal, J. Faber, R. L. Hitterman, U. Balachandran, G. Tomlins, H. Shi, L. Morss, and A. P. Paulikas, *Phys. Rev. B* **41**, 4173 (1990).
- [315] Z. Bukowski, Ph.D. Thesis, Institute of Low Temperature and Structure Research, Wroclaw, Poland, 1996.
- [316] V. A. Drozd, I. L. Baginski, S. A. Nedilko, and V. S. Melnikov, *J. Alloys Comp.* **384**, 44 (2004).
- [317] E. Goodilin, A. Oka, J. G. Wen, Y. Shiohara, M. Kambara, and T. Umeda, *Physica C* **299**, 279 (1998).
- [318] I. Vogel, R. Kucharkowski, and G. Krabbes, *Fresenius J. Anal. Chem.* **357**, 69 (1997).
- [319] T. B. Lindemer, E. D. Specht, P. M. Martin, and M. L. Flicroft, *Physica C* **255**, 65 (1995).
- [320] D. H. Kim, K. E. Gray, R. T. Kampwirth, J. C. Smith, D. S. Richeson, T. J. Marks, J. H. Kang, J. Talvacchio, and M. Eddy, *Physica C* **177**, 431 (1991).
- [321] J. L. Tallon, G. V. M. Williams, C. Bernard, D. M. Pooke, M. P. Staines, J. D. Johnson, and R. H. Meinhold, *Phys. Rev. B* **53**, R11972 (1996).

## List of publications

- A. Kortyka, R. Puzniak, A. Wisniewski, M. Zehetmayer, H. W. Weber, C. Y. Tang, X. Yao, and K. Conder, „Evidence for a temperature dependent anisotropy of the superconducting state parameters in underdoped  $\text{SmBa}_2\text{Cu}_3\text{O}_x$ ”, Phys. Rev. B **82**, 054510 (2010).
- A. Kortyka, R. Puzniak, A. Wisniewski, M. Zehetmayer, H. W. Weber, Y. Q. Cai, and X. Yao, „Anisotropy of the superconducting state parameters and intrinsic pinning in low-level Pr-doped  $\text{YBa}_2\text{Cu}_3\text{O}_{7-\delta}$ ”, Supercond. Sci. Technol. **23**, 065001 (2010).
- A. Kortyka, R. Puzniak, A. Wisniewski, H. W. Weber, C. Y. Tang, X. Yao, and K. Conder, “Irreversibility line and anisotropy of  $\text{SmBa}_2\text{Cu}_3\text{O}_{7-\delta}$  with varying oxygen content”, Physica C **470**, S217 (2010).
- A. Kortyka, T. B. Doyle, R. Puzniak, A. Wisniewski, H. W. Weber, Y. Q. Cai, and X. Yao, “Superconducting state parameters, pinning centres and their effectiveness in  $\text{Y}_{1-x}\text{Pr}_x\text{Ba}_2\text{Cu}_3\text{O}_{7-\delta}$  single crystals with low Pr contents”, Supercond. Sci. Technol. **22**, 105008 (2009).
- X. Q. Xu, Y. Q. Cai, C. X. Yang, X. Yao, S. Xu, A. Kortyka, and R. Puzniak, “Pr doping effects on property and growth behaviour of YBCO superconductor”, Supercond. Sci. Technol. **22**, 015001 (2009).
- A. Kortyka, R. Puzniak, A. Wisniewski, H. W. Weber, T. Doyle, Y. Q. Cai, and X. Yao, „Influence of low-level Pr substitution on the superconducting properties of  $\text{YBa}_2\text{Cu}_3\text{O}_{7-\delta}$  single crystals”, J. Phys.: Conf. Ser. **150**, 052123 (2009).
- A. Wisniewski, R. Puzniak, A. Bienias, M. Baran, J. Jun, N. D. Zhigadlo, and J. Karpinski, „Anisotropy of the lower and of the upper critical fields in  $\text{Mg}_{1-x}\text{Al}_x\text{B}_2$  single crystals”, Physica C **460**, 614 (2007).
- M. Gazda, B. Kusz, J. Piętosa, A. Bienias, R. Puźniak, S. Stizza, and S. Chudinov, „Effect of preparation conditions on superconducting properties of (Bi,Pb)–Sr–Ca–Cu–O glass–ceramics” Physica Status Solidi C **2**, 1674 (2005).
- M. Gazda, B. Kusz, S. Stizza, S. Chudinov, R. Natali, J. Piętosa, and A. Bienias, “Conductivity and superconductivity of  $(\text{Bi,Pb})_4\text{Sr}_3\text{Ca}_3\text{Cu}_4\text{O}_x$  glass–ceramic” Acta Physica Polonica A **106**, 617 (2004).



---

## Curriculum Vitae

|                          |                                      |
|--------------------------|--------------------------------------|
| Imię i nazwisko          | Anna Kortyka                         |
| Nazwisko rodowe          | Bienias                              |
| Data i miejsce urodzenia | 20 Sierpień 1982<br>Kozienice        |
| Adres zamieszkania       | ul. Lechicka 11/1<br>02-156 Warszawa |

## Edukacja

|                                  |   |
|----------------------------------|---|
| Październik 2006 – wrzesień 2010 | Studia doktoranckie w Instytucie Fizyki Polskiej Akademii Nauk, Warszawa. Kierunek badań: fizyka ciała stałego-nadprzewodnictwo wysokotemperaturowe   |
| Kwiecień 2007 – maj 2010         | Stypendium Marie Curie w ramach programu „NESPA”, Vienna University of Technology, Atominstitute, Wiedeń, 4 pobyty, łącznie 20 miesięcy   |
| Październik 2004 – czerwiec 2006 | Studia uzupełniające magisterskie na Uniwersytecie Kardynała Stefana Wyszyńskiego, w Szkole Nauk Ścisłych, w Warszawie. Specjalność magisterska: fizyka ciała stałego. Tytuł pracy magisterskiej: „Wpływ podstawień glinem na anizotropię pierwszego pola krytycznego w $MgB_2$ ”                                       |
| Wrzesień 2004 – styczeń 2005     | Studia magisterskie na Universiteit van Amsterdam w ramach programu Socrates/Erasmus, Amsterdam   |
| Październik 2001 – czerwiec 2004 | Studia licencjackie na Uniwersytecie Kardynała Stefana Wyszyńskiego, w Szkole Nauk Ścisłych, w Warszawie. Specjalność licencjacka: informatyka stosowana. Tytuł pracy licencjackiej: „Pomiary właściwości nadprzewodzących i modernizacja system sterującego kontrolerem temperatury w magnetometrze z drgającą próbką” |
| Wrzesień 1997 – czerwiec 2001    | Liceum Ogólnokształcące w Kozienicach. Profil matematyczno-fizyczny   |

**Letnie szkoły i konferencje**

|                               |   |
|-------------------------------|---|
| Czerwiec 2004 – sierpień 2010 | Uczestnictwo i prezentacja wyników na konferencjach naukowych: Krajowa Szkoła Nadprzewodnictwa w Warszawie (2004), w Łądku Zdrój (2007) i w Ostrowie Wielkopolskim (2009), LT25 w Amsterdamie (2008), M2S w Tokio (2009), EUCAS w Dreźnie (2009), ASC w Waszyngtonie (2010) |
| Lipiec 2004 – lipiec 2006     | Coroczne uczestnictwo w dwu-tygodniowych letnich szkołach dot. nadprzewodnictwa: ASSE w Budapeszcie (2004), SCENET w Turku (2005), SCENET w Camerino (2006)   |
| Sierpień – wrzesień 2005      | Praktyki studenckie w Hahn-Meitner Institute, Berlin. Kierunek badań: stopy metaliczne  |
| Czerwiec 2005                 | „51 Nobelpreisträgertagung”, spotkanie młodych naukowców z Noblistami, Lindau   |
| Marzec 2005                   | „Science in Society”, uczestnictwo i prezentacja Pikniku Naukowego Polskiego Radia Bis na forum zorganizowanym przez European Commission’s Research Directorate General, Bruksela   |

**Popularyzowanie nauki**

|                            |  |
|----------------------------|--|
| Styczeń 2010, styczeń 2009 | Opieka naukowa nad stypendystami Krajowego Funduszu na rzecz Dzieci podczas tygodniowych warsztatów w IFPAN      |
| Listopad 2008              | Opieka naukowa nad laureatami konkursu „First Step to Nobel Prize in Physics” podczas miesięcznego stażu w IFPAN |
| Maj 2002 – czerwiec 2005   | Coroczne uczestnictwo w Piknikach Naukowych Polskiego Radia Bis  |

**Otrzymane wyróżnienia**

|                                  |  |
|----------------------------------|--|
| Czerwiec 2006                    | Ukończenie studiów wśród 5% najlepszych absolwentów roku akademickiego 2005/2006 |
| Rok akademicki 2005/2006         | Stypendium Ministra Edukacji Narodowej i Sportu                                  |
| Czerwiec 2004                    | Dyplom licencjacki „cum laude”   |
| Październik 2002 – czerwiec 2005 | Corocznie uzyskiwane stypendium naukowe  |